UNIVERSIDAD NACIONAL DEL LITORAL

Hydrometeorological Forecasts and Their Sensitivity to Land Cover Changes

Omar Vicente Müller

FICH
FACULTAD DE INGENIERIA
Y CIENCIAS HIDRICAS

INTEC
INSTITUTO DE DESARROLLO TECNOLOGICO
PARA LA INDUSTRIA QUIMICA

Tesis de Doctorado **2015**

UNIVERSIDAD NACIONAL DEL LITORAL
Facultad de Ingeniería y Ciencias Hídricas
Instituto de Desarrollo Tecnológico para la Industria Química

HYDROMETEOROLOGICAL FORECASTS AND THEIR SENSITIVITY TO LAND COVER CHANGES

Omar Vicente Müller

Tesis remitida al Comité Académico del Doctorado
como parte de los requisitos para la obtención
del grado de
DOCTOR EN INGENIERIA
Mención Recursos Hídricos
de la
UNIVERSIDAD NACIONAL DEL LITORAL

2015

Comisión de Posgrado, Facultad de Ingeniería y Ciencias Hídricas, Ciudad Universitaria, Paraje ”El Pozo”, S3000, Santa Fe, Argentina.

HYDROMETEOROLOGICAL FORECASTS AND THEIR SENSITIVITY TO LAND COVER CHANGES

Omar Vicente Müller

Workplace:

CEVARCAM - FICH - UNL
Centro de Estudios en Variabilidad y Cambio Climático
Facultad de Ingeniería y Ciencias Hídricas
Universidad Nacional del Litoral

Thesis advisor:

Ernesto Hugo Berbery — Earth System Science Interdisciplinary Center/Cooperative Institute for Climate and Satellites-Maryland - University of Maryland

Thesis co-advisor:

Norberto Oscar García — CEVARCAM - FICH - UNL

Evaluation committee members:

Silvina Alicia Solman* — *Centro de Investigaciones del Mar y la Atmósfera - Universidad de Buenos Aires
Moira Evelina Doyle* — *Centro de Investigaciones del Mar y la Atmósfera - Universidad de Buenos Aires
Marcelo Daniel Nosetto — Instituto de Matemática Aplicada - Universidad Nacional de San Luis

Dissertation submitted to the Postgraduate Department of the
FACULTAD DE INGENIERIA Y CIENCIAS HIDRICAS
of the
UNIVERSIDAD NACIONAL DEL LITORAL
in partial fulfillment of the requirements for the degree of
DOCTOR EN INGENIERIA - MENCION RECURSOS HIDRICOS

2015

I dedicate this dissertation to the memory of my father, Omar. He graduated from high school with honors at the age of 50. Is there a better example of commitment to self-improvement?

Acknowledgements

I would like to thank all those who contributed, supported and encouraged me throughout my dissertation research. All of you have been essential to achieving this goal.

A deep appreciation to Dr. Hugo Berbery, my advisor, who guided me with the same patience as a school teacher guides a first grade child. His humility, honesty and his passion for science have fed my admiration for him. Furthermore, I am grateful to Dr. Norberto García, my co-advisor, for trusting in a computer engineer and giving me a chance in the world of the natural sciences.

I would like to thank Dr. Domingo Alcaraz-Segura for his valuable help and enthusiasm, and to my colleagues at CEVARCAM, for their companionship and collaboration. Especially to Leandro, Miguel, Diego and Carlos, with whom we have walked together towards the doctorate.

My thanks must also go to my workplace at the Facultad de Ingeniería y Ciencias Hídricas (FICH), UNL, as well as to the Cooperative Institute for Climate & Satellites (CICS-MD) at the University of Maryland and to the Land Surface Hydrology Research Group at the University of Washington, for welcoming me during my visits.

I want to thank my wife Guadalupe, my daughters Oriana and Brisa, who supported me with love during the hard way of a doctorate, especially for making me feel close when the distance separated us.

Also, I would like to thank my mother María, my siblings Valeria, Maricel and Juan Ignacio and their families, as well as my in-laws for always being attentive to my doctorate and giving me encouragement to do it. “Omar, how are your studies going?, Are you finishing?, When is the graduation?”, were common questions during these years. Finally, I can say I did it!

Lastly, I want to acknowledge the financial support of a grant from Consejo Nacional de Investigaciones Científicas y Técnicas (CONICET), and the partial funding of the following projects: PICT 2008-1576 of the Agencia Nacional de Promoción Científica y Tecnológica, and projects CRN2094, CRN3035 and CRN3095 from the Inter-American Institute for Global Change Research (IAI), which is supported by the U.S. National Science Foundation.

Hydrometeorological Forecasts and Their Sensitivity to Land Cover Changes

Omar Vicente Müller

Advisor: Ernesto Hugo Berbery
Co-Advisor: Norberto Oscar García

Abstract

Sea surface temperature (SST) anomalies are recognized as the main driver of extremes in southern South America. Also, regional feedbacks between land surface conditions and the overlying atmosphere play an important role modulating droughts or persistent wet spells. However, the regional feedbacks are not fully understood. Currently, many atmospheric models have simplified land surface schemes that employ fixed land-cover maps or vegetation types along with tables of their corresponding biophysical properties. Using a fixed land-cover classification does not account for interannual changes of those properties due to, for example, excess or deficit of precipitation. This representation of vegetation functioning may result in delayed responses in the atmospheric signal, and reduces the ability of models to represent rapid changes including land-use shifts, floods, or droughts.

In the same manner as plant species can be grouped into plant functional types, terrestrial ecosystems can be grouped into Ecosystem Functional Types (EFTs). EFTs are groups of ecosystems that share functional characteristics in relation to the amount and timing of the exchanges of matter and energy between the biota and the physical environment. In other words, EFTs are patches of the land surface that exchange mass and energy with the atmosphere in a common way. Since EFTs can be defined from Normalized Difference Vegetation Index (NDVI) fields on an annual basis, the year-to-year variability of the surface conditions can thus be identified. In this work, we examine the use of Ecosystem Functional Types as an alternative to Land Cover Types in simulations of regional climate in La Plata Basin (LPB).

Several experiments were done with the Weather Research and Forecasting Model (WRF) model in order to understand the land-atmosphere interactions

in the region. First, the WRF model was carried out for a 11-years period (2000-2010). The objectives were to have a reliable high resolution climatology and to assess the model proficiency in represent the regional climate with the current parameterizations. The results shows that the model is able to properly simulate the regional climate and variability. Nevertheless, WRF in general tends to present drier conditions in LPB, and thereby, it has difficulties in identify severe droughts.

Then, the experiments continue with a deep analysis of the severe Argentine drought that began in late 2007 and lasted until early 2009. The study is based in a comparison of WRF simulations with conventional Land Cover Types, and simulations with the proposed Ecosystem Functional Types used as lower boundary conditions. The results show that the use of realistic information of vegetation states enhances the model performance, reducing the precipitation biases over the drought region and over areas of excessive precipitation. The temperature simulation shows a generalized increase that has a beneficial effect toward the eastern part of the domain with a notable reduction of the bias, but not over the central region where the bias is increased. The overall results suggest that an improved representation of the surface processes may contribute to improving the predictive skill of the model system.

With the ultimately aim to translate the acquired knowledge about regional climate modeling to practical information for different users and stakeholders, a real-time forecasts and monitoring system is developed. Particularly the system is tailored specifically for users in regions of high agricultural productivity and water needs. The effort aims to add value with respect to other systems in the region offering tools with graphical information in a unified system based on numerical simulation. The evaluation of the forecasts skill shows an accuracy of about 70% average in the prediction of occurrence of daily precipitation, and about 85% of correlation in the forecasts of daily temperature. Beyond the scores, the system output is used as input of an early warning system for flows and as a support of the local daily weather report. Also, regular users check the system daily to know the extended forecasts. In all cases the users value positively the utility of the system and recognize it as a key tool for their particular objectives.

Contents

List of Figures

List of Tables

Preface

The climate is a determining factor for our society, the global economy and the nature. In this regard, the climate of La Plata Basin is vital for the quality of life and economy of the region. This basin is one of the most densely populated regions of South America, where harvests and livestock are among the region's most important assets. In the last decades, different parts of the basin were affected by climate change that modified precipitation frequency and intensity patterns. These changes favored the agricultural expansion towards the west, but also increased the occurrence of floods and droughts.

Undoubtedly, it is very important for the scientific community to advance in the regional climate modeling towards a correct reproduction of this reality, and translate it into useful knowledge and predictive skill for decision making and sustainable development. There have been many advances in modeling the effects of ocean-atmosphere interactions in the region, but land-atmosphere interaction still is not well understood. It is probably because land surface processes are not correctly represented in models. Modeling studies that consider land cover changes show that biophysical properties of vegetation may modify significatly the surface conditions of a region, and thereby affect the overlying atmospheric states. However, many numerical models for weather forecasting that consider the atmosphere and land surface as a coupled system, represent vegetation in a simplified way with land cover types fixed in time. Hence, they are insensitive to any vegetation variability. In order to include biosphere processes and their effects over the atmosphere, it is desirable that climate models represent the vegetation dynamics.

From the above introduction several questions arise: What are the strengths and weaknesses of climate models to represent the regional climate of La Plata Basin? How much do the region's land cover and land use changes influence the climate? Can a more realistic representation of land cover improve the predictability of the region? Can the agricultural expansion intensify or prolong droughts or wet spells originated by La Niña or El Niño events? How can the knowledge on the regional climate modeling be translated into useful tools for decision making?

This research will seek to answer these questions and lays the foundations

for the development of tools to support decision making. The work begins with an assessment of a model climatology of La Plata Basin. Then, the role of land cover changes is examined and a new approach to realistically represent land cover in models is presented and evaluated with the objective of contributing to improve the region predictability. Finally, an operational system of forecasting and monitoring of hydrometeorological variables is designed and developed.

Chapter 1 | Introduction

1.1 Background

The climate system in South America has great variability at different time and spatial scales. Complex processes and interactions among atmosphere, land and ocean play fundamental roles in the climate variability and predictability. Hence, their understanding is essential to advance in new approaches that improve the skill of models.

The main features of South America's climate are related to regional forcings like orography (Andes Mountains) and diabatic heating (summer monsoon). The Andes Mountains are the most important geographical factor determining low level circulations, as they effectively block air transport in the zonal direction (westerlies in middle latitudes, easterlies near the tropics). A related and intrinsically connected element is the South American Low Level Jet (SALLJ) (Virji, 1981). The Andes Mountains define the SALLJ path, that flows southeastward along the eastern side of the mountains. The SALLJ appears to be present most of the year (Nogués-Paegle and Berbery, 2000; Berbery and Barros, 2002) carrying moisture to the southern part of the basin.

The extension of the monsoon over the South Atlantic is known as the South Atlantic Convergence Zone (SACZ) (Kodama, 1993; Carvalho et al., 2004). It extends southeastward along the northeastern boundary of the LPB. It has convergent winds across southeast Brazil into the southwest Atlantic Ocean. Plentiful moisture supply from the Atlantic maintains a precipitation maximum over central Brazil defining the monsoon system.

The climate variability in southern South America —and particularly extreme events— recognize as the main driver the Pacific Ocean sea surface temperature (SST) anomalies, especially those associated with the El Niño Southern Oscillation (ENSO) phenomenon (Ropelewski and Halpert, 1987; Aceituno, 1988; Mechoso and Perez Iribarren, 1992; Müller and García, 2010). Positive SST anomalies over the tropical Pacific (El Niño) are known to induce wet spells over southern South America, and conversely, a cold tropical Pacific (La Niña) favors dry conditions. The effect of the Pacific Ocean anomalies is enhanced by

the North Tropical Atlantic when they are in opposite phases. For example, a cold Pacific (La Niña) complemented with a warm North Tropical Atlantic induces a distinct drought pattern with a noticeable increase in the anomalies' magnitude (Seager et al., 2010; Mo and Berbery, 2011).

Important physical factors, like the land cover that varies from tropical forests in Amazonia to high altitude deserts in the Bolivian Altiplano, also play a critical role in the regional climate. This diverse coverage has experienced large changes in the last decades, either human-induced or of natural origin.

Southeastern South America has shown a positive trend in annual precipitation during the second half of the twentieth century, as reported by (Krepper and Zucarelli, 2010) and Doyle et al. (2012). The increase of precipitation has been accompanied by greater interannual variability in precipitation, which increases not only the risk of flood events but also of droughts with their consequent negative impacts (Penalba et al., 2010).

Brazil, Paraguay, Argentina, and Uruguay are countries whose economy relies mostly on rain-fed agriculture. The increase of precipitation in arid regions combined with technological advances and new conditions of the global market has favored the expansion of the agricultural frontier, increasing the availability of productive lands. Large areas of native forests, savannas and grasslands suffered deforestation and land-clearing, with the purpose of exploiting them in agriculture and cattle ranching (Dros, 2004; Paruelo et al., 2005). E.g., the dry forests of the subtropical zone of the continent experienced a reduction of 12% of their area between 1980 and 2000 Baldi et al. (2008). Further, there were observed changes in crop types. E.g., the soybean production has increased significantly, substituting crops like sorghum and rye. But not only deforestation processes were detected, tree afforestation for wood production was reported by different authors. E.g., Baldi and Paruelo (2008) have demonstrated the afforestation on both margins of the Uruguay River in Argentina and Uruguay as a result of economic and political incentives. Geary (2001) discusses the sustainability of the increase in forest industry in Uruguay.

All such changes in surface coverage have a direct impact on land surface processes. They are recognized as a potential source of climate variability, predictability and change at different time scales, from hours to seasons and longer (Sellers et al., 1992; Koster et al., 2000; Foley et al., 2000; Koster and Suarez, 2003; Guo-Shuai et al., 2011). Changes in the land surface or vegetation cover can affect the way the land and the atmosphere interact at many of those time scales and can thus have an effect on climate. Changes in the surface states result from land use and land cover changes, either from natural or anthropocentric origin, or from climate conditions that affect the vegetation health and its phenology. Abundant evidence based on model simulations has been offered on the impacts of land cover changes on regional to global climate (see,

e.g., Mahmood et al., 2010; Pielke et al., 2007, and references therein).

While the interactions between ocean and atmosphere that influence in the regional climate are reasonably understood and properly represented in model simulations, the relation between land and atmosphere is not fully understood, especially in our region. These interactions require a correct representation of the land cover in models (Betts et al., 1996; Ge et al., 2007) and several efforts have been reported with positive results. In the most elaborate approach, climate models are being coupled to highly complex dynamical vegetation models with explicit representation of physiological and biogeochemical processes (e.g. Smith et al., 2001; Levis et al., 2004). However, in most cases, the processes are handled by simpler and more empirical approaches to avoid high computer requirements.

Practical approaches may consist on the use of realistic representation of surface variables, e.g., as derived from satellite observations. Kurkowski et al. (2003) and Jiang et al. (2010) have found that the use of near real-time fractional vegetation coverage derived from satellite data in model simulations tends to reduce both the near surface temperature and dew point biases. Likewise, the use of a realistic leaf area index translates into increases of potential predictability of evaporation in tropical and forested areas, although the impact on potential predictability of near surface temperature is smaller and in some places even negative (Weiss et al., 2012).

Tian et al. (2004a,b) indicated that a better representation of vegetation leads to a more realistic surface albedo, of which impacts on climate are well documented. Their results also show that new estimates of leaf area index, Plant Functional Types and fractional vegetation cover from Moderate Resolution Imaging Spectroradiometer (MODIS) improve the absorption and partitioning of energy between canopy and soil, reducing the model biases. A shortcoming of this approach is that not all biophysical variables are estimated from satellites, and their computation by alternative means may lead to imbalances or biases in the models.

Numerical experiments using the Community Climate System Model have been carried out to test new land surface parameters based on MODIS data, showing that results are sensitive to the changes in land surface. But while there are improvements in the simulation of precipitation and near surface temperature, large biases still remain (Lawrence and Chase, 2007). These mixed results are not uncommon in studies of vegetation-atmosphere feedbacks, and are a demonstration of the complexity of representing realistically the land surface in climate models.

Despite the overall evidence indicating that a more realistic representation of surface conditions reduce model biases, many current numerical models,

particularly those used for operational forecasts, still employ fixed land cover types. Hence they are unable to represent the additional sources of interannual variability due to land cover changes, either as a result of land use changes or the vegetation's degree of stress (e.g., during droughts, wet periods, or insect outbreaks). In other words, models that do not include changes in land cover may have a limited representation of the land surface-atmosphere feedbacks and consequently on their effects on the regional climate.

South America is a region where climate models tend to have difficulties to properly reproduce the patterns and magnitude of precipitation (e.g. Silvestri and Vera, 2008; Solman et al., 2008; Rusticucci et al., 2010). The reasons are not fully understood, but contributing factors are assumed to be the misrepresentation of the actual land cover types and the consequent inadequate simulation of the land-atmosphere interactions. This study aims at improving the predictive skill in models over this region and at developing methods to transfer this knowledge into applied tools to support decision making.

The hypothesis of this work is that a realistic representation of the land cover properties helps improve the simulation of the land surface-atmosphere interactions and hence can reduce model biases that are inherent to surface processes. In this regard, the study proposes, develops and applies a consistent set of annually varying biophysical properties of vegetation derived from satellite data. This new set is a replacement of the conventional land cover types for southern South America in the Weather Research and Forecasting (WRF) model coupled with the Noah Land Surface Model (LSM). The new set, based on the concept of ecosystem functioning is named Ecosystem Functional Types (EFTs), and takes into account the functional properties of terrestrial ecosystems, as identified using a top-down approach of MODIS measurements of vegetation greenness.

Lee et al. (2013a,b) explored the sensitivity of climate variables to the use of time-varying ecosystem properties as a replacement of the invariant land cover types, with promising results for 3-months WRF simulations. It is expected that surface effects will be more noticeable during a situation when the surface states depart noticeably from their predefined properties, as during a major drought period. In this work the hypothesis is tested for the real world case of a prolonged drought event that took place in southern South America. Other regions within the model domain had excess of precipitation giving the opportunity to examine the land-atmosphere interactions and surface effects during very different conditions.

1.2 Objectives

In relation to the issues described above, the main objectives of this dissertation are to:

- Investigate current strengths and weaknesses of the WRF regional model in representing the regional climate of La Plata Basin.
- Perform research to better understand the processes that lead to an improved predictability of the regional climate, specifically by using a more realistic and consistent set of time-varying land cover biophysical properties in the regional model.
- Improve the understanding of the impact of land cover/land use changes over physical processes related to LPB hydro-climate.
- Develop predictive capabilities by implementing a real-time forecasting and monitoring system that produces practical information for the users and stakeholders, particularly in agricultural and water management activities.

1.3 Dissertation Outline

This dissertation is divided in six chapters. Chapter 1 introduces the regional climate, and reviews the influence of land surface conditions on climate. The hypothesis and objectives are then presented. Chapter 2 reviews the parameterizations and vegetation representation currently used by regional models. It also presents the basis of the novel approach suggested to represent vegetation in models. Chapter 3 discusses the current skill of the WRF/Noah model to represent the climate of LPB. Chapter 4 analyses the severe drought of 2008 in the Lower LPB contrasting simulations of WRF/Noah model using conventional Land Cover Types against the novel approach with Ecosystem Functional Types introduced in Chapter 2. Chapter 5 presents the development of a real-time forecasting and monitoring system and evaluate the system forecasts performance. Finally, Chapter 6 summarizes the main conclusions of this dissertation and presents and outlook for future work.

Chapter 2 | Regional and Coupled Models: Land Surface Representation

2.1 Introduction to Regional Coupled Models

General circulation models (GCMs) must deal with atmospheric processes in three dimensions, and need to ingest information from the lower boundary conditions including analyses of ocean surface temperatures and land surface processes. In parallel, studies of the oceans and land surface focus on their corresponding three-dimensional properties. With the evolution of climate modeling, it was of interest of the scientific community to couple these three dimensional components to simulate the behavior of the climate system over lengthy periods. At the interfaces, the atmosphere is coupled to the land and oceans through exchanges of heat, moisture and momentum. These models of the climate system are usually known as coupled GCMs. Further coupling of other climate system component models, especially the cryosphere and the biosphere, are also necessary to obtain more realistic simulations of climate on decadal and longer timescales.

Coupled GCMs allow to simulate the general circulation and processes around the Earth, but usually fail to represent or predict processes at regional scales because of their coarse spatial resolution. One technique to "zoom in" is that of nested modeling, giving place to regional climate models (RCMs). This involves the linking of models of different scales within a global model to provide increasingly detailed analysis of local conditions while using the general products of the global model as a driving force for the higher resolution model. Results for a particular region from a coupled GCM are used as initial and boundary conditions for the RCM, which operates at much higher resolution in time and space and often, with more detailed representation of local forcings (e.g., topography) and physical parameterization. This enables the RCM to be used to enhance the detailed regional model climatology and this down-scaling can be extended to even finer detail in local models. This procedure is particularly attractive for mountain regions and coastal zones, as their complexity is unresolved by the coarse structure of a coupled GCM grid.

2.2 The *Weather Research and Forecasting* Model

The Weather Research and Forecasting Model is a regional model based in what 10 years ago were the two most popular and advanced regional models in use (Eta and MM5). At the time, the National Center for Atmospheric Research (NCAR) and the National Centers for Environmental Prediction (NCEP) made a concerted effort to unify them into one model that would take advantage of the strongest points each of the models had. Thus, WRF was born. At present, and among the available RCMs, WRF is by far the most used model by the worldwide community of climate modelers and users. The reasons are that, unlike for other models, WRF is developed as an open source model by a large community of experts contributing to each of the specific components of the model. The fact that the distribution is centralized at NCAR avoids the risks of developing parallel versions and guarantees that all portions of the model will be properly linked. NCAR also maintains an up-to-date documentation and provides help support of unparalleled quality.

The WRF model is a mesoscale numerical weather prediction system. It is currently in operational and research use around the world. The development of WRF has been a multi-agency effort to build a next-generation mesoscale forecast model and data assimilation system. The goals of this effort are to advance the understanding and prediction of mesoscale weather and accelerate the transfer of research advances into operations. The model is suitable for a broad span of applications across scales ranging from meters to thousands of kilometers. Such applications include real-time numerical weather prediction, data assimilation development and studies, parameterized-physics research, regional climate simulations, air quality modeling, atmosphere-ocean coupling, and idealized simulations. For more detailed information about WRF see Michalakes et al. (2004), Skamarock et al. (2008) or visit the web site www.wrf-model.org.

Technically, the WRF model has a framework that provides the infrastructure that includes the dynamics solvers, physics packages that interface with the solvers, programs for initialization, WRF-Var, and WRF-Chem. The dynamics solver define diffusion, damping and advection options. They include algorithms for computation of pressure gradient and Coriolis force terms and mass divergence, advection schemes, thermodynamics processes, horizontal diffusion, divergence damping, and coupling of the sub-grids, boundary conditions, and nesting capability, as well as the transport of various scalars such as moisture variables, etc. The physics packages are between solver-dependent routines: a pre-physics preparation and post-physics modifications of the tendencies. The physics preparation involves filling arrays with physics-required variables such as temperature, pressure, heights, layer thicknesses, and other state

variables. Physics packages compute tendencies for the velocity components, potential temperature, and moisture fields. The solver-dependent post-physics step will re-stagger these tendencies as necessary, couple tendencies with coordinate metrics, and convert to variables or units appropriate to the dynamics solver. WRF-Var is a variational data assimilation system, which can ingest a host of observation types in pursuit of optimal initial conditions, while WRF-Chem model provides a capability for air chemistry modeling.

There are two options for the dynamics solver component: The Advanced Research WRF (ARW) solver (originally referred to as the Eulerian mass solver) developed primarily at NCAR, and the Nonhydrostatic Mesoscale Model (NMM) solver developed at NCEP. These solvers define two separate models, WRF-ARW and WRF-NMM respectively, where both share the rest of the components, but differ in the dynamic solver. In this research the WRF-ARW (henceforth simply WRF) is used. The modules for data assimilation (WRF-Var) as well as for chemistry modeling (WRF-Chem) are not used in this study.

2.2.1 Governing Equations

The governing equations to represent the behavior of the atmosphere on climate models are usually called primitive equations. They are a set of nonlinear differential equations forming a system of seven equations with seven unknowns with specified boundary conditions. The equations can be found in most books of climate dynamics or atmospheric modeling such as Peixoto and Oort (1992), Hartmann (1994), Rayner (2001), Holton et al. (2004), or Jacobson (2005). A general formulation of the system is given by the following equations:

- equation of motion:

$$\frac{d\mathbf{V}}{dt} = -\frac{1}{\rho}\nabla p - (2\mathbf{\Omega} \times \mathbf{V}) - \mathbf{g} + \mathbf{F}, \tag{2.1}$$

- equation of continuity:

$$\frac{1}{\rho}\frac{d\rho}{dt} + \nabla \cdot \mathbf{V} = 0, \tag{2.2}$$

- equation of state of moist air:

$$p = \rho R_d T(1 + 0.61q), \tag{2.3}$$

- thermodynamic equation:

$$c_v \frac{dT}{dt} + p\frac{d\alpha}{dt} = Q, \tag{2.4}$$

- and equation of conservation of water vapor:

$$\frac{dq}{dt} = B \tag{2.5}$$

where $\mathbf{V}$ is the three-dimensional velocity with its u=zonal, v=meridional, and w=vertical components, the term $2\boldsymbol{\Omega} \times \mathbf{V}$ represents the Coriolis force, $\mathbf{g}$ is the gravity force, $\mathbf{F}$ are forcing terms from model and turbulent physics, ρ is the density, p is the pressure, R_d is the gas constant for dry air, T is the temperature, while the term $T(1 + 0.61q)$ means virtual temperature being q the specific humidity of water vapor. Then, c_v denotes the specific heat capacity, $\alpha = 1/\rho$ the inverse of density, and Q the heat flow. Finally, B represents flow through the boundaries of a parcel, i.e., the difference between evapotranspiration (source) and condensation (sink).

Note that equation 2.1 can be expanded in three scalar equations, one for each component of vector $\mathbf{V}$, completing the system of seven equations. The basic predicted variables are $\mathbf{V} = (u, v, w)$, ρ, p, T and q. The equation system may appear in different forms, however it still consists of seven equations composed of seven variables. For instance, the technical report of the ARW dynamics solver of WRF model (Skamarock et al., 2008) states the system of equations in flux form using a terrain-following mass vertical coordinate following the philosophy of Ooyama (1990). Here, the system was expressed in its most general form.

2.2.2 Model Parameterization

The use of the WRF-ARW model does not only require the configuration related with the domain and the spatial and temporal resolutions, but also the choice of several parameterizations related to the physics and dynamics. The most important parameterizations are those linked to the physics. The model offers multiple physics options that range from simple and efficient, to sophisticated and computationally costly, but also from novel schemes to well-known schemes. A brief description is given of those physics options that are relevant for surface processes, which are the core of our research:

- Microphysics: It represents the physics governing the growth and evolution of clouds and aerosol particles. It includes explicitly resolved water vapor, cloud, and precipitation processes.
- Cumulus Convection: These schemes are responsible for the sub-grid-scale effects of convective and/or shallow clouds. The schemes are intended to represent vertical fluxes due to unresolved updrafts and downdrafts and compensating motion outside the clouds. They operate only on individual columns and provide the convective component of surface rainfall.
- Surface Layer: The surface layer schemes calculate friction velocities and exchange coefficients that enable the calculation of surface heat and mois-

ture fluxes by the land-surface models and surface stress in the planetary boundary layer scheme.

- Land Surface Model (LSM): The LSMs use atmospheric information from the surface layer scheme, radiative forcing from the radiation scheme, and precipitation forcing from the microphysics and convective schemes, together with internal information on the land's state variables and land-surface properties, to provide heat and moisture fluxes over land points and sea-ice points. These fluxes provide a lower boundary condition for the vertical transport done in the planet boundary layer schemes. The land-surface models have various degrees of sophistication in dealing with thermal and moisture fluxes in multiple layers of the soil and also may handle vegetation, root, and canopy effects and surface snow-cover prediction. The land-surface model updates the land's state variables which include the ground (skin) temperature, soil temperature profile, soil moisture profile, snow cover, and possibly canopy properties. There is no horizontal interaction between neighboring points in the LSM, so it can be regarded as a one-dimensional column model for each WRF land grid-point, and many LSMs can be run in a stand-alone mode.

- Planet Boundary Layer (PBL): The PBL is responsible for vertical sub-grid-scale fluxes due to eddy transports in the atmospheric column. Thus, when a PBL scheme is activated, explicit vertical diffusion is de-activated with the assumption that the PBL scheme will handle this process. The surface fluxes are provided by the surface layer through the land-surface schemes. The PBL schemes determine the flux profiles within the well-mixed boundary layer and the stable layer, and thus provide atmospheric tendencies of temperature, moisture (including clouds), and horizontal momentum in the entire atmospheric column.

- Atmospheric Radiation: The radiation schemes provide atmospheric heating due to radiative flux divergence and surface downward longwave and shortwave radiation for the ground heat budget. Longwave radiation includes infrared or thermal radiation absorbed and emitted by gases and surfaces. Upward longwave radiative flux from the ground is determined by the surface emissivity that in turn depends upon land-use type, as well as the ground (skin) temperature. Shortwave radiation includes visible and near-visible wavelengths that make up the solar spectrum. Hence, the only source is the Sun, but processes include absorption, reflection, and scattering in the atmosphere and at surfaces. For shortwave radiation, the upward flux is the reflection due to surface albedo.

As Skamarock et al. (2008) highlight, the model physics parameterizations are presented individually, but it is evident that there are many interactions

between them via the model state variables (potential temperature, moisture, wind, etc.) and their tendencies, and via the surface fluxes (shortwave/longwave radiation, heat/moisture flux, etc). Particularly, the biophysical properties of land cover are directly or indirectly involved in many parameterizations described above. These properties are defined by the LSM and directly affect the surface layer, whose friction velocities vary with the roughness length, and the atmospheric radiation that depends on emissivity and albedo. Moreover the surface fluxes of heat and moisture also depend on these properties, then the planetary boundary layer and the cumulus convection parameterization are indirectly related to those properties.

2.3 The Noah Land Surface Model

The Noah LSM is selected among the LSMs available in the WRF model. This LSM is an intermediate complexity model coupled to the WRF model, with a cost/benefit (computational cost/quality of simulation) that positions it as the best option for operational forecasts. The Noah LSM is the successor to the OSU LSM described by Chen and Dudhia (2001). The scheme was developed jointly by NCAR and NCEP, and is applicable for research and operational purposes.

As explained in Section 2.2.2 and as shown in Figure 2.1 the model uses atmospheric and radiation forcing, together with internal information on the land's state variables and land-surface properties, to provide heat and moisture fluxes over land points and sea-ice points. These fluxes provide a lower boundary condition for the vertical transport done in the PBL.

The LSM has four soil layers with a corresponding thickness from the top down of 10, 30, 60 and 100 cm (2 m total depth), and includes representations of the root zone, vegetation categories, monthly vegetation fraction, and soil texture, among others. The Noah LSM additionally predicts soil ice, and fractional snow cover effects; it has an improved urban treatment, and considers surface emissivity properties. This LSM simulates soil moisture (both liquid and frozen), soil temperature, skin temperature, snowpack depth, snowpack water equivalent (and hence snowpack density), canopy water content, and the energy flux and water flux terms of the surface energy balance and surface water balance (Mitchell et al., 2005).

A brief description of model equations is done following the formulation of Chen and Dudhia (2001). Basically the model equations can be separated in three parts: model thermodynamics, model hydrology and model snow and sea-ice.

The model thermodynamics determine the surface energy balance representing the combined ground-vegetation surface. The ground heat flux is con-

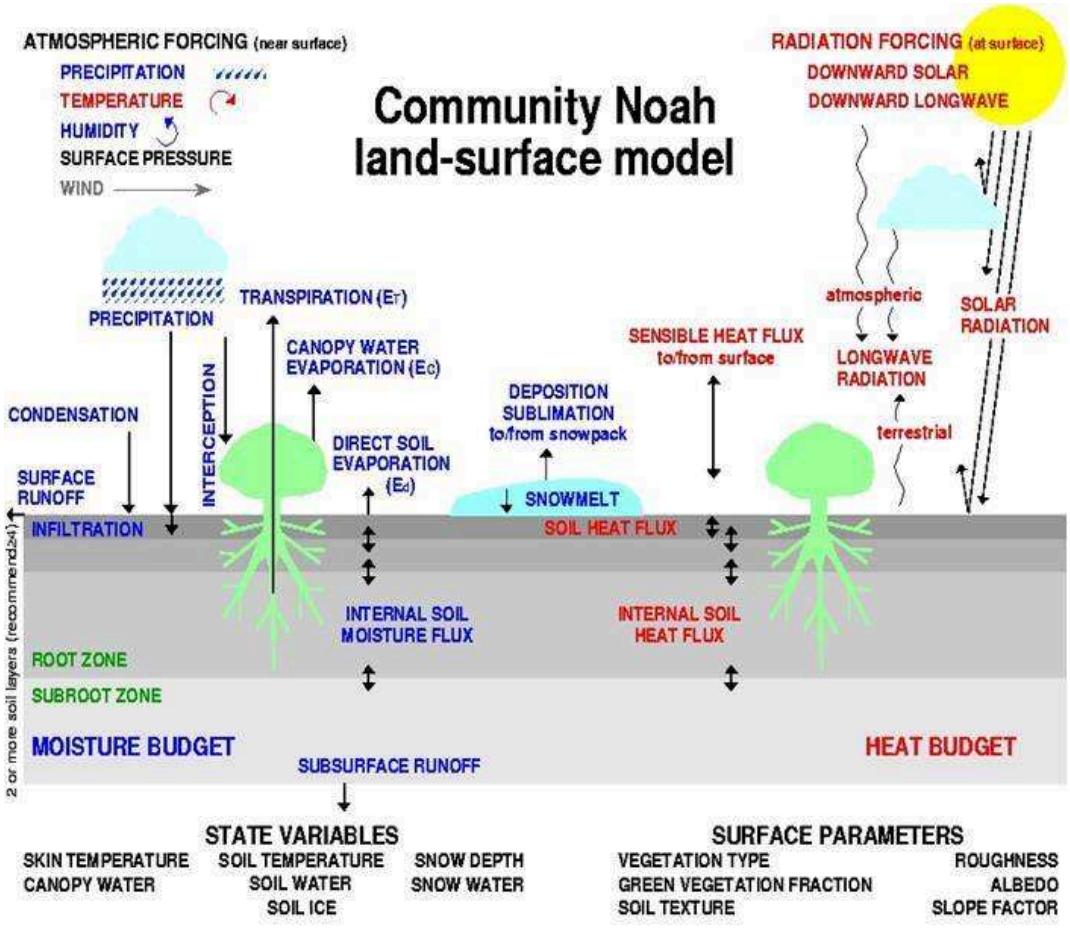

Figure 2.1: Schematic diagram of the Noah LSM indicating the water and energy balance as well as forcings, state variables and parameters. Source ldas.gsfc.nasa.gov/nldas/NLDAS2model.php.

trolled by the usual diffusion equation for soil temperature (T_s):

$$C\frac{\partial T_s}{\partial t} = \frac{\partial}{\partial z}\left(K_t\frac{\partial T_s}{\partial z}\right), \tag{2.6}$$

where the volumetric heat capacity C and the thermal conductivity K_t are formulated as functions of volumetric soil water content or simply soil moisture (SM), which in turn depend on the soil texture. Then, the layer-integrated form of 2.6 for the ith soil layer is:

$$\Delta z_i C_i\frac{\partial T_{s_i}}{\partial t} = \left(K_t\frac{\partial T_s}{\partial z}\right)_{z_{i+1}} - \left(K_t\frac{\partial T_s}{\partial z}\right)_{z_i}. \tag{2.7}$$

The last term in 2.7 represents the surface ground heat flux in the top layer and is computed using the surface skin temperature.

The prognostic equation for volumetric soil moisture content (SM) is given by:

$$\frac{\partial SM}{\partial t} = \frac{\partial}{\partial t}\left(D\frac{\partial SM}{\partial z}\right) + \frac{\partial K_h}{\partial z} + F_{SM} \tag{2.8}$$

where the soil water diffusivity D and the hydraulic conductivity K_h are functions of SM. F_{SM} represents sources and sinks (i.e., precipitation, evapotranspi-

ration, runoff, etc.) for soil water. Integrating 2.8 over four soil layers, as used in Noah LSM, and expanding F_{SM}:

$$d_{z_1}\frac{\partial SM_1}{\partial t} = -D\left(\frac{\partial SM}{\partial z}\right)_{z_1} - K_{h_{z_1}} + P_d - R - E_{dir} - E_{t_1} \quad (2.9)$$

$$d_{z_2}\frac{\partial SM_2}{\partial t} = D\left(\frac{\partial SM}{\partial z}\right)_{z_1} - D\left(\frac{\partial SM}{\partial z}\right)_{z_2} + K_{h_{z_1}} - K_{h_{z_2}} - E_{t_2} \quad (2.10)$$

$$d_{z_3}\frac{\partial SM_3}{\partial t} = D\left(\frac{\partial SM}{\partial z}\right)_{z_2} - D\left(\frac{\partial SM}{\partial z}\right)_{z_3} + K_{h_{z_2}} - K_{h_{z_3}} - E_{t_3} \quad (2.11)$$

$$d_{z_4}\frac{\partial SM_4}{\partial t} = D\left(\frac{\partial SM}{\partial z}\right)_{z_3} + K_{h_{z_3}} - K_{h_{z_4}} \quad (2.12)$$

where d_{z_i} is the ith soil layer thickness, P_d the precipitation not intercepted by the canopy, and E_{t_i} the canopy transpiration taken by the canopy root in the ith layer within the root zone layers. The surface runoff R is defined as the excess of precipitation not infiltrated into the soil. The total evapotranspiration $EVT = E_{dir} + E_c + E_t$ is the sum of direct evaporation from the top shallow soil layer (E_{dir}), evaporation of precipitation intercepted by the canopy (E_c), and transpiration via canopy and roots (E_t). The three terms forming EVT are functions of potential evaporation E_p and green vegetation fraction (GVF). Green vegetation fraction acts as a critical weighting coefficient between the components of EVT (Chen et al., 1996). Also, E_t is a function of stomatal resistance, rooting depth and leaf area index (LAI). Stomatal resistance controls the amount of water that the leaves can lose by transpiration, and LAI is the fraction of ground area covered by green leaves.

The snow model has one layer of snow cover and simulates the snow accumulation, sublimation, melting, and heat exchange at snow layer interfaces. The heat flux between the soil and the snow is estimated by:

$$G = K_t\frac{T_0 - T_s}{D_{sn}} \quad (2.13)$$

where K_t is the thermal diffusivity for snow, T_0 the skin temperature, T_s the temperature in the first soil layer, and D_{sn} the snow depth. The skin temperature T_0 can be calculated by solving the surface energy balance equation:

$$(1-\alpha)S\downarrow + L\downarrow - \epsilon\sigma T_0^4 = G + SHF + LHF \quad (2.14)$$

where α is albedo, $S\downarrow$ and $L\downarrow$ are the downward short- and longwave surface radiation, ϵ is emissivity and σ is the constant of Stefan-Boltzmann, while the terms on the right-hand side are the snow, sensible, and latent heat fluxes.

An extended version of Noah LSM equations can be found in Chen et al. (1996) and Chen and Dudhia (2001), but what this brief review intends to highlight is the dependence of model equations with biophysical properties defined by the vegetation cover parameterization. For instance, green vegetation

fraction is critical for the partitioning of total evapotranspiration, stomatal resistance, root depth and leaf area index also affect the computation of model hydrology. On the other hand, the roughness length modifies the wind speed involved in heat flux equations, and albedo determines the shortwave radiation reaching the surface. Then, a realistic definition of these biophysical parameters may help improve the LSM performance and thereby the overall simulation results.

2.4 Land Cover Representation in the WRF/Noah Framework

The Noah LSM prescribes a dominant land cover type and its associated biophysical properties to each grid point following the classification system suggested in Anderson (1976). In this way, each grid point has defined a dominant land cover category that is constant in time (Li et al., 2013). Then, a set of 15 biophysical properties are assigned to that land cover type through a look-up table. In other words, the look-up table prescribes the values of all properties for each land cover category.

By default the model uses a set of 27 land cover categories that was generated by the United States Geological Survey (USGS) Center for Earth Resources Observation and Science, the University of Nebraska-Lincoln, and the Joint Research Centre of the European Commission. The map was derived from the NOAA Advanced Very High Resolution Radiometer (AVHRR) images collected daily over a 12-month period from April 1992 through March 1993 with 1 km resolution (Eidenshink and Faundeen, 1994). The International Geosphere Biosphere Program is an alternative classification available in the Noah LSM. It offers 20 categories based on MODIS satellite data from October 2000 to October 2001.

In both cases (USGS and IGBP) the land cover data is available at different spatial resolution: 30-arc-second, 2-, 5-, and 10-arc-minutes. The Figure 2.2 shows as example the land cover categories of USGS (Figure 2.2a) and IGBP (Figure 2.2b) with the coarsest resolution for the region of interest. Although the classifications work with different categories, the maps present the same general distribution of land covers. Major differences are found in the Dry Chaco, where USGS classifies it as savanna and grassland, while IGBP identifies broadleaf forest and savanna. Also, IGBP replaces the cropland/woodland mosaics and grasslands by croplands in central Argentina. Lastly, IGBP identifies many more urbanized locations than USGS, mainly in Brazil.

Note that in each map the grid cells with the same color have the same dominant land cover category. Then, these pixels share the same set of properties

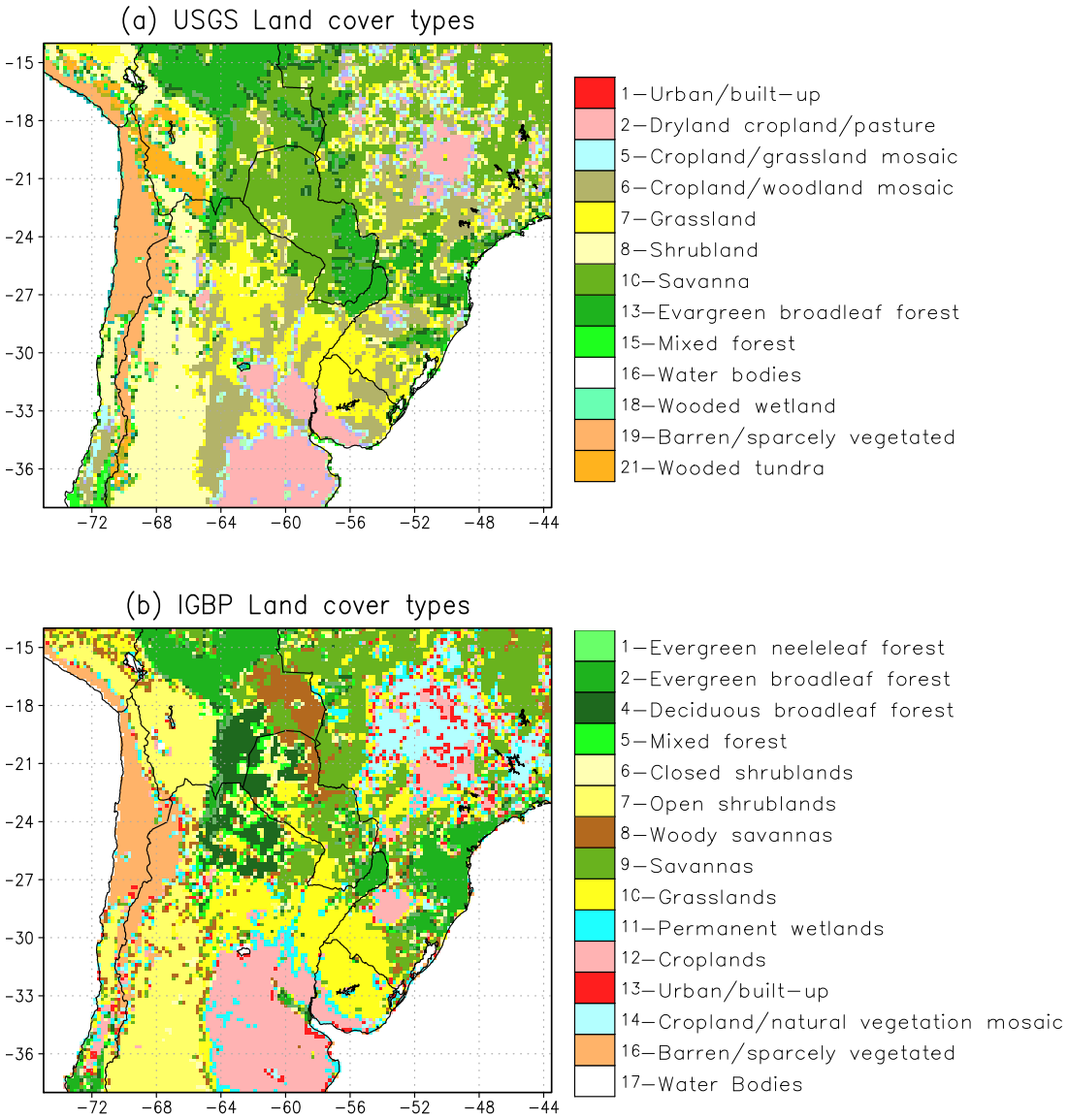

Figure 2.2: Conventional land cover representation in Noah LSM for 10-arc-minute resolution a) USGS classification and b) IGBP classification. The legends show only categories appearing in the region.

in any simulation. I.e., the properties are not only constant in time, but also in space when different grid cells get the same category (color) anywhere in the world.

The 15 properties linked to each category are presented in Table 2.1. The Appendix A presents the lookup tables that define the values of this set of properties for each land cover classification: USGS and IGBP. Once the classification is chosen in the model configuration, the categories and the values of the properties remain constant during the simulation.

As was explained above, one important limitation of this approach is that the properties assigned to a given land cover category are invariant in time, or are bound by fixed minimum and maximum values. For instance, each land cover is assumed to have the same constant properties during a drought or a

Property	Notation	Units
Green vegetation fraction	GVF	—
Rooting depth (soil layer index)	i	—
Stomatal resistance	rs	sm^{-1}
Parameter used in radiation strees function	rgl	—
Parameter used in vapor pressure deficit function	hs	—
Threshold water-equivalent snow depth that implies 100% snow cover	$snup$	m
Upper bound on maximum albedo over deep snow	α_{sn}	%
Minimum leaf area index through the year	LAI_{mn}	—
Maximum leaf area index through the year	LAI_{mx}	—
Minimum background emissivity through the year	ϵ_{mn}	—
Maximum background emissivity through the year	ϵ_{mx}	—
Minimum albedo through the year	α_{mn}	—
Maximum albedo through the year	α_{mx}	—
Minimum roughness length through the year	$Z0_{mn}$	m
Maximum roughness length through the year	$Z0_{mx}$	m

Table 2.1: Biophysical properties used by Noah LSM.

wet spell, and at any location classified with the same category.

The exchanges of energy, water, and momentum between the land surface and the atmosphere depend on the land surface biophysical properties. Consequently, changes in land cover will also affect those exchanges with expected impacts on the climate conditions. The inclusion of realistic land cover information in LSMs is relatively new, but particularly relevant for southern South America, where the replacement of native vegetation, e.g., by croplands, has extensively occurred in recent years (Volante et al., 2012).

2.5 Ecosystem Functional Types (EFTs)

In order to overcome the shortcomings noted above, the concept of time-varying ecosystem functioning is presented in this dissertation. The description focuses in the conceptual differences with the conventional method to represent the land cover highlighting the potential advantages. Then, the model sensitivity to the use of time-varying ecosystem properties as a replacement of the invariant land cover types will be investigated in Chapter 4.

The origin of EFTs is based on the functional attributes of ecosystems that characterize the energy and matter exchange between the biota and the atmosphere (Valentini et al., 1999). These attributes show a quicker response to environmental changes than structural ones (McNaughton et al., 1989) and are relatively easy to monitor using satellite-derived spectral indices (Paruelo et al., 2001). The representation of the vegetation variability from attributes that show sensitivity to any kind of change and that are easy to get from satellite data makes this approach attractive for the ecological community. On this research the approach is extended and adapted to work in regional models.

2.5.1 Definition

Formally, EFTs are defined as *groups of ecosystems that share functional characteristics in relation to the amount and timing of the exchanges of matter and energy between the biota and the physical environment* (Paruelo et al., 2001; Alcaraz et al., 2006). In other words this means that an EFT represents a region where the exchanges of mass and energy between the surface and the atmosphere are homogeneous.

Since EFTs are defined from descriptors of the Normalized Difference Vegetation Index (NDVI) dynamics on an annual basis, the year-to-year variability of the surface conditions can thus be identified (Alcaraz-Segura et al., 2013b). Based on these concepts, Alcaraz et al. (2006); Alcaraz-Segura et al. (2013a) developed a method to define EFTs on a yearly basis. Therefore, intermediate and long-term ecological phenomena and land surface processes are better represented, i.e., EFTs reflect vegetation changes resulting from either land use or natural changes.

2.5.2 Computation

Following the above studies, EFTs are computed using three metrics of the NDVI seasonal dynamics (see Figure 2.3):

(a) NDVI-I: the annual mean of NDVI as an estimator of net primary production;

(b) CV: the seasonal coefficient of variation of NDVI as a descriptor of seasonality (difference between the growing and non-growing season, or amplitude of the annual cycle); and

(c) DMAX: the time of the year when NDVI achieves its absolute maximum value as a phenological indicator of the growing season.

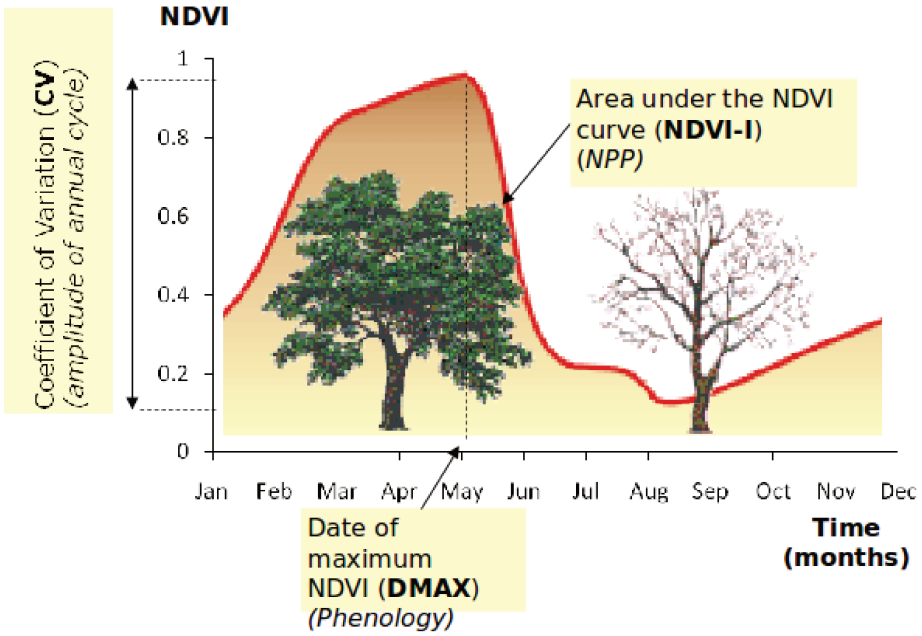

Figure 2.3: Conceptual example of an annual cycle of NDVI and the three metrics considered to compute the EFTs. It was obtained from lechusa.unsl.edu.ar and modified by Domingo Alcaraz-Segura.

For practical reasons (see Alcaraz et al., 2006; Alcaraz-Segura et al., 2013a) the range of values of each NDVI descriptor was divided into four fixed intervals, giving a potential number of $4^3 = 64$ categories. To divide the range of values of the NDVI annual mean into four categories, its three quartiles were obtained for each year and then, for each quartile, the median across years was calculated. The same applies to the seasonal coefficient of variation. Lastly, the four categories for the date of maximum NDVI correspond to the four seasons of the year in temperate ecosystems.

The EFTs categories are identified with codes of three characters, one for each descriptor, following the convention suggested by Paruelo et al. (2001). The definition and coding of EFTs allow for an ecological interpretation of the legend in terms of the three NDVI metrics: The first character, an uppercase letter from A to D, identifies the net primary productivity from low to high. The second character, a lowercase letter from a to d, represents decreasing seasonality (amplitude of the annual cycle). The last character, a number from 1 to 4, corresponds to the season of the maximum NDVI, where spring is associated with 1 and sequential numbers for the following seasons.

The EFT map presented in Figure 2.4d shows an example of spatial patterns of ecosystem functioning in temperate southern South America for the year 2001. The EFT map captures in a concise way the spatial variability of the three integrative descriptors of ecosystem functioning: productivity (Figure 2.4a), seasonality (Figure 2.4b), and phenology (Figure 2.4c) allowing an ecological interpretation.

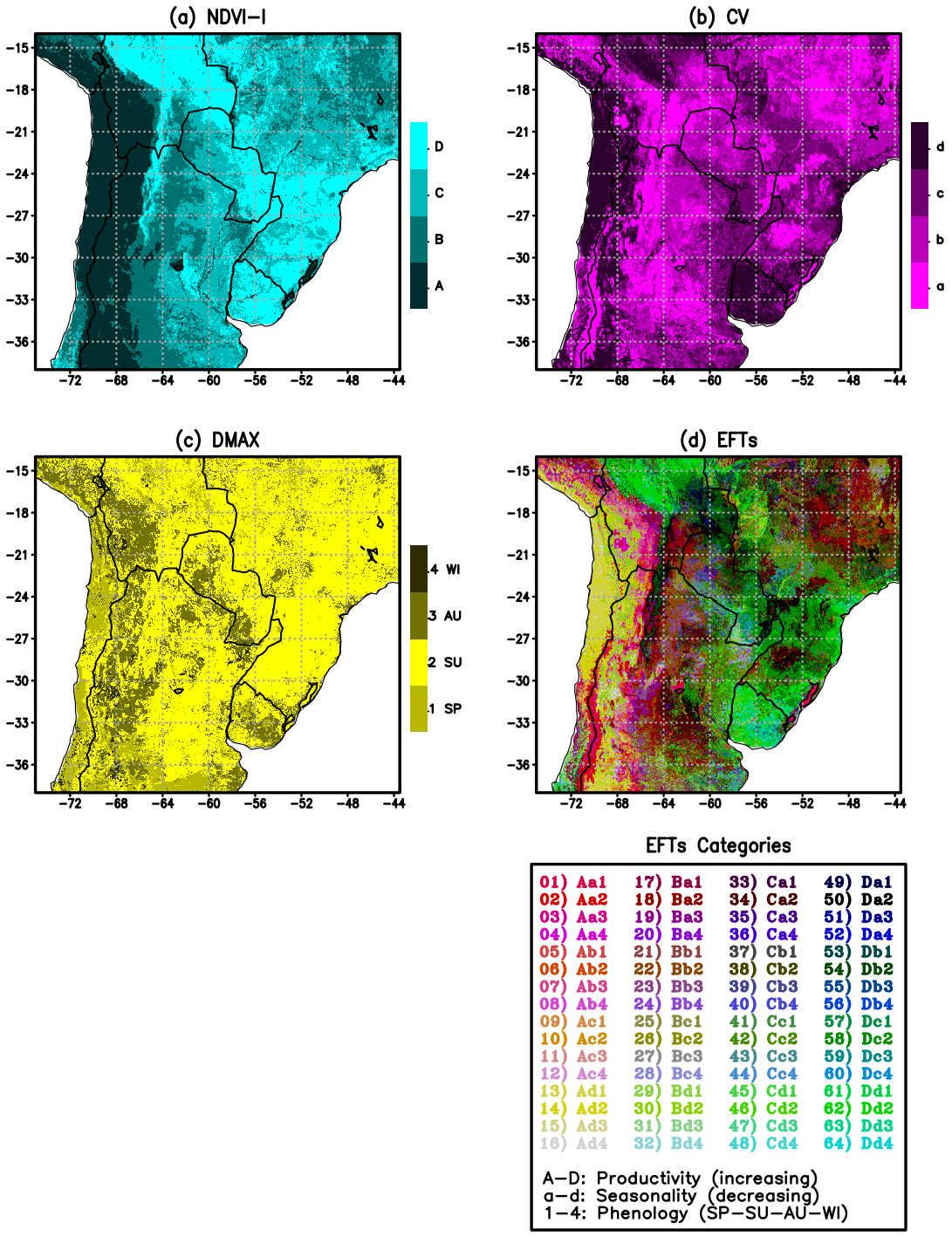

Figure 2.4: Spatial distribution of 2001 EFTs and the metrics that make up them. The maps show (a) the NDVI annual mean (NDVI-I), (b) seasonal coefficient of variation NDVI (CV), (c) date of the maximum NDVI (DMAX), and (d) resulting EFTs and the legend with the full definition of all ecosystem functional types/colors.

From Figure 2.4 it is possible identify that, for instance, subtropical rainforests have high productivity, low seasonality and summer maxima, which correspond to an EFT identified as Dd2. Soybean plantations in the dry Chaco forest have relatively low productivity, very high seasonality and summer maxima, which correspond to an EFT identified as Ba2. The Atacama desert, on

the other hand, has very low productivity, very low seasonality and spring to summer maximum, which corresponds to EFTs defined as Ad1 to Ad2. The Humid Pampas have relatively high productivity, very low to low seasonality and a summer maximum, which corresponds to EFT categories Ca2 and Cb2.

2.6 A Consistent Set of Time-Varying Biophysical Properties

The Noah LSM defines a table of 15 biophysical properties for each land cover category. Following the method described in Appendix B, an analogous table of properties can be obtained for the EFTs categories. The method was applied using the properties of Noah LSM for the IGBP classification over the MODIS land-cover classes (MCD12C1 product, collection 5) (product details in Friedl et al., 2002, 2010).

Basically, the proposed method matches for a given year the EFTs map with the 15 parameters maps derived from MODIS classes. Then, the EFTs parameters are computed as spatial average of those property values sharing the same EFT class. At this point there are a different table of properties for each year. In order to unify them, they are averaged in time. Further details and discussion are provided in Appendix B.

Since EFTs are time varying for a given location, their properties (that is, the land surface properties) will be time varying too. It ensures that the full set of properties change in a consistent manner with land cover states.

In order to highlight the differences of the new approach with other alternatives, annual minimum and maximum albedo from different sources were contrasted for four different locations for the period 2001-2009. Following the IGBP classification, the locations are identified as: croplands (two places), grasslands and savanna. The albedo estimates[1] are:

a) MODIS — Product MCD43C3, shortwave, used as reference;
b) IGBP LC-derived — From look-up table provided by the Noah LSM;
c) MODIS LC-derived — Computed as for IGBP LC but using the time-varying MODIS land cover types, product MCD12C1; and
d) EFTs-derived — Derived in this study.

[1]The Noah LSM uses one broadband albedo, while MODIS has different bands (visible, near infrared, shortwave, etc.). The conversion of the different bands to one broadband albedo is out of the scope of this study. It implies that while the comparison is not straightforward, it allows to assess the basic characteristics of the variables' time evolution. We used the MODIS shortwave albedo for our assessment since it is the closest to the Noah albedo.

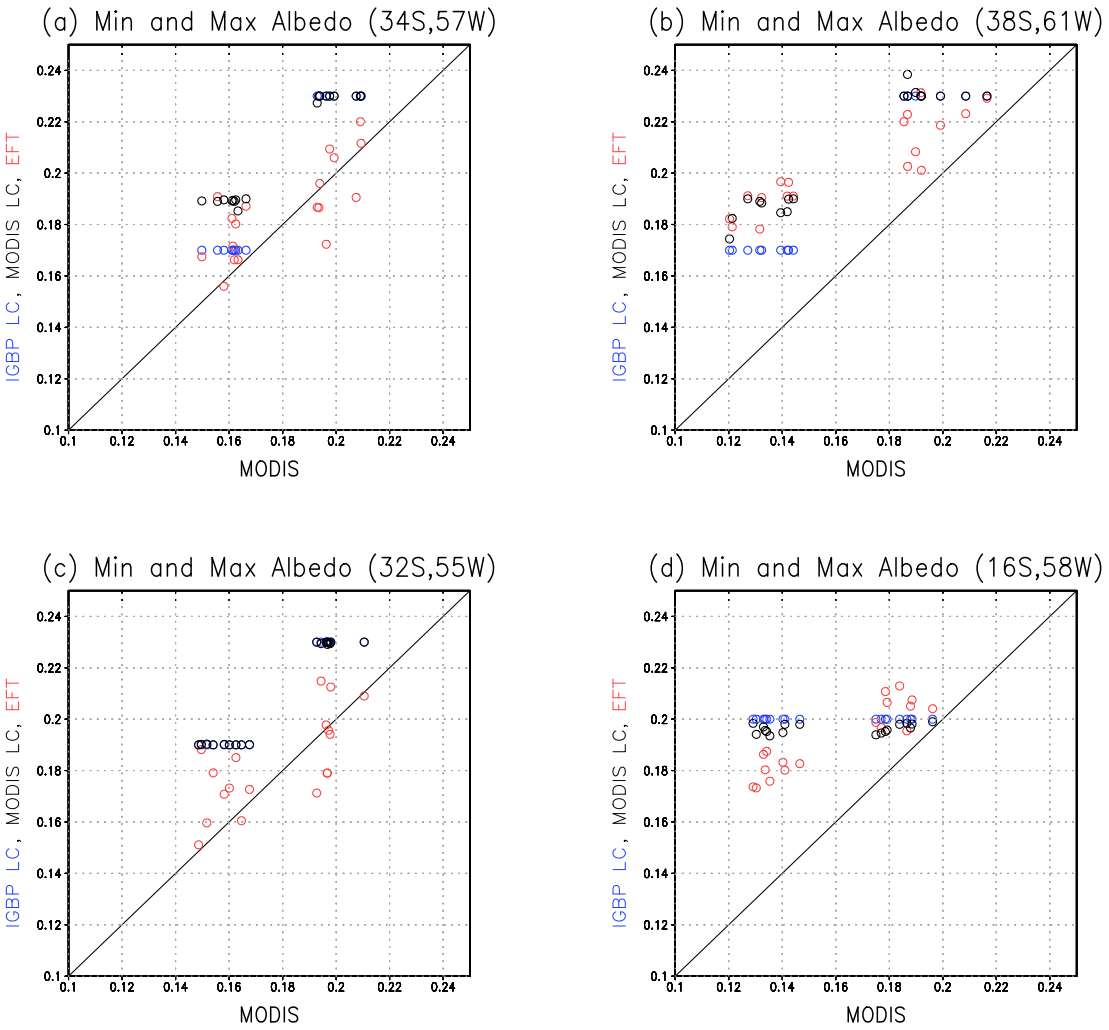

Figure 2.5: Scatterplots of MODIS albedo (product MCD43C3, x-axis) vs albedo derived from IGBP Land Cover categories (blue); vs albedo derived from MODIS Land Cover product MCD12C1 (black); and vs albedo derived from EFT categories (red). The IGBP Land Cover categories defined for the selected points are: (a) Croplands (34S, 57W); (b) Croplands (38S, 61W); (c) Grassland (32S, 55W); (d) Savanna (16S, 58W). The values are annual minimum and maximum albedo for the period 2001-2009

Figure 2.5 presents the scatterplots at the four locations, where it can be noted that the EFT albedo estimates (red circles) are closer to the MODIS albedo, but they are closer to it than are the IGBP LC or MODIS LC albedo estimates (blue and black circles respectively). That is, they tend to have a better correspondence with observations than the other estimates.

Figure 2.6 also shows that the time series of EFT albedo, MODIS LC albedo and IGBP LC albedo tend to overestimate the MODIS albedo, but, in general, the EFT albedo estimate tends to be closer to the MODIS albedo than the rest. As expected, EFT albedo for these specific places has a time evolution that is closely negatively correlated to the NDVI evolution.

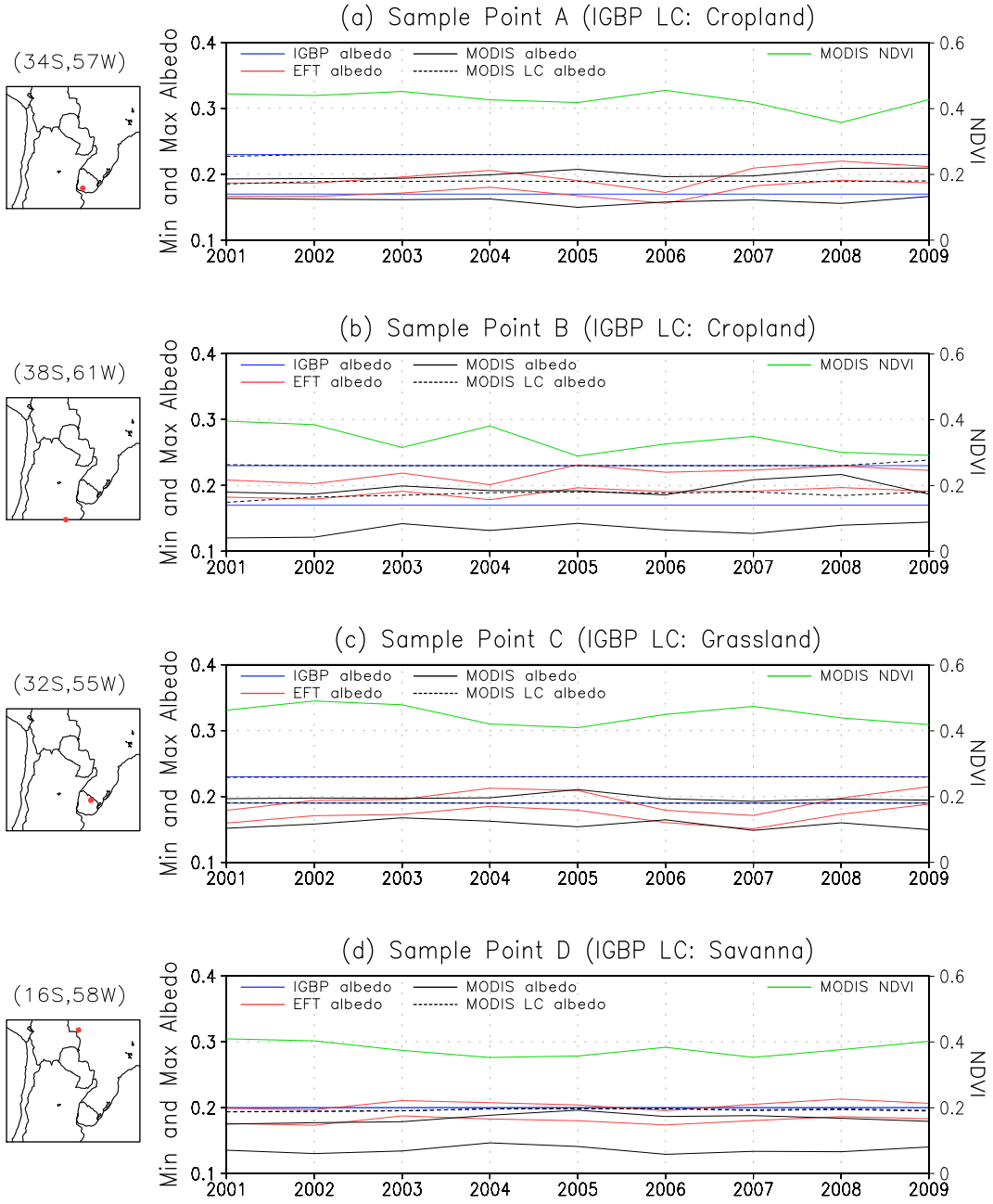

Figure 2.6: Time-series of NDVI from MODIS (product MOD13C2), MODIS albedo (product MCD43C3), albedo derived from IGBP Land Cover categories, albedo derived from MODIS Land Cover (product MCD12C1), and albedo derived from EFT categories.

In summary, the EFT albedo does not always match the evolution of MODIS albedo, but as seen in the time series and scatterplots they tend to have a better correspondence between each other than any of the other estimates. Part of the reason for the improvement may be attributed to the fact that the conventional land cover representation prescribes properties for each land cover regardless of whether it is a wet or dry year. The EFT approach is based on satellite estimated exchanges of mass and energy between land and atmosphere regardless of the land cover type, and therefore the biophysical properties will be sensitive to changes due to a wetter or drier year, even when land cover categories

are assumed to be the same. The examples presented here indicate that EFTs are a helpful approach to represent in a realistic manner the geographical and temporal changes in the land surface biophysical properties.

2.7 Discussion: Land Cover Representations

As noted earlier, one of the limitations of the conventional USGS or IGBP land cover types is that they are constant in time. The use of MODIS land cover categories updated on a yearly basis is an improvement in this respect. Yet, Friedl et al. (2010) report that the MODIS land cover data set has an overall accuracy of about 75% but "the range in class specific accuracies is large". The errors may be larger in regions with scarce or no in-situ information (e.g., southern South America) than over other regions like the US or Europe, where observations can be used to better define parameters.

MODIS also estimates some biophysical properties like green vegetation fraction, leaf area index, and albedo that have begun to be introduced in land-surface and climate modeling to depict more realistically some land surface processes (Miller et al., 2006; Weiss et al., 2012). However, there are other parameters like rooting depth or surface roughness length that should change consistently with the modified properties, but for which there are no satellite estimates. Additionally, the MODIS leaf area index is derived from other MODIS products including the MODIS land cover which, as noted by Friedl et al. (2010), may be subject to uncertainties.

In this work, greenness vegetation fraction, leaf area index and albedo are derived from EFT values along with all the other biophysical parameters to maintain the consistency among them and avoid mixing approaches. In this way, the data set has consistent changes in all properties corresponding to a unique physical indicator (the EFT values). The purpose of this study is to show improvements over a current version of the WRF/Noah model that is of common use.

Note that with the conventional approach it is also possible to increase the number of land cover types to better represent shifts in crop types (see Beltrán-Przekurat et al., 2012), something that has occurred intensively in the region of interest (changes within the cropland category have involved soy bean, alfalfa, wheat, among other crop types). Moreover, the version of WRF model released on July 2014 (version 3.6) offers a mosaic/tiling approach where a certain number of tiles, each representing a land cover category, is considered within each grid cell (Li et al., 2013; Wang et al., 2014). Then, the properties are assigned as a weighted average. Nevertheless, assigning physical properties to each subcategory, as well as, identify the percentage of coverage of different

land cover types in a grid cell may be hard to achieve.

In our case, the EFT properties are derived from the smaller number of land cover types, which is done as weighted averages for each pixel. Per se, this may not provide additional information, however, EFTs include in their definition a representation of vegetation status by means of the primary production, annual amplitude, and phenology of the NDVI annual cycle at pixel level, ecologically meaningful information that otherwise would not be taken into account.

The definition of EFTs captures the differences in ecosystem functioning within the same land cover type. For instance, it distinguishes dense from open shrublands, or irrigated from rain-fed croplands, by means of their differences in primary production dynamics. With these definitions, yearly changes in EFTs (either land cover changes or inter-annual variability of environmental factors) will have associated a consistent set of yearly biophysical properties (e.g., a dry year with stressed vegetation will have increased stomatal resistance, higher albedo and lower surface roughness, and the opposite during a wet year).

Summarizing the key aspects of the EFTs classification, it is noted that: (a) it is an alternative approach to land cover classification that centers on physical properties that allow to identify patches of land that behave homogeneously in terms of surface-atmosphere energy and biomass exchanges (for a same EFT value). From a climate modeling point of view, this is unique; (b) it is based in concepts of ecosystems functions, energy and carbon exchanges; (c) it can be applied to cases preceding the MODIS period (using AVHRR NDVI); and (d) it provides consistency among changes in all 15 biophysical parameters.

Chapter 3 | A High Resolution Model Climatology of La Plata Basin

3.1 Long-Term Simulations over La Plata Basin

This chapter examines a long-term numerical simulation with the analysis focusing over LPB. The ultimate aim is to have a reliable high resolution model climatology which will allow to understand the model performance in climate mode. In this regard, it is necessary to evaluate current strengths and weaknesses of the regional model in the LPB region. The analysis is based on a description of an 11-year high-resolution simulation, including a discussion of the model biases and an evaluation of extreme events.

There are a variety of studies of LPB climatology based on observations or using land surface models (Berbery and Barros, 2002; Barros et al., 2006; Krepper and Zucarelli, 2010). There are other studies that have examined the climate of regional models, although typically at a lower resolution (e.g., Solman et al., 2008; Nuñez et al., 2009; Solman et al., 2013). However, long-term WRF simulations over LPB have not been developed with the features proposed on this work. Then, this experiment should provide a good background to understand the capacity of the model simulating the regional climate. At the same time it will give a useful model climatology for the remaining experiments. The main features of the simulation are the use of a regional climate model (forced by observed SSTs and involving land-atmosphere coupling) at a high resolution to simulate a decade of the South American climate focusing on LPB.

The performance of the model is evaluated in terms of precipitation, soil moisture and air temperature at 2 m. All three variables were designated as *Essential Climate Variables* by the World Meteorological Organization (2010). The simulation of precipitation is fundamental in the water balance and for the representation of drought events. Models must correctly represent a number of processes (e.g., evapotranspiration, moisture flux convergence) to simulate the patterns of precipitation. Meanwhile, soil moisture acts as a control variable of the flux of heat and water between the land and the lower atmosphere, in particular through regulation of evapotranspiration (Koster et al., 2004; Müller et al., 2014). Also, soil moisture is relevant for a wide range of applications

like meteorological forecasts, agriculture, water resources, ecology, among others. Temperature (with rain) have the greatest impact on natural systems and human activities. It is relevant in many physical processes, such as thermal radiation or water phase changes. Also, an evaluation of extreme events is performed through the analysis of the Standardized Precipitation Index (*SPI*).

3.2 Model and Data sets

3.2.1 Model Configuration

The long-term simulation was carried out with the WRF model with the ARW dynamics solver in its version 3.3. The atmospheric model is coupled with the Noah LSM, as anticipated in sections 2.2 and 2.3 respectively.

The period of simulation starts on January 1, 2000 and extends to December 31, 2010, but results of the first year were discarded in the analysis, as it is considered as spin-up. The simulation was done over South America with a horizontal grid spacing of 45 *km* with a nested domain covering the LPB at 15 *km* grid spacing. Both domains are depicted in Figure 3.1. Note that the largest domain has most of its lateral boundaries over the oceans, ensuring the contribution of the SSTs through the lower boundary conditions.

The lateral boundary conditions of the finer domain are provided by the coarser domain. When a nested domain is chosen there are two important aspects to be considered. First, the grid should have enough grid points to allow stabilization and development of the numerical calculations. Second, the grid should have buffer bands around the region of interest, which are usually discarded in the analysis because they can show unstable output as result of the adaptation to different grid resolutions. These issues are satisfied by the nested domain, which has more than 300,000 grid points, and whose area exceeds at least 2 degrees at each side of the basin.

The nested domain (see Figure 3.1) includes the area of La Plata Basin (in red), which is formed by the subbasin of Paraguay (PAY), Mid-Upper Paraná (MUP), Lower Paraná (LOP) and Uruguay (URU). Also, there are significant topographic features like the Andes Cordillera towards the west, and the Brazilian Highlands towards the northeast of the nested domain. Lowlands and plains complete the domain.

The model physics configuration follows the selection of schemes and options of Lee and Berbery (2012) and Lee (2010) who evaluated the combination of parameters that represent South America's climate with smaller biases. A complete summary of the model configuration including spatial and time configuration, physics schemes (parameterization) is given in Table 3.1.

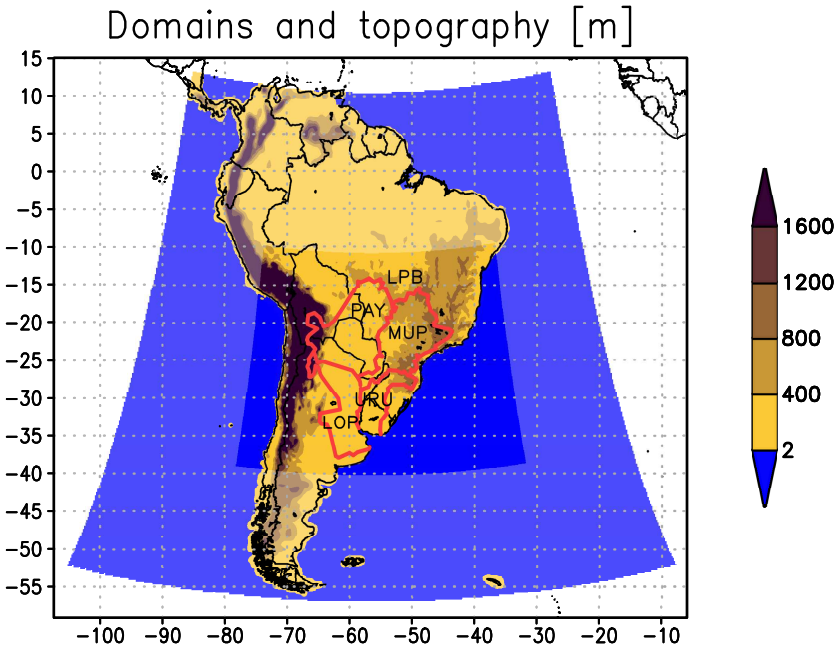

Figure 3.1: Model domains and topography. The largest domain is shown with smoothed colors while the nested domain is highlighted with saturated colors. The red line bounds the LPB and its subbasins: Paraguay (PAY), Mid-Upper Paraná (MUP), Lower Paraná (LOP) and Uruguay (URU).

Parameter	Parent Domain	Nested Domain
Region	South America	LPB
Grid Resolution	45 *km*	15 *km*
Grid Size	502×367 grid points	709×475 grid points
Vertical Levels	28	
Period	2000-2010	
Integration Time Step	240 *sec*	
Dynamic Solver	ARW	
Boundary Condition	CFSR	Parent Domain
Microphysics	Eta Microphysics (Rogers et al., 2001)	
Cumulus Convection	Betts-Miller-Janjic Scheme (Janjic, 1994, 2000)	
Surface Layer	Janjic Eta Scheme (Janjic, 1996)	
Land Surface Model	Noah LSM (Chen and Dudhia, 2001)	
Land Cover Classif.	USGS	
Planet Boundary Layer	Mellor-Yamada-Janjic Scheme (Janjic, 1994)	
Shortwave Radiation	Dudhia Scheme (Dudhia, 1989))	
Longwave Radiation	Rapid Radiative Transfer Mod. (Mlawer et al., 1997)	

Table 3.1: Summary of WRF configuration.

	Levels					
Variable	Depth 4-layers	Surface	MSL	2 *m*	10 *m*	Pressure 37-levels
Geopotential Height						X
Ice Cover		X				
Land Cover		X				
Pressure		X				
Temperature	X	X		X		X
U-component of Wind					X	X
V-component of Wind					X	X
Soil Moisture	X					
Water equiv. of Snow Depth		X				
Pressure reduced to MSL			X			
Relative Humidity				X		X

Table 3.2: CFSR variables and levels at wich fields are defined. Deep levels are 4: 0-10 *cm*, 10-40 *cm*, 40-100 *cm*, 100-200 *cm*. Surface means ground or water surface. MSL is mean sea level. 2 *m* and 10 *m* indicate height above ground. Pressure levels are 37 levels of upper air from 1000 *mbar* to 1 *mbar*.

The model was forced by the initial and 6-hr lateral boundary conditions from the NCEP Climate Forecast System Reanalysis (CFSR) (Saha et al., 2010). Table 3.2 shows the variables of CFSR forcing the simulation. Sea surface temperatures are included in the global reanalysis through the skin temperature.

3.2.2 Evaluation Data Sets

The performance of the model is evaluated with observational data sets either from satellite sources or *in-situ* observations. To evaluate precipitation, NCEP's Climate Prediction Center (CPC) Unified Gauge-Based Analysis of Global Daily Precipitation (Chen et al., 2008) is used. It consists of daily rain gauge observations interpolated to a grid of $0.5^\circ \times 0.5^\circ$ resolution. Also, some figures include the Tropical Rainfall Measurement Mission (TRMM) 3B43 monthly satellite data at $0.25^\circ \times 0.25^\circ$ grid spacing (Huffman et al., 2007).

Soil moisture products are compared against a satellite-derived data set called Essential Climate Variable V2 (ECV V2). It is produced by the European Space Agency (ESA), and combines data from different satellite sources. It has a spatial resolution of $0.25^\circ \times 0.25^\circ$ (Liu et al., 2011).

Temperature at 2 m is evaluated with the CPC global monthly gridded ($0.5^\circ \times 0.5^\circ$ resolution) land-only surface air temperature at 2 m data set (Fan and Van den Dool, 2008). This product is commonly referred to as GHCN-CAMS as it is an analysis based upon station data from both the Global Historical Climatology Network version 2 (GHCN), and the Climate Anomaly Monitoring System (CAMS). Also, the satellite derived temperature product called MOD11C3 from MODIS at $0.05^\circ \times 0.05^\circ$ is used (Wan and Li, 2011).

Henceforth, observational data sets for each variable will be identified in text and figures by the name of the institution that produced them, or the satellite name for products derived from one satellite. I.e. GHCN-CAMS or the global precipitation analysis will be called as CPC (temperature or precipitation respectively), and remotely sensed soil moisture as ESA.

3.3 An examination of the model's surface climate

3.3.1 Precipitation Estimates

The spatial pattern of the time average of observed CPC precipitation (Figure 3.2a) has its maximum in southern Brazil, on the east side of LPB. This wet region, mostly covered by the Upper Paraná Atlantic Forest, has an average precipitation rate of around 5 $mm\,day^{-1}$. The magnitude of daily mean precipitation gradually decreases westward to less than 1 $mm\,day^{-1}$ on top of the Andes Mountains and the desert of Atacama. The northern part of the domain (along the southern part of the Amazon Forest) also shows high precipitation of around 4 $mm\,day^{-1}$.

The simulated precipitation map (Figure 3.2b) captures the main observed features, with high precipitation to the east and north of the domain that gradually decreases towards the southwest. However, the bias map (Figure 3.2c) shows that WRF tends to simulate higher precipitation in mountain-dominated regions like the Andes Cordillera and Brazilian Highlands. These positive biases may be attributable to the topographic complexity of the area, where models exhibit difficulties regardless of the grid spacing. In addition, the Andes Cordillera has very few stations available. When an assimilation system interpolates observations to regular grids, it tends to smooth values in places with little data. Then, the differences over the Andes, could be due to the scarcity of rain gauges. The low values of observed precipitation on this area make the percentage model biases very noticeable on Figure 3.2d.

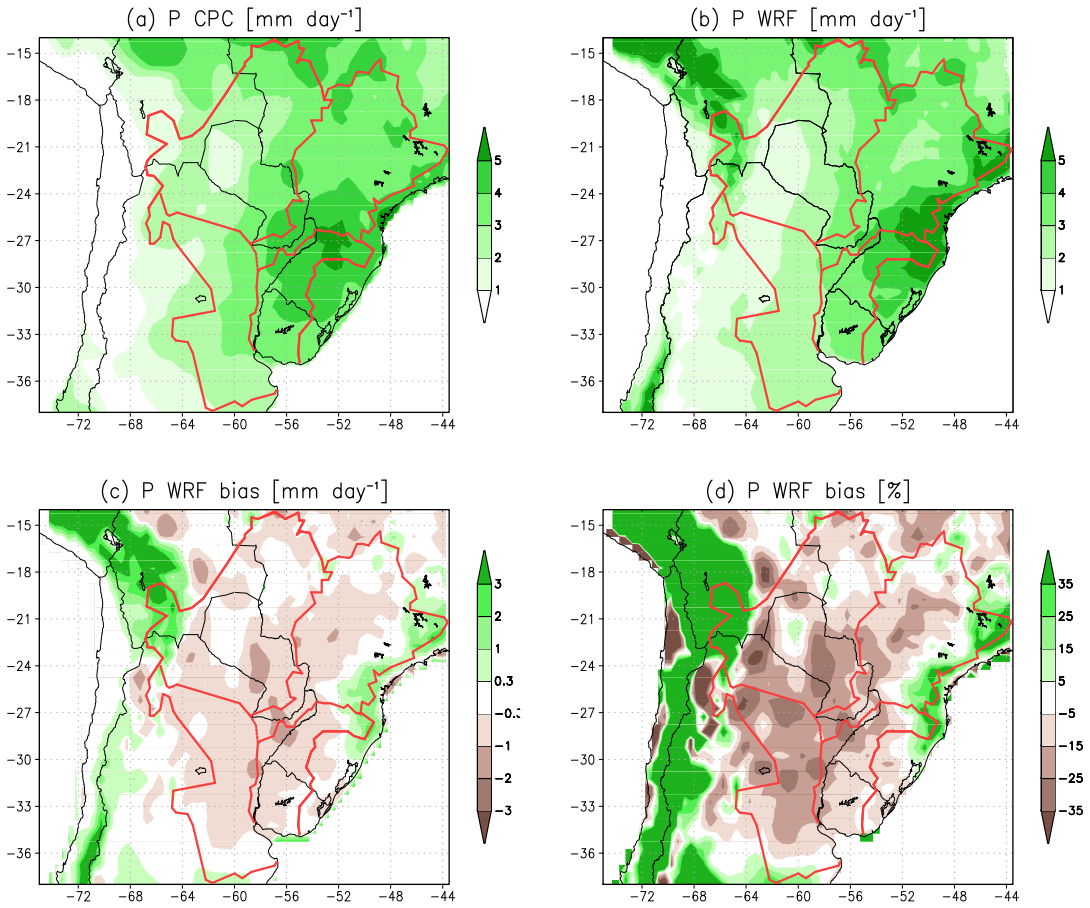

Figure 3.2: Ten years average of (a) observed precipitation based on CPC; (b) simulated precipitation by WRF; (c) model precipitation biases ($WRF - CPC$); and (d) percentage model precipitation biases $(WRF - CPC)/CPC \times 100$.

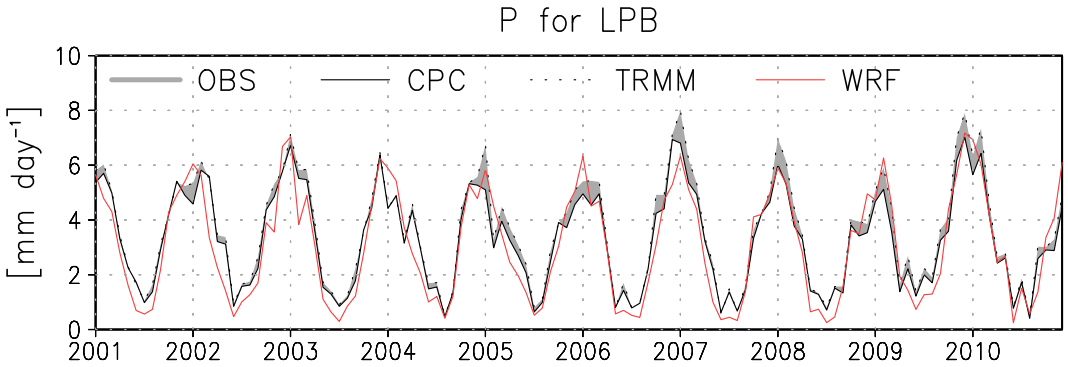

Figure 3.3: LPB areal aveage precipitation for two observational data sets, CPC and TRMM, and simulated by WRF. The grey band marks the observations uncertainty.

In the rest of the domain, mostly occupied by LPB, the model's simulated climate is slightly drier than the observed values. The biases are in general lower than -1 $mm\,day^{-1}$ (Figure 3.2c), but vary from -5 % to -35 % when values are normalized (Figure 3.2d). These negative biases on LPB arise from underestimated precipitation during dry seasons (austral winter) in most years as shown in Figure 3.3. Nevertheless, WRF notably improves the estimation in wet seasons (austral summer) showing almost the same peaks of observations for all

Basin	$RMSE[mmday^{-1}]$	r
La Plata (LPB)	0.76	0.93
Paraguay (PAY)	0.95	0.90
Mid-Upper Paraná (MUP)	1.30	0.90
Lower Paraná (LOP)	0.97	0.88
Uruguay (URU)	1.41	0.77

Table 3.3: Root mean square error ($RMSE$) and correlation coeficient (r) between WRF and CPC time-series of areal average precipitation over LPB and its subbasins.

years. The correlation between WRF and CPC time-series is 0.93 and the *RMSE* is 0.76 considering the whole basin as shown in Table 3.3.

A more detailed analysis of model's precipitation is done with Figures 3.4 and 3.5, where the LPB area is divided in two parts. The northern part of the basin identified as Upper LPB is formed by the Paraguay and Mid-Upper Paraná subbasins; the southern part of the basin called Lower LPB is formed by Lower Paraná and Uruguay subbasins. The left columns of Figures 3.4 and 3.5 present the mean annual cycle of precipitation rate, intensity and frequency for Upper LPB and Lower LPB respectively. The frequency of precipitation is defined as the number of rainy days out of the total number of days. A day is considered with rain when precipitation is 0.25 *mm* [1] or greater. The precipitation intensity is the average rain over rainy days. Scatterplots comparing CPC estimations and WRF simulation of the mentioned aspects of precipitation are shown in the right columns of both figures. Values corresponding to months of the cold season, i.e. from March to August, are plotted in blue, while red circles identify values during the warm season, i.e. from September to February.

The dry biases of WRF during dry/cold seasons is also evidenced in Figure 3.4b where the fit line (blue) is under the 45° line. Particularly, in Upper LPB the annual cycle of WRF is below the observation band from March to September (Figure 3.4a). In general, the model captures the well-defined annual cycle of precipitation but simulates higher variability. The high annual variability is due to the presence of the South America monsoon system present in northeastern LPB (Collini et al., 2008). Beyond the described differences between WRF and CPC, the model precipitation achieves a correlation of 0.90 on cold/dry months and 0.85 on warm/wet months over Upper LPB.

Note that while the precipitation rate in Upper LPB shows great similarities

[1]The criteria to define 0.25 *mm* as threshold is that most gauge stations measure precipitation with bucket pluviometers, which minimum measurable quantity is 0.25 *mm*. Also, many precipitation datasets store data in inches with precision of two decimals, i.e., the minimum value of a rainy day is 0.01 *in*=0.254 *mm*.

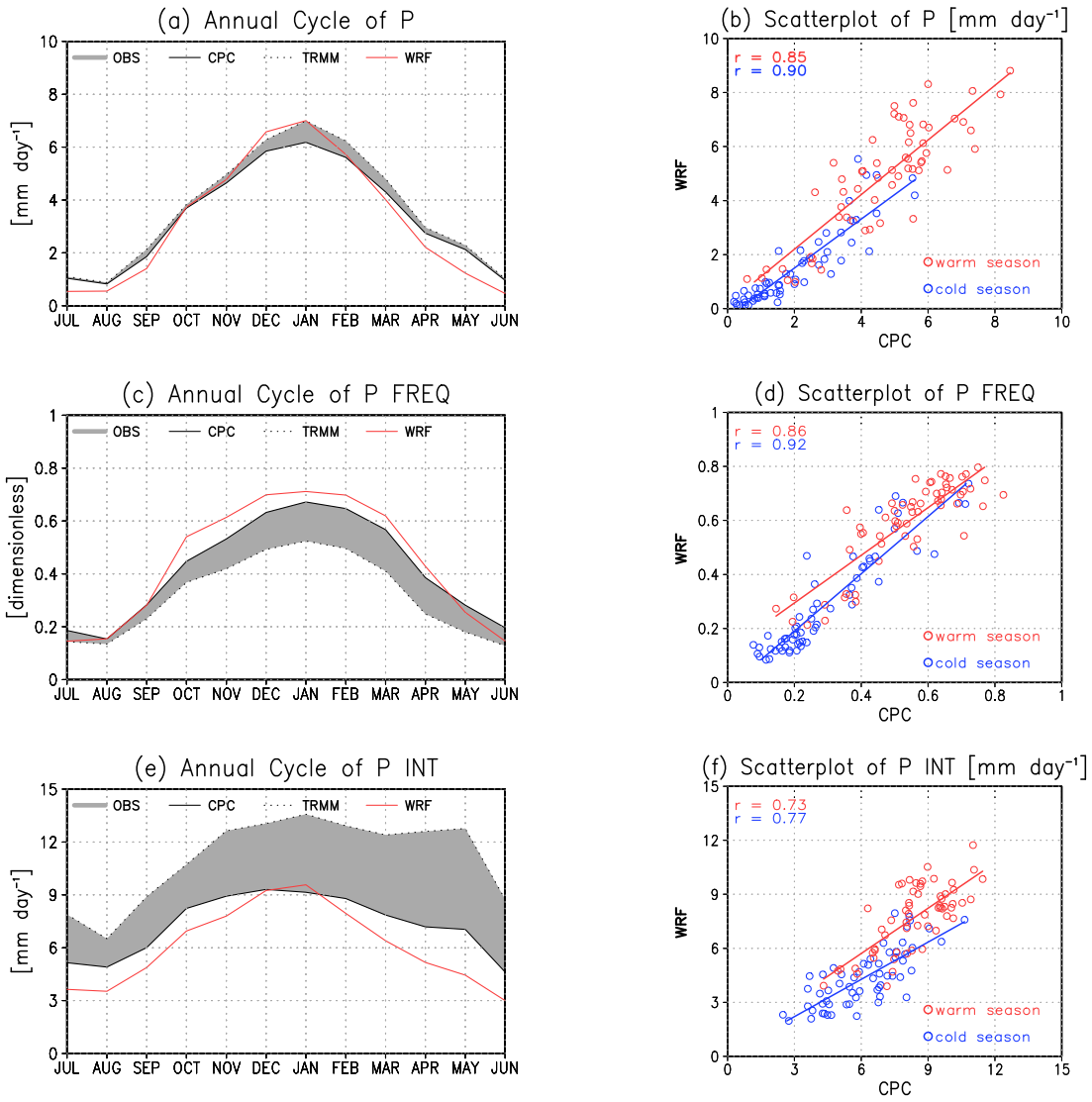

Figure 3.4: Mean annual cycle of Upper LPB (i.e. PAY and MUP) for ten years period of (a) precipitation rate, (b) frequency and (c) intensity and their corresponding scatterplots in (b), (d) and (f) respectively.

between TRMM and CPC curves, the corresponding precipitation intensity and frequency present major differences (see Figures 3.4a and b). Specifically, CPC has more rainy days (higher frequency) than TRMM, but it presents lighter precipitation (lower intensity). The model has a behavior closer to CPC in terms of frequency and intensity but even with more frequent and less intense rainy days. As with the precipitation rate, the correlation of precipitation frequency and intensity is higher during cold seasons than during warm seasons. It suggests that although the higher biases are in dry/cold seasons, the model is able to follow the dry seasons variability.

As for Upper LPB, the annual cycle of precipitation rate for TRMM and CPC in Lower LPB presents a close resemblance (Figure 3.5a), but CPC has more intense and rarer events (Figure 3.5b and c). In this context, the Lower LPB has

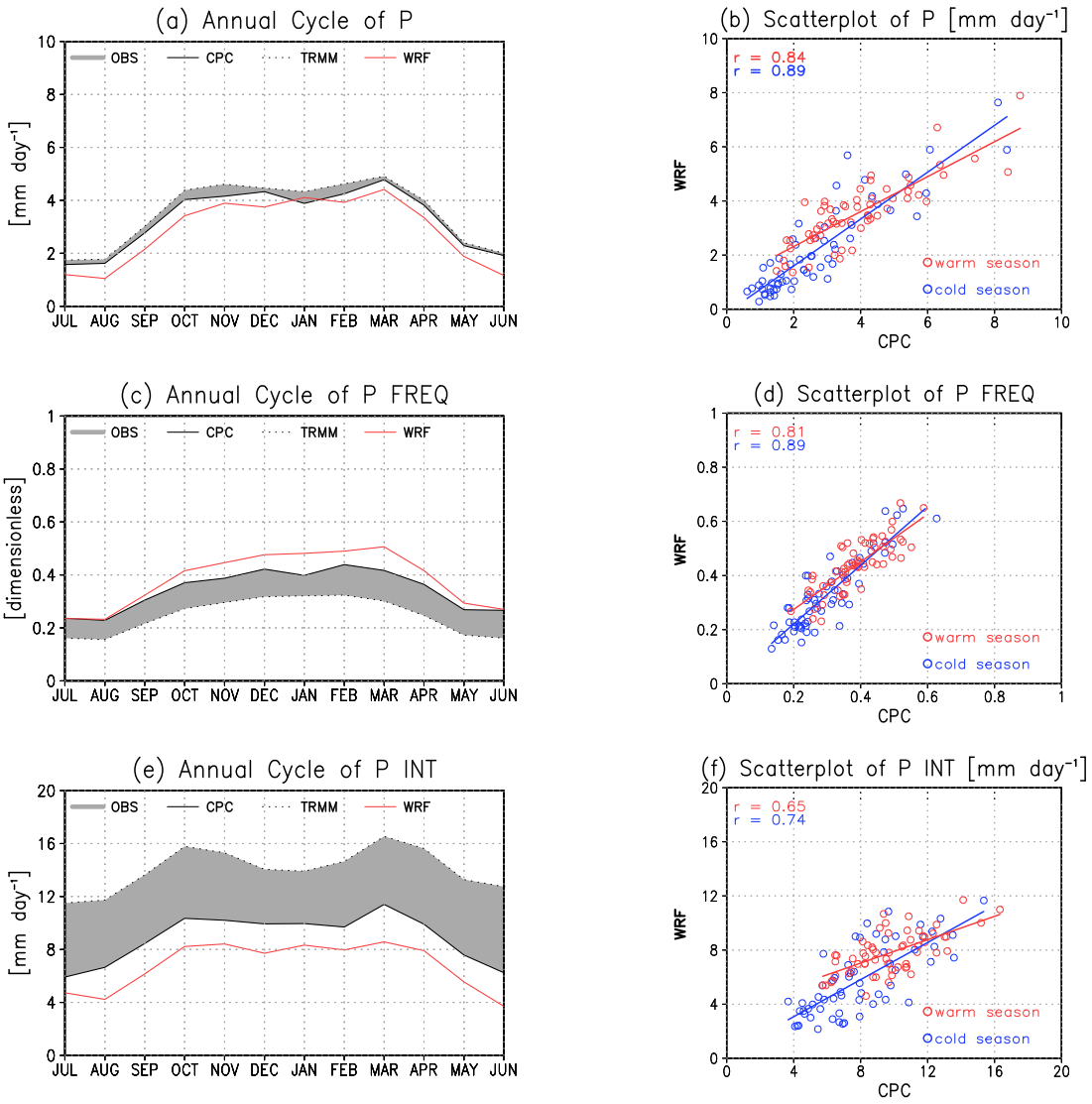

Figure 3.5: Mean annual cycle of Lower LPB (i.e. LOP and URU) for ten years period of (a) precipitation rate, (c) frequency and (e) intensity and their corresponding scatterplots in (b), (d) and (f) respectively.

a precipitation annual cycle with low variability, where the precipitation rate keeps almost constant from October to April and decrease from May to September (Figure 3.5). The model follows the form of the observation band with an almost constant negative bias of about 0.5 $mm\,day^{-1}$ with exception of January, when the model estimation is in the uncertainty band. The negative bias is also evident in Figure 3.5b where most WRF values, either during cold or warm season, are below of the 1:1 line. The correlation coefficients for precipitation rate are of 0.89 for cold seasons and 0.84 for warm seasons, similar values to those obtained on Upper LPB. In terms of precipitation frequency and intensity, WRF shows even more frequent and less intense events than CPC (Figure 3.5d and f) as in Upper LPB.

Note that the correlation coefficient computed on Table 3.3 for each sub-

basin and the full basin and also those computed for cold and warm seasons of Upper and Lower LPB on Figures 3.4 and 3.5 are always between 0.77 and 0.93 suggesting a great capacity of the model to represent the precipitation rate estimated by CPC. Focusing on how the model achieves the precipitation rate (Figures 3.4c-f and 3.5c-f) it is noted that the model represents better the frequency than the intensity of rainy days. In other words, according to CPC observations WRF tends to correctly simulate the precipitation rate, but slightly overestimates the number of rainy days and underestimates the precipitation intensity on those days.

3.3.2 Soil Moisture Estimates

A direct comparison between the observation data set and the model estimation is not possible for several reasons. Soil moisture values are highly dependent on model characteristics, preventing a comparison between models. While the Noah LSM simulates soil moisture at 0.1 m, 0.4 m, 1.0 m and 2.0 m below surface, the moisture content of ESA (satellite derived) is estimated at 0.05 m below surface. Also, Sörensson and Berbery (2014) reported that the season of initialization of a simulation as well as the vegetation type affect the model skill to predict soil moisture. In particular, they suggest that the best results in predicting soil moisture in LPB with WRF/Noah are achieved when the simulation starts on wet season (from September to February). In this work, the simulation effectively begins on wet season (January). However, in order to avoid a direct comparison of different approaches the assessment is done examining spatial patterns, mean annual cycles, scatterplots and the correlation between series.

The maps presented on Figures 3.6a and b show many similarities between satellite-based observations and model estimation of soil moisture. Both distributions have high values to the east with maxima over the Atlantic Forest, a region where precipitation maps (Figure 3.2) showed the highest values. Also, observed and simulated water content have the minimum in the Atacama desert, the area with least precipitation rate of the domain. Focusing on LPB, the Lower LPB shows a general agreement between model and observed soil moisture. In the Upper LPB the model presents somewhat drier conditions than those observed. Major differences are found over the Andes towards northwest domain, where the simulation is wetter than observations. The location is coincident with the maximum (positive) bias of precipitation (see Figure 3.2c), hence the soil moisture bias seems to derive from overestimated precipitation.

The annual cycles of simulated and observed soil moisture for Upper LPB (Figure 3.7a) share the same month of maximum and minimum values (February and August respectively), but the simulation cycle has higher variability than observation cycle. Differences arise mainly from low levels of simulated

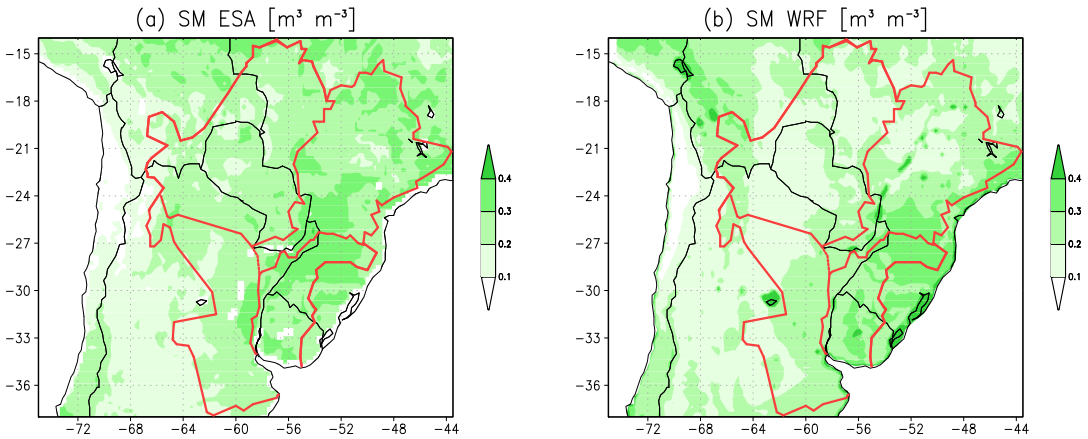

Figure 3.6: Ten years average (a) observed soil moisture 0.05 m depth based on ESA; and (b) simulated soil moisture at 0.1 m depth by WRF.

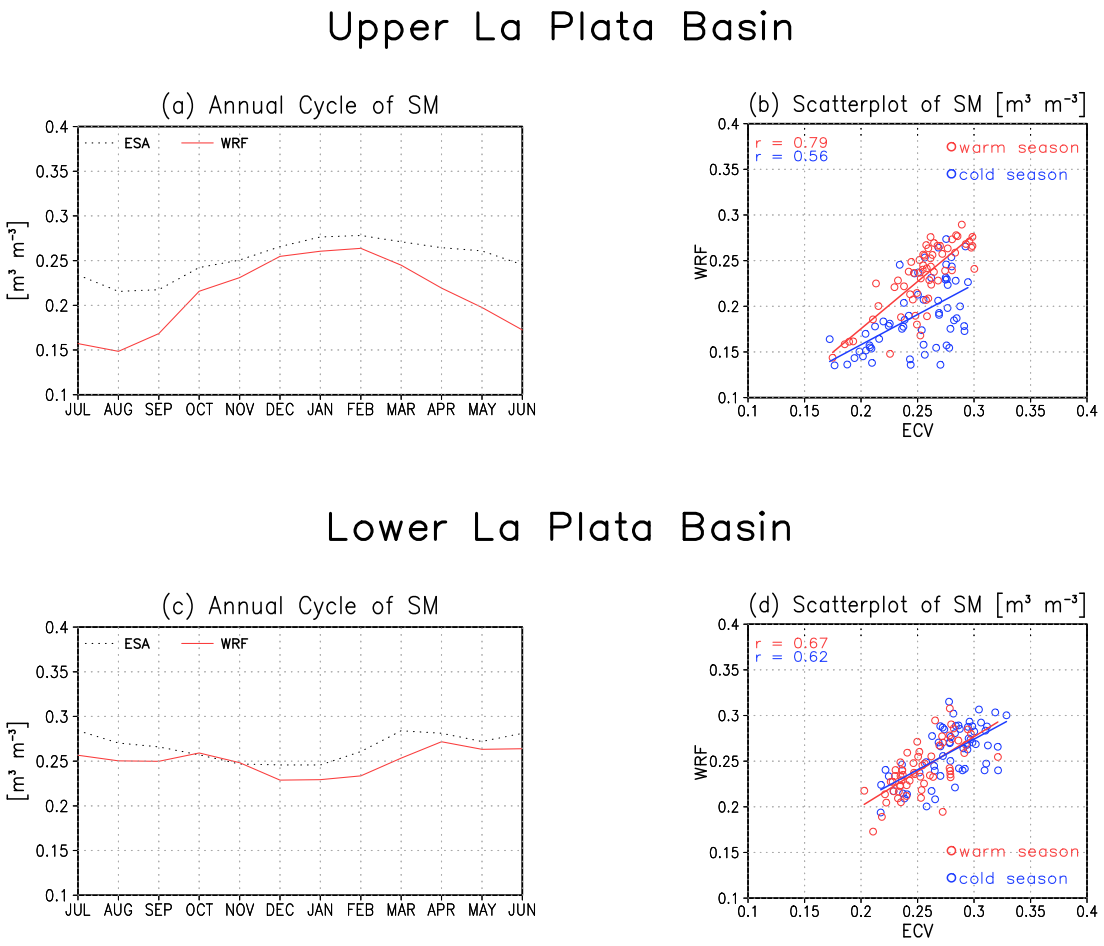

Figure 3.7: Mean annual cycle of soil moisture for (a) Upper LPB and (b) Lower LPB and their corresponding scatterplots in (b), and (d) respectively.

moisture in cold months, season where the model has the the lowest correlation with observations (r = 0.56) (Figure 3.7). On the other hand, the warm season has a good correspondence between both data sets with a correlation of r = 0.79.

For the Lower LPB, both annual cycles show low variability with two local maxima (Figure 3.7c), although not coincident. While the observation curve

has maxima in early autumn and winter, the model shows them in early autumn and spring. The scatterplot presented in Figure 3.7d shows similar correlations for warm and cold seasons ($r = 0.62$ and $r = 0.67$ respectively). Also, the distributions of values for both seasons (red and blue circles) appear merged in the plot and restricted to a narrow range of values, also supporting that soil moisture has low variability during the year.

3.3.3 Temperature Estimates

The spatial distribution of mean temperature as estimated from the CPC observations (Figure 3.8a) shows the Andes as the coldest region, with average values below 5 $^{\circ}C$ in zones of higher elevation. In the rest of the domain, the average temperatures decrease from north to south, as it moves away from Equator. While the area in the subtropical region averages temperatures above 25 $^{\circ}C$, the extra-tropical region averages temperatures around 15-20 $^{\circ}C$.

The model simulation captures the main features of the observed temperature in terms of magnitude and distribution (Figure 3.8b). In most of the domain the biases range between -2 $^{\circ}C$ and $+2$ $^{\circ}C$ (Figure 3.8c). As were detected for precipitation and soil moisture, the greater biases (warm and cold) are present in Chile and over the Andes Cordillera, but the combination of sparse observations and steep slopes over the region prevent a deeper analysis of the model's surface temperature simulations on this area. Away from the Andes, the bias pattern shows somewhat warmer temperatures over the middle of the continent and cooler temperatures on a band along eastern coast. On these areas, model anomalies range between 0.5 $^{\circ}C$ and 2.5 $^{\circ}C$ in magnitude. Particularly WRF shows warm biases over the northwest side of LPB (Paraguay sub-basin), and slight cold biases over the east side of LPB (Mid-Upper Paraná and Uruguay sub-basins). In the Lower Paraná the model has a mix of warm biases toward northwest and slight cold biases towards the south.

The annual cycles of the two observed estimates of near surface temperature over Upper LPB show discrepancies leading to uncertainties on what the actual values may be (see Figure 3.9). While the satellite derived product (MODIS) has the maximum on October, the gridded observation data set (CPC) has the maximum on January, but it presents almost constant values from December to March. A maximum in October may be due to the effects of the monsoon system. The Upper LPB and particularly Mid-Upper Paraná subbasin are affected by the monsoon system. Temperatures raise during spring as expected, but intense summer rains (due to the monsoon) cool the surface and near surface temperatures. Some gauge stations (Teniente Jara in Paraguay, Ipameri, Capinópolis, Franca among others in Brazil) have the hottest month in October, nevertheless CPC, which is based on station data, fails to identify this maxi-

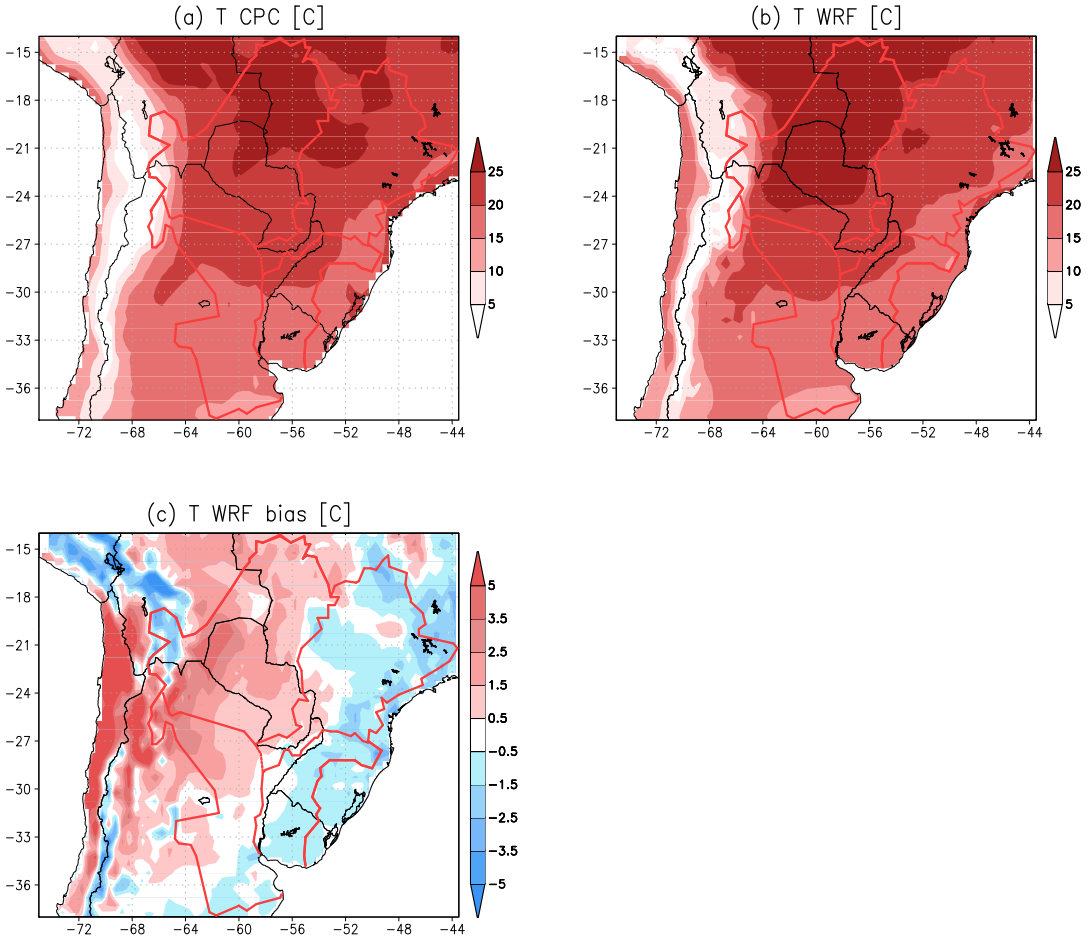

Figure 3.8: Ten years average of (a) observed temperature at 2 m based on CPC; (b) simulated temperature by WRF; and (c) model temperature biases ($WRF - CPC$).

mum. As already stated, this could be due to the low density of gauge stations in this region.

Focusing on model estimation, it tends to follow the MODIS evolution with the maximum in October that slightly decreases in the following months. Beyond the form of model curve, its values are remarkably close to CPC mean temperatures from December to July. In the rest of the year the model has warm biases with respect to the two observational time series. This behavior is replicated in the scatterplot where the distribution remains close to the imaginary 1:1 line for the cold season (blue circles) reaching a correlation of $r = 0.95$, while warm season circles are disperse and above 1:1 line, with a correlation of $r = 0.57$.

The observations for the Lower LPB show a narrow band of uncertainty (Figure 3.9c) and a defined annual cycle with maximum in January and minimum in July as expected in the southern hemisphere. The cycle is correctly reproduced by the model with a slight warm bias on January and February. The scatterplot in Figure 3.9d confirms the good approximation between WRF and CPC with a correlation of $r = 0.98$ for both seasons.

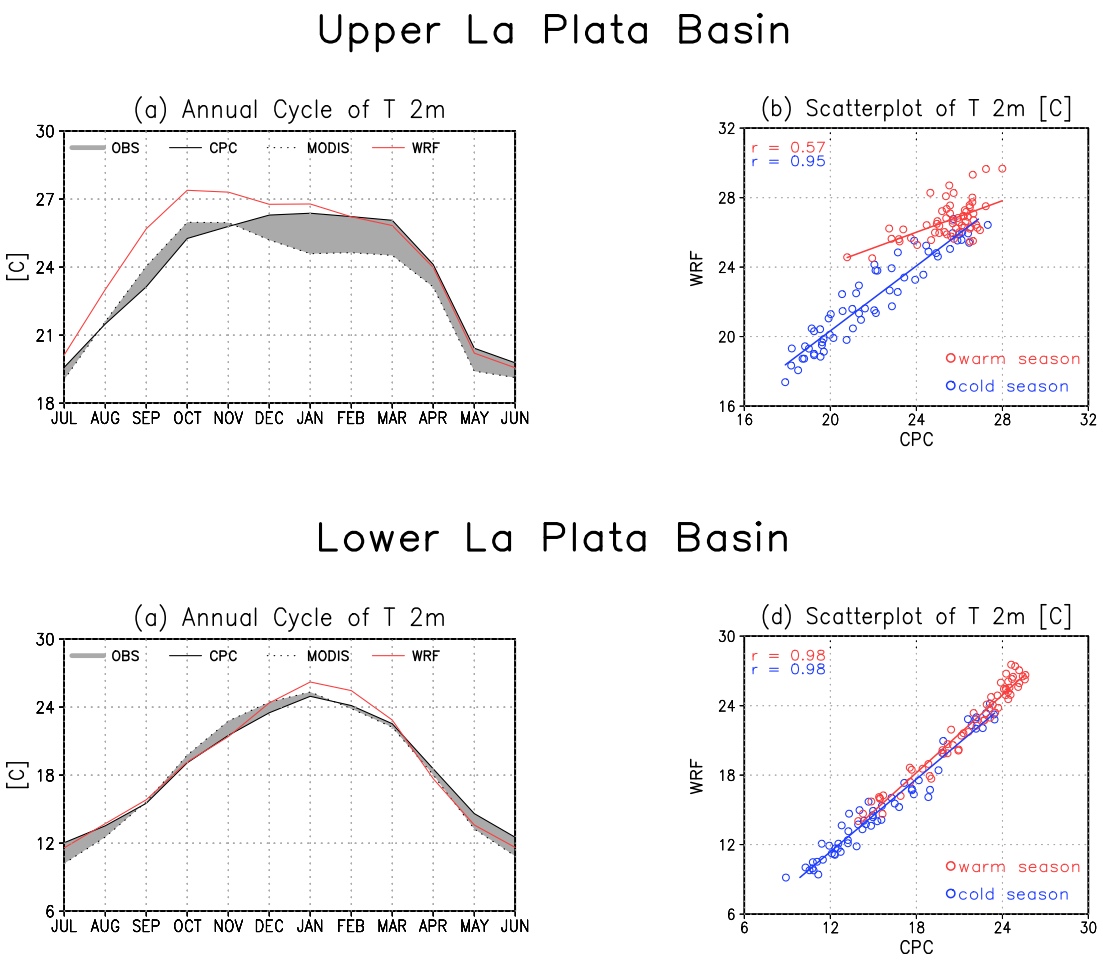

Figure 3.9: Mean annual cycle of temperature at 2m for (a) Upper LPB and (b) Lower LPB and their corresponding scatterplots in (b), and (d) respectively.

3.4 Extreme Events Assessment

The model skill to represent extreme events is evaluated next through analysis *SPI*. *SPI* is based on the probability of precipitation for any time scale, and allows an easy characterization of abnormal wetness and dryness. Positive values indicate greater than median rainfall; negative values indicate less than median rainfall. The severity classes are shown in Table 3.4 following the categorization of McKee et al. (1993). The WMO recommends that all national meteorological and hydrological services should use the *SPI* for monitoring dry spells (World Meteorological Organization, 2009). The advantages of *SPI* over other indexes are that it is based only on monthly precipitation, and its standardization allows comparisons across regions with markedly different climates and easily determines the "rarity" of an event. Also, it can be computed for different time lengths, from 1 to 36 months.

First, the model's ability to simulate abnormal conditions of precipitation is assessed with histograms. Figure 3.10 compares the distribution of *SPI* computed with CPC and model precipitation, for Upper and Lower LPB and for different time-scales: 3–, 6-, 9- and 12-months. To obtain a representative his-

SPI	Probability of occurrence	Class
2.00 or more	2.3	Extremely wet
1.50 to 1.99	4.4	Severely wet
1.00 to 1.49	9.2	Moderately wet
-0.99 to 0.99	68.2	Near normal
-1.49 to -1.00	9.2	Moderately dry
-1.99 to -1.50	4.4	Severely dry
-2.00 or less	2.3	Extremely dry

Table 3.4: SPI classes defined by McKee et al. (1993).

togram for each region (Upper and Lower LPB), the histogram for each grid point belonging to the region is computed. Then all histograms are averaged into one [2]. In other words, each histogram in Figure 3.10 can be considered as the sum of the individual histograms for each grid point of the region divided by the number of grid points. This method of calculation allows to interpret the bin height as the number of months with a specific *SPI* value during the 10 years of the simulation. For instance, the red bin with *SPI*3 values between -1.5 and -2 in Figure 3.10a means that, for the model, there are 5 months during the 10 years period where Upper LPB gets *SPI*3 in that range.

Focusing on abnormal wetness and dryness for Upper LPB, i. e. $|SPI| >= 1$, the histograms (left column in Figure 3.10) show a very good approximation of moderately dry months by the model, but also an underestimation of severely to extremely dry months. This behavior is similar for all time-scales. On the other hand, the probability of occurrence of wet months, either moderate, severe or extreme, is very well represented by WRF for all time-scales. For the Lower LPB, there is almost not difference between CPC and WRF for severely to extremely dry months, but there are more observed months with indices indicating moderate drought, with exception of *SPI*3 where the values are equivalent. The bins for moderately, severely and extremely dry present slightly lower values for the model in comparison with CPC in all time-scales.

In summary, histograms of SPI based on model or observed precipitation have similar shape in all time-scales. The main differences are found in severely to extremely dry months, where the model does not show as many cases as were found in observations. Nevertheless, the probability of occurrence of moderately to extremely wet months is notably similar between CPC and WRF. The model histograms indicate that it is capable to reproduce extreme conditions,

[2] An areal average of *SPI* values over a region should be avoided, as this variable has positive and negative values around zero. Then, the average result is not representative of *SPI* of the region.

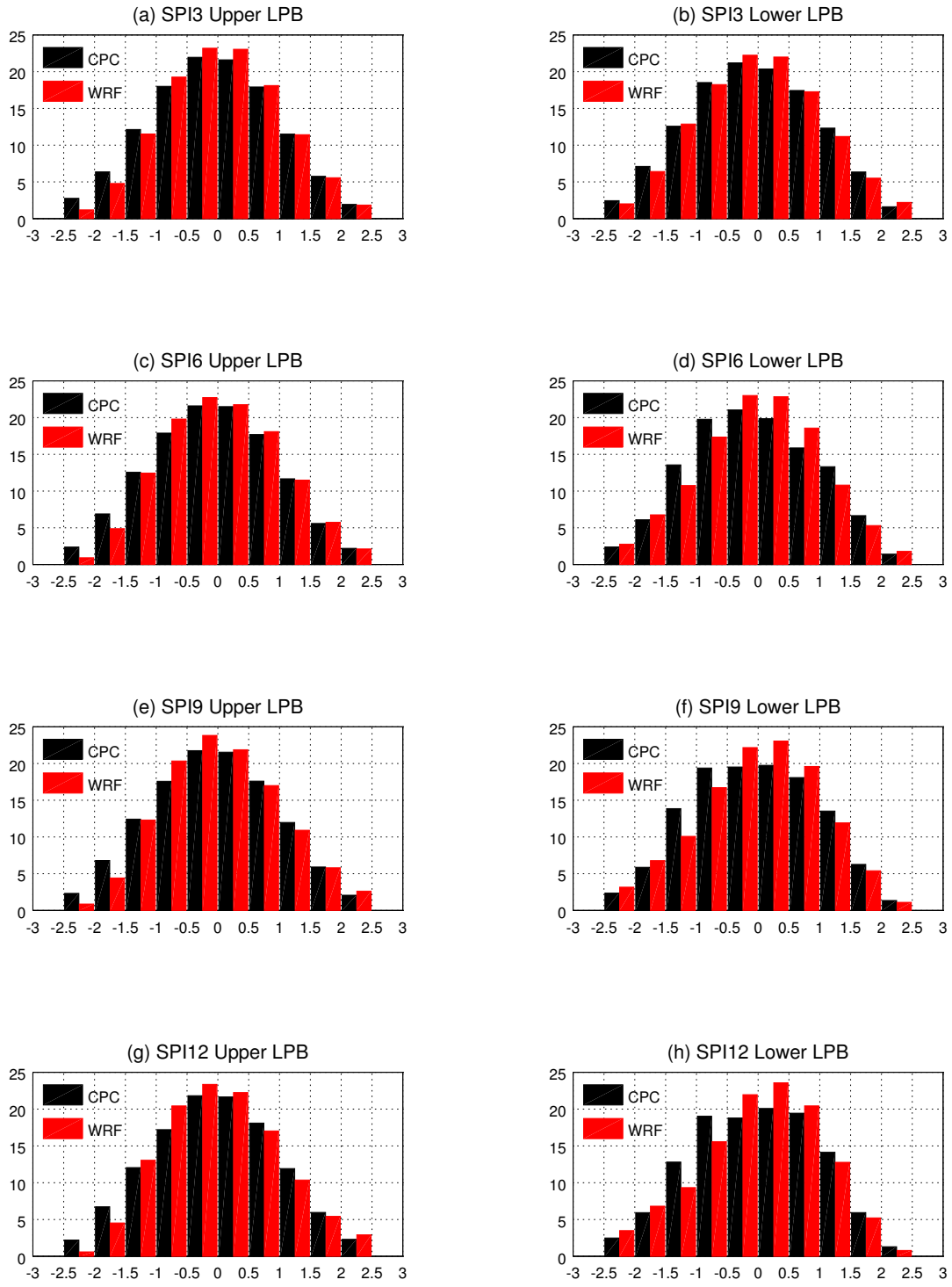

Figure 3.10: Histogram of *SPI*3, *SPI*6, *SPI*9 and *SPI*12 for Upper LPB (left column), and for Lower LPB (right column).

with some difficulties in severe to extreme droughts.

The *SPI* histograms presented above give an idea of how good is the model to reproduce the frequency of occurrence of extreme events, either droughts or wet spells. In other words they respond to the question: Is the model capable to reproduce extreme events in a long term simulation with the frequency and intensity that they occur in the region?. However, the histograms do not show

the correspondence between simulated and observed events, or in general, between simulated and observed SPI.

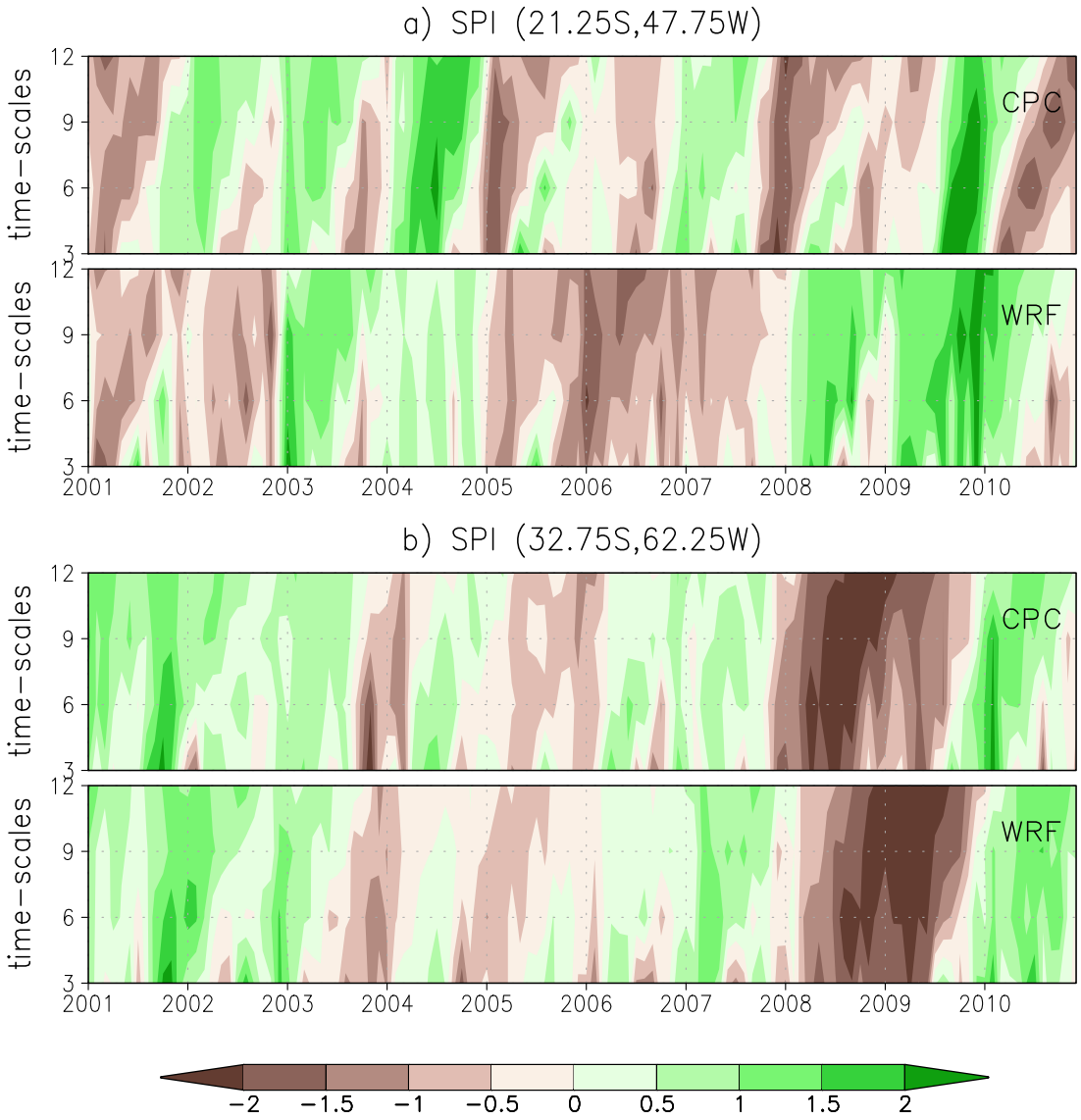

Figure 3.11: Time-series of SPI based on CPC and WRF presented as functions of time-scales (3, 6, 9 and 12 months) for two locations: a) (21.25S,47.75W), and b) (32.75S,62.25W).

In order to compare *SPI* from CPC and WRF, the 10-year evolution of *SPI* for both sets are presented in Figure 3.11. The time-series are shown for particular grid points and as function of time-scales. The locations are selected following some criteria. First, the availability of reliable stations around, in order to assume that CPC precipitation correctly represents the observed on that point. Then that SPI based on CPC is assumed realistic. Second, the occurrence of drought or wet spells during the ten years period. Finally, the selected points should be placed on different sub-basins with different climate conditions. The chosen locations are (21.25S,47.75W) and (32.75S,62.25W). The first location is placed in the state of Sao Paulo in southern Brazil. This point belongs in the

Mid-Upper Paraná sub-basin. The second location is placed in the province of Córdoba in central Argentina and belongs in the Lower Paraná sub-basin.

The evolution of *SPI* based on CPC precipitation (Figure3.11a) shows a high inter-annual variability with some extreme events (classified as severely or extremely dry/wet) such as the droughts at the beginning of 2005, at the end of 2007, during 2010 and the wet spell at the end of 2009. The time-series of *SPI* based on WRF precipitation shows lower inter-annual variability and less months with severe or extreme anomalies. The observed severe droughts of 2007 and 2009 and 2010 are simulated as mild or moderate droughts by the model. This is consistent with the previous analysis of Upper LBP histograms, where severely to extremely dry months are less frequent for WRF than CPC. The observed wet event classified as severe has a better approximation by the model that also classified it as severe but during a shorter period than observed. Also the WRF time-series present more difficulties with a severe drought in 2006 that was not observed, and many months where the model has negative anomalies while CPC show them as positive anomalies and vice-versa.

The results improve for the grid point placed in Lower Paraná (Figure 3.11b). Here, WRF *SPI* follows the evolution of CPC *SPI* in terms of anomaly sign (dry or wet) but also in intensity. Both graphics begin with wet anomalies until mid-2003. In next years both set of series share the evolution alternating mildly to moderately dry and wet months up to the end of 2007. An extreme drought during 2008 and 2009 and a wet 2010 complete the series. Focusing on severe to extreme events, WRF identifies the drought of 2008 and 2009 (it will be a case study in the next chapter) but showing a longer period of extremely dry months. Also, it is remarkable how the model captures the short extremely wet month towards the end of 2001. Beyond some small differences that were highlighted the model achieves a very good estimation of dry and wet anomalies on this location.

3.5 Discussion: Model Strengths and Weaknesses on LPB

The overall results presented on this chapter suggest that the proposed model parameterization is suitable to represent the regional climate. The largest biases of the analyzed variables are observed over the Andes Cordillera, where there are not enough gauge stations for a correct assessment. Models often fail due to: a) a lack of adequate resolution to represent the topographic changes, b) the parameterization does not adjust to the processes inherent to mountain-dominated areas, such as snowfall or snowmelt. Beyond this troublesome area, the investigation will focus on the model ability over LPB, which is mostly plain.

Within LPB, the model simulation achieves a high resemblance with the spatial pattern of precipitation based on CPC and correctly identify the large annual variation of precipitation to the north. However, the model tends to simulate drier conditions than observed mainly during dry/cold seasons, but also on wet/warm seasons on Lower LPB. Correlation coefficients between WRF and CPC were computed for LPB, their subbasins as well as for dry/cold and wet/warm seasons. All correlations are above 0.77 indicating a remarkable ability of the model to represent the precipitation rate. Yet in terms of frequency and intensity, both observations and model shows diversity; the model has more frequent and less intense rainy days than observations.

The soil moisture patterns based on satellite (ESA) and model estimations are consistent with the spatial precipitation distribution, with the highest values over the Upper Paraná Atlantic Forest and driest conditions in the Atacama Desert, being the Andes in Bolivia and Perú the places with largest wet biases. LPB shows a general agreement between model and observed estimations, with slightly drier biases in Upper LPB. The correlations between both data sets are better for wet/warm season than for dry/cold seasons. A deeper analysis of soil moisture is not possible as it is highly dependent of its source.

As with precipitation and soil moisture, the model does a very good approximation of the spatial distribution of temperatures, except over the Andes. The simulated temperatures have a very high correlation for the Lower LPB in all seasons, while the Upper LPB has high correlation in dry/cold season, but it decreases in warm months due to the warm biases in Paraguay sub-basin. The model also shows slightly colder temperatures over the east side of LPB (Mid-Upper Paraná and Uruguay subbasins). In Lower Paraná the model has warm biases towards the northwest turning into slight cold biases towards the south.

Extreme events ($|SPI| \geq 1$) showed similarities between the probability distributions of *SPI* Upper and Lower LPB. Some difficulties are found in severe to extreme droughts over Upper LPB, where the model does not show as many events as were observed. The probability of occurrence of moderately to extremely wet months is notably similar between CPC and WRF. The evolution of *SPI* based on CPC and WRF precipitation was evaluated in two places, one in each part of LPB, i.e. Lower and Upper LPB. The WRF results in the northern location does not have a good correspondence to CPC. The model simulates lower inter-annual variability and less intense events. The results show a dramatic improvement in the southern location, where the model achieve a very good correspondence for all *SPI* time-scales, identifying correctly dry or wet anomalies with different intensities. For instance, the severe drought of 2008 and 2009 that will be studied in next chapter is identified from the beginning in late 2007 until its end in late 2009. There are also similarities in intensities but the model shows a drier event than observed.

The long-term simulation discussed on this chapter has demonstrated a very good performance of the model in this region. The assessment suggests that the simulation can be used as a reliable model climatology for remaining experiments, as it represents the regional climate. At the same time, it is a good starting point from which is expected to improve. The objective is to reduce current biases from a more realistic representation of land covers.

Chapter 4 | Land Surface Processes: The LPB Drought of 2008

4.1 The Observed LPB Drought of 2008

The hypothesis of this research is that a realistic representation of the land cover properties helps improve the simulation of the land surface-atmosphere interactions and hence can reduce model biases that are inherent to surface processes. Consequently, it is expected that the effects will be more noticeable during anomalous situations, when the vegetation conditions depart noticeably from their predefined properties, as during a drought period. For this reason the hypothesis is tested for a drought event that took place in southern South America in 2008. Other neighboring regions had normal or excess of precipitation giving the opportunity to examine the land-atmosphere interactions and surface effects during very different conditions.

4.1.1 Observations

The observational data sets used to describe the characteristics of the 2008 drought and to evaluate the model performance are those that were used to evaluate the 10-year simulation in the previous chapter (see Section 3.2.2). Additionally, the NDVI is used to identify EFTs capturing the seasonal and inter-annual variability of vegetation primary production. The NDVI data set was derived from the MODIS vegetation product MOD13C2 for 2001-2009. This data set consists of 16-day maximum value composite global images at a spatial resolution of $0.05^\circ \times 0.05^\circ$.

4.1.2 Observed Features of the Drought

The large-scale ocean patterns during the severe drought of 2008 affecting southern South America were consistent with the modes described in Section 1.1, that is, the combination of a La Niña episode with large tropical North Atlantic warm SST anomalies, as shown in Figure 4.1. The drought had exceptional characteristics in terms of spatial extension and persistence, causing

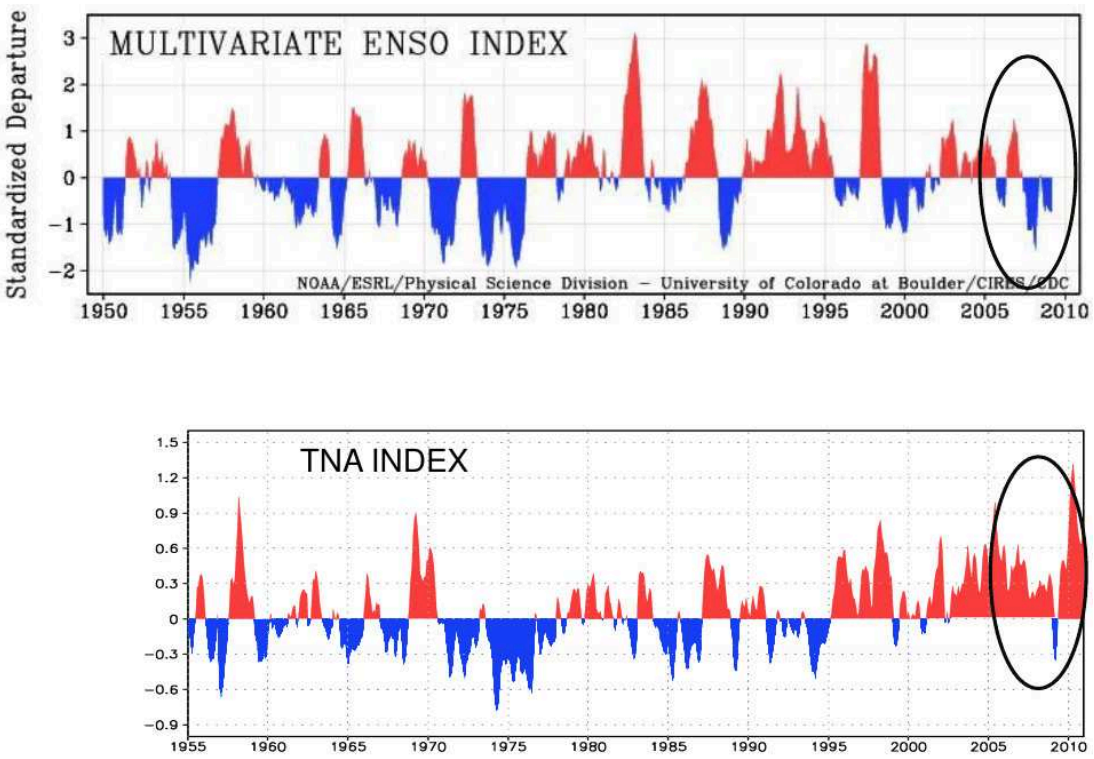

Figure 4.1: Evolution of Multivariate ENSO Index at top from http://www.esrl.noaa.gov/psd/enso/mei, and Tropical North Atlantic Index at bottom created with data from http://ioc-goos-oopc.org/state_of_the_ocean/sur/atl/tna.php. The black ellipse focus on drought period.

great economic losses. Bidegain (2009) reported that the spatial extent of the 2008 drought was comparable to, or larger than, other important droughts in the region that occurred during the last five decades. In several locations the duration of the drought was the longest on record, achieving very low values of *SPI*, which in some cases became the series absolute minimum (Skansi et al., 2009).

The spatial distribution of the drought as represented by the precipitation anomalies is shown in Figures 4.2a and 4.2b. Both maps shows a negative center over Uruguay, extending over the Lower Paraná and Middle Paraná, and southern Paraguay sub-basins with a maximum deficit of 2 $mm\ day^{-1}$ over Uruguay (a reduction to about 40 % of the 1998-2007 mean). Particularly, the CPC map has drier anomalies around the Mid-Paraná that extends to the Upper Paraná. Figure 4.2c depicts the 3-month *SPI* average during 2008. The *SPI* values identify the main drought area as moderately to severely dry. The rainfall deficit conditions have an evident effect on the soil moisture availability in Lower Paraná and Uruguay, mainly in areas covered by croplands and grasslands (Figure 4.2d). The depletion of rainfall and soil moisture have effects over the vegetation health/stress, which exhibits also negative anomalies of NDVI (Figure 4.2e) over the same croplands and grasslands areas.

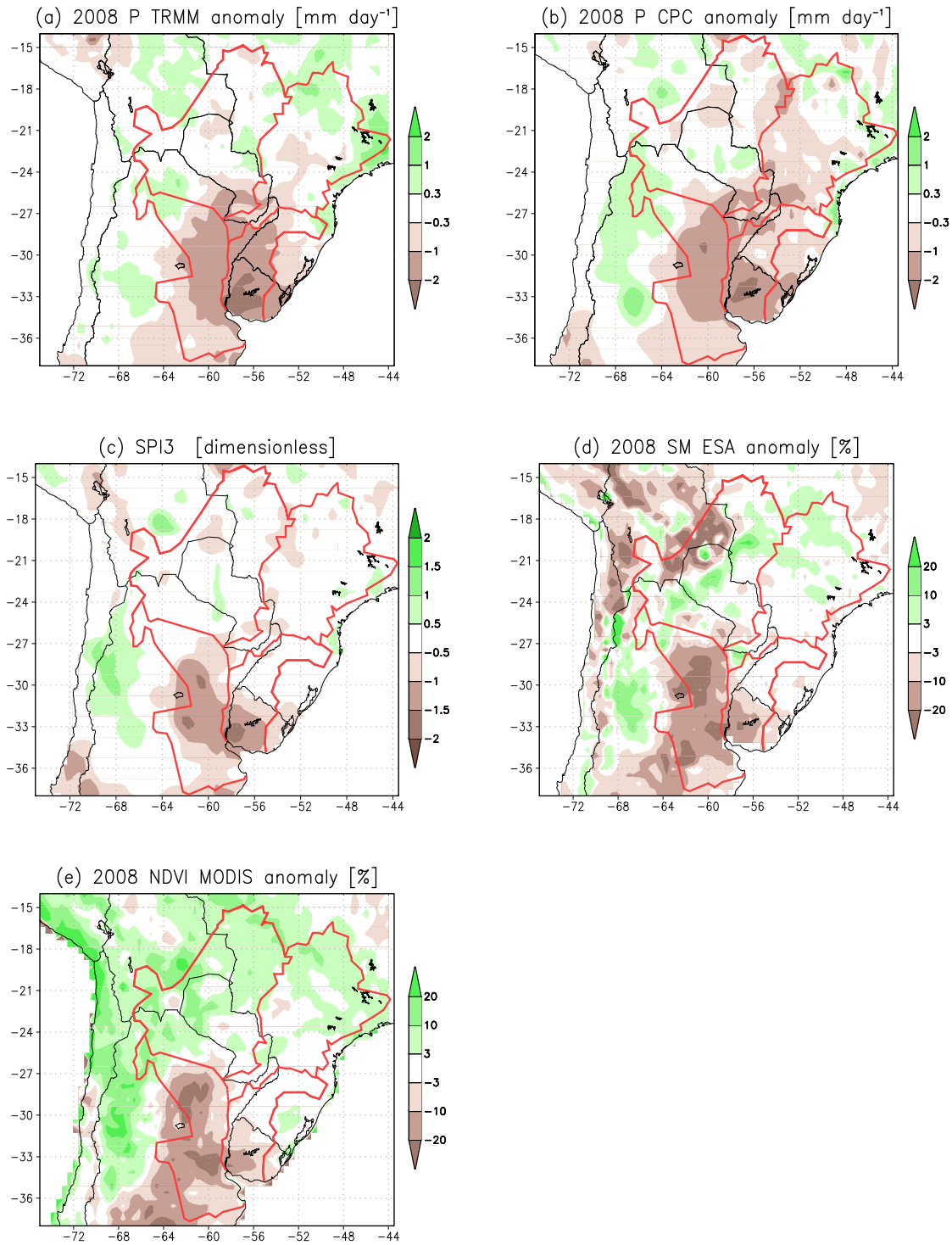

Figure 4.2: The year 2008 anomalies for (a) TRMM precipitation, (b) CPC precipitation, (d) CPC soil moisture, (e) MODIS NDVI. All anomalies are computed as the difference between 2008 values and average values in the period 1998-2007. Panel (c) shows the average *SPI*3 during 2008 based on CPC precipitation.

Figure 4.3 presents the evolution of the drought through areal averages over the Lower LPB, the most affected part of the basin. Figures 4.3a and b indicate that the region had first a rainfall deficit during the austral winter of 2007 that recovered during the austral spring, only to return to an almost continuous

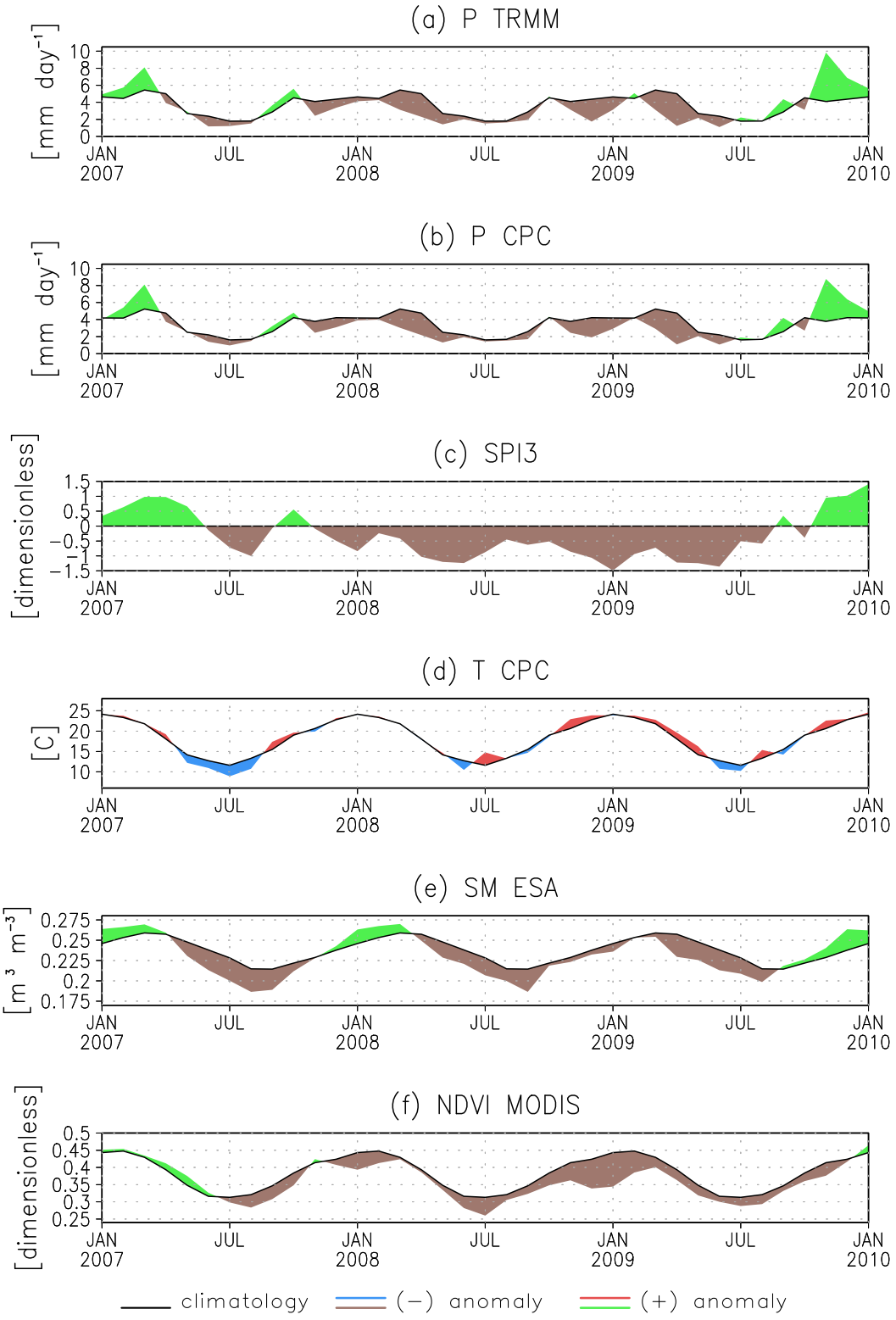

Figure 4.3: Area-averaged time series for the drought region (Lower LPB) of: (a) TRMM precipitation anomalies, (b) CPC precipitation anomalies, (c) 3-month *SPI*, (d) CPC temperature anomalies, (e) ESA soil moisture anomalies, and (f) MODIS NDVI anomalies. All anomalies are done with respect to the corresponding mean annual cycle based on the period 1998-2007.

deficit from November 2007 to June 2009. The time series of *SPI*3 in Figure 4.3c repeats the precipitation evolution, showing four local minima classifiable

as moderately dry ($SPI3$ <=-1.0). The minimum in August 2007 derives from the first rainfall deficit, and the remaining minima appear lagging one month with respect to the minimum peaks of rainfall, as a consequence of the computation method for $SPI3$. The near surface temperature in Figure 4.3d shows a slight warming of about 0.5 °C on average from the mean annual cycle during the longest period of the drought. The soil moisture also follows the rainfall evolution (Figure 4.3e), with a first deficit in the winter of 2007, and then a continuously deficit from April 2008 that begins to recover in September 2009, with the rain returning to normal around July/August 2009. The water deficit had a direct effect on NDVI that presents a long period of low vegetation greenness (Figure 4.3f) starting about three months after the first negative anomalies of precipitation. The time-series show that the long-term anomalous precipitation strongly affected vegetation and soil conditions, which need about two months of normal to high precipitation to recover back to their typical mean values.

In summary, the spatial distribution and time evolution of the analyzed variables suggest that the precipitation deficit affected soil conditions mainly in areas dominated by croplands and grasslands. Then, these land covers reflect these conditions with low NDVI, indicating stressed vegetation. As was explained in previous chapter this information is not considered by models. On this research, the vegetation states will be included through the EFTs.

4.1.3 Ecosystem Functioning During the 2008 Drought

Figure 4.4a presents the 2001-2009 median EFT field that is a characterization of ecosystem functioning. Blue/green colors represent ecosystems with large net primary production, low seasonality and warm season maxima (for example, the subtropical forests, Dd1). Red/yellow colors represent the opposite behavior, as in the Dry Puna (Ad3). See the legend in Figure 4.4a for the definition of all ecosystem functional types/colors. In general, ecosystems of temperate South America show maxima in autumn and summer. EFTs that have a summer maximum tend to show medium-to-low productivity and high seasonality. EFTs with a winter NDVI maximum tend to exhibit either very low or very high productivity under very low seasonality values.

Figure 4.4b shows the 2008 EFT map. In most of the domain, both maps (Figs. 4.4a and 4.4b) share the same categories. However, as expected from previous subsection, remarkable differences are evident for areas that experienced either strong land use changes or climate-related vegetation stress. Particularly, the map of 2008 EFTs shows large changes in the main drought area (white rectangle): areas with green colors were reduced, while red colors were expanded. It means that patches with average productivity and seasonality in

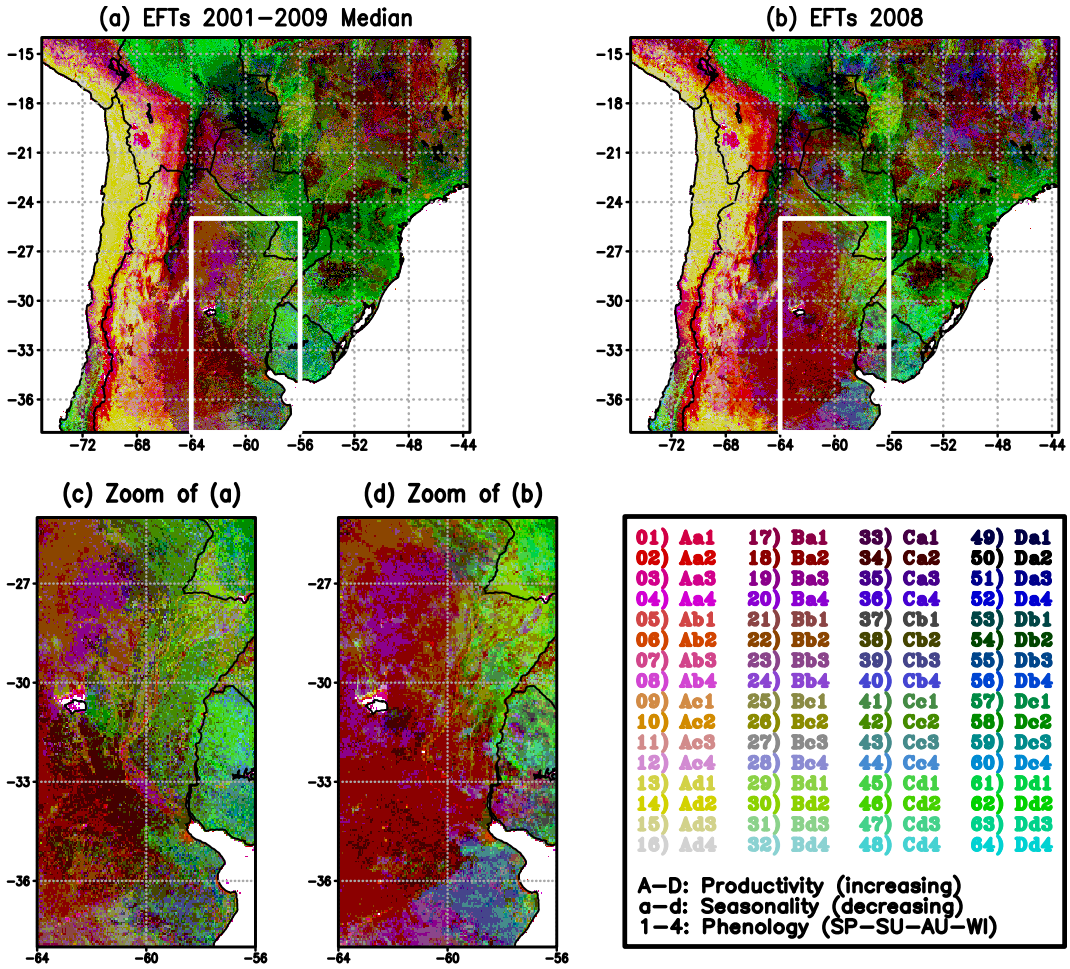

Figure 4.4: (a) 2001-2009 EFTs median map and (b) EFTs map for 2008, and the zoom over the white rectangle in (c) and (d) respectively. EFTs categories are indicated by the legend at bottom right.

Figure 4.4c are replaced by low and very low productivity and seasonality during 2008, indicating a reduction in photosynthetic activity. Such interannual changes agree with the observed dynamics in NDVI depicted in Figure 4.2d. Also during 2008, the EFT composition of northern Paraguay and eastern Bolivia (part of the Dry Chaco) indicates decreases in seasonality, while in the Atlantic Forest it indicates slight increases of cultivated areas (dark spots).

4.2 Simulation of the 2008 Drought

4.2.1 Model configuration

Numerical simulations of the 2008 drought were carried out with the WRF model version 3.2. The WRF model was run with a horizontal grid spacing of 18 *km* and 28 vertical levels over a domain that covers the southern part of South America (see nested domain in Figure 3.1). The model physics and

dynamics configuration follows the selection of schemes and options described on Table 3.1.

The model was forced by the initial and 6-hr lateral boundary conditions from the NCEP/NCAR Global Reanalysis Project (Kalnay et al., 1996). Sea surface temperatures were obtained from the Reynolds data set, also included in the global reanalysis. The reanalysis additionally provides soil moisture data. It is a variable that need a particular attention, as its initial state is an important source of error in the simulations. First, the NCEP/NCAR reanalysis model has a land surface model that is different from the one used in WRF/Noah. Soil moisture estimates are model dependent, and thus the range of values between wilting point and the field capacity can be very different. Second, the reanalysis land surface model has two layers while Noah uses four layers, hence an interpolation is needed (the interpolation scheme is part of the WRF package). In long term simulations like the ones performed in this study the spin-up time should be enough to achieve an equilibrium that minimizes these errors.

Control simulations (CTL) were carried out using the USGS land cover map (see Figure 2.2a) and its corresponding biophysical properties (see Table A.1). Experiments using the IGBP land cover categories obtained from MODIS data (see Figure 2.2b) were also carried out but they are not shown, as the model performance was similar to that using the USGS definitions. An ensemble of five members was created using identical parameterizations with the only difference being the initial conditions that are 24-hr apart following the lagged average forecasting method (Hoffman and Kalnay, 1983). The simulation of the ensemble members starts on five consecutive days, from August 29 to September 2, 2007. All simulations end on July 31, 2009. This period covers the whole period of precipitation deficit, as shown in Figures 4.3a and b. Hereafter we will call this period “drought period”.

Then, similar simulations were performed using the land cover representation based on EFTs map (see Figure 4.4b) and their biophysical properties forming an ensemble called EFT. The results were compared with the CTL ensemble to study the sensitivity of the model to the lower boundary conditions derived from land cover. The model configuration for the EFT ensemble simulations was identical to that of the CTL ensemble, except for the change in the land cover data set.

4.2.2 Changes in the Biophysical Properties

Previous to study the simulation results (outputs), it is interesting to analyze the differences in the model inputs. As was explained before the ensembles of this experiment share identical configuration, and just modify the land cover representation. Then, the comparison between these approaches will help to

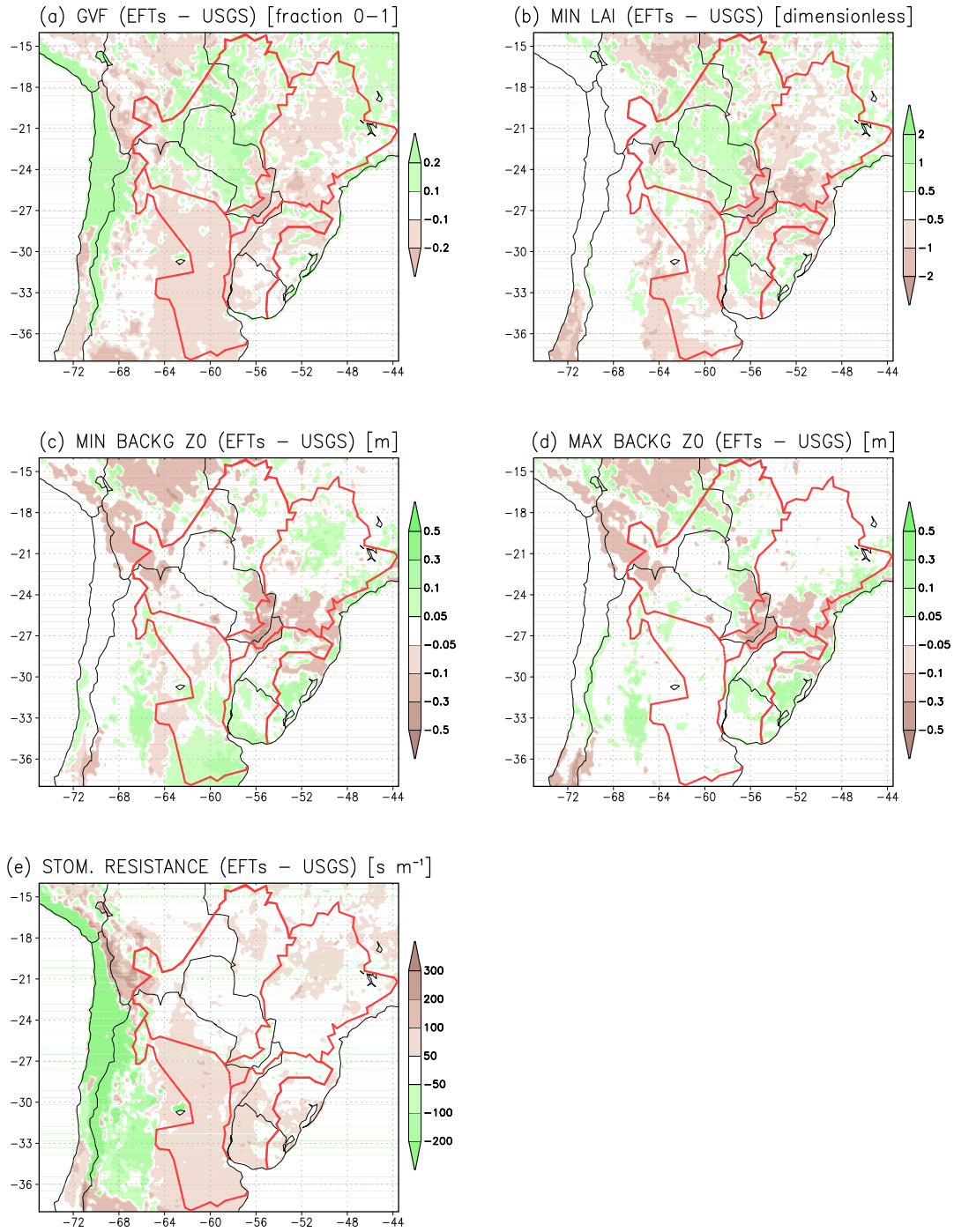

Figure 4.5: Vegetation properties differences between EFTs of 2008 and the USGS classification: (a) green vegetation fraction, (b) minimum leaf area index through the year, (c) minimum and (d) maximum background roughness length through the year, and (e) stomatal resistance.

understand the differences of the ensemble results.

A comparison between the distribution of EFT categories and conventional land cover types is not possible as they come from different approaches. However, the comparison can be done directly over the properties derived from each approach. Figures 4.5 and 4.6 present the biophysical property changes when the USGS land cover map is replaced by the EFTs map of 2008. Eight out of

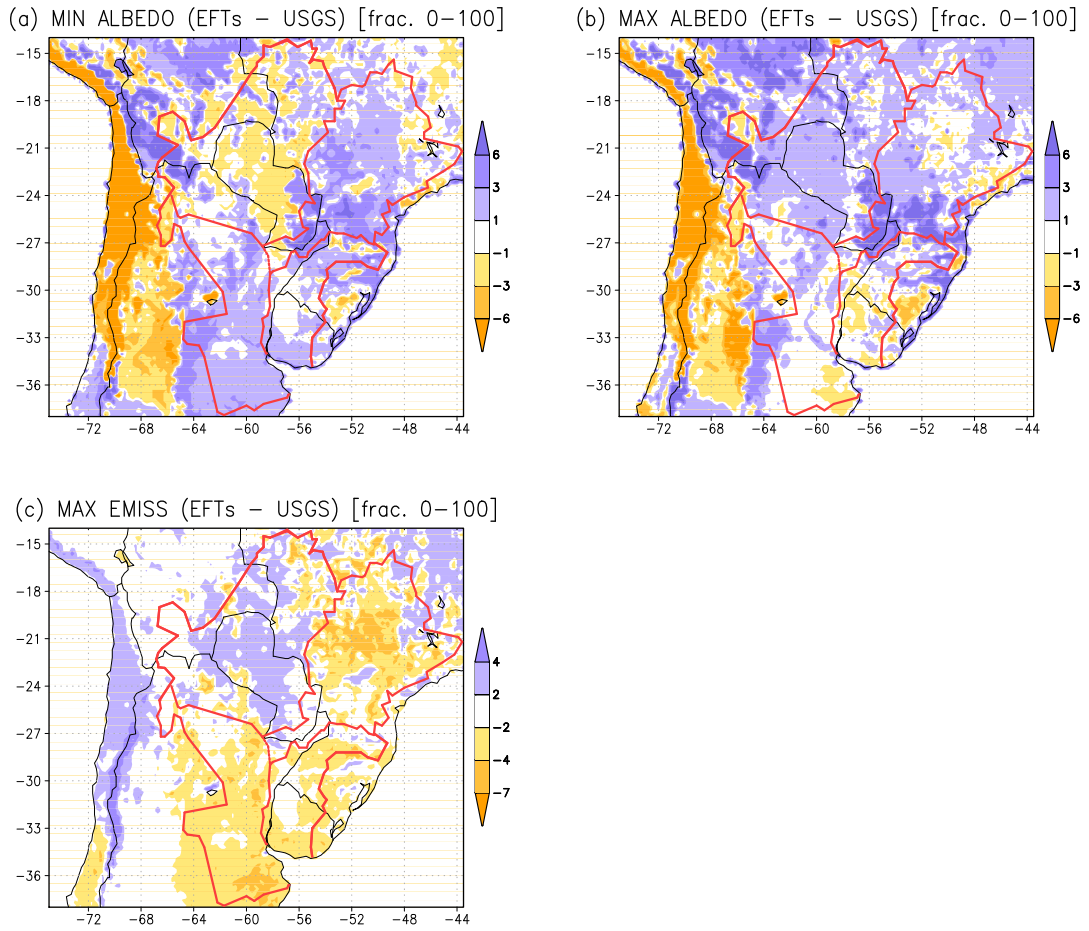

Figure 4.6: Vegetation properties differences between EFTs of 2008 and the USGS classification: (a) minimum and (b) maximum background albedo through the year and (c) maximum background emissivity through the year.

the fifteen parameters are shown. They were selected because of their larger dependence on the land surface changes as described by the time-varying EFTs (Alcaraz-Segura et al., 2011, 2013a). Figure 4.5 presents the properties related to vegetation, like greenness fraction, leaf area index, surface roughness and stomatal resistance[1]. On the other hand, Figure 4.6 shows properties related to the radiation terms, like albedo and emissivity. Some maps of minimum or maximum parameters are not shown as their present almost the same values for USGS and EFTs, for instance, maximum leaf area index.

Biophysical properties associated with the 2008 EFTs depict the drought region with decreased greenness and leaf area index, and larger stomatal resistance (Figure 4.5). Also the region presents an increase in minimum albedo and a reduction of emissivity (Figure 4.6). Focusing on the secondary core of the drought (around Mid Paraná), EFTs reduce greenness fraction, leaf area index and surface roughness. This region has higher values of minimum and

[1]Note in Figure 4.5e that, unlike the rest of panels, colors were reversed to reflect that for all properties, green colors represent greener vegetation, and brown colors, drier.

maximum albedo.

In general, the changes in biophysical properties from USGS to EFTs are consistent with the dry conditions of the year under study. However, while the use of EFTs improves the description of land cover states in most of the domain, there are exceptions. The Atacama Desert in northern Chile appears "greener" because the methodology tends to smooth such extreme states. In future versions, the EFTs computation will be improved by setting a decision rule to classify nonvegetated pixels (water bodies, snow, and absolute deserts) before the calculation of the NDVI descriptors (Alcaraz-Segura et al., 2013a).

4.2.3 Effects of Land Surface Changes on Regional Climate

An analysis is done of the changes in precipitation and 2-m temperature when EFTs are used as lower boundary conditions. The interpretation of these changes focuses on the modification of vegetation properties, and concurrent land surface processes. Nevertheless, a specific interpretation for the precipitation and 2-m temperature changes is not always apparent due to the complexity of the system, including the type of land cover (or EFT) that prevails in each region, and the dominant precipitation/circulation regimes to which each region is subject. Further, while the Noah LSM follows a single column approach, its use over a grid and coupled with WRF implies that nonlinear three dimensional effects will take place. Land cover changes will favor the generation of surface gradients for different variables, which in turn will induce local circulations and differential surface heat fluxes. Advective processes will be influenced, as will be the moisture flux convergence (e.g., Baidya Roy and Avissar, 2002; Lee and Berbery, 2012).

Precipitation

The spatial distribution of precipitation during the drought (Figure 4.7a) depicts a similar pattern to that described in Subsection 3.3.1. The main differences are the reduced maximum around Mid Paraná and shifted isohyets eastward in Lower LPB evidencing the drought.

The CTL bias map (Figure 4.7b) fails to faithfully represent the local drought features. It shows a dry bias of about 1 $mm\ day^{-1}$, i.e., exaggerating the drought severity in Lower LPB, and wet biases towards the northern part of the drought region (NE Argentina/E Paraguay). Positive biases are found in an approximate longitudinal band along 25°S - 18°S, with values of up to 8 $mm\ day^{-1}$ near the Andes Cordillera and the Brazilian Highlands, and up to 5 $mm\ day^{-1}$ in Paraguay. Underestimated precipitation in Lower LPB agree with the evaluation of the model climatology. However, the positive biases in Upper LPB are unexpected,

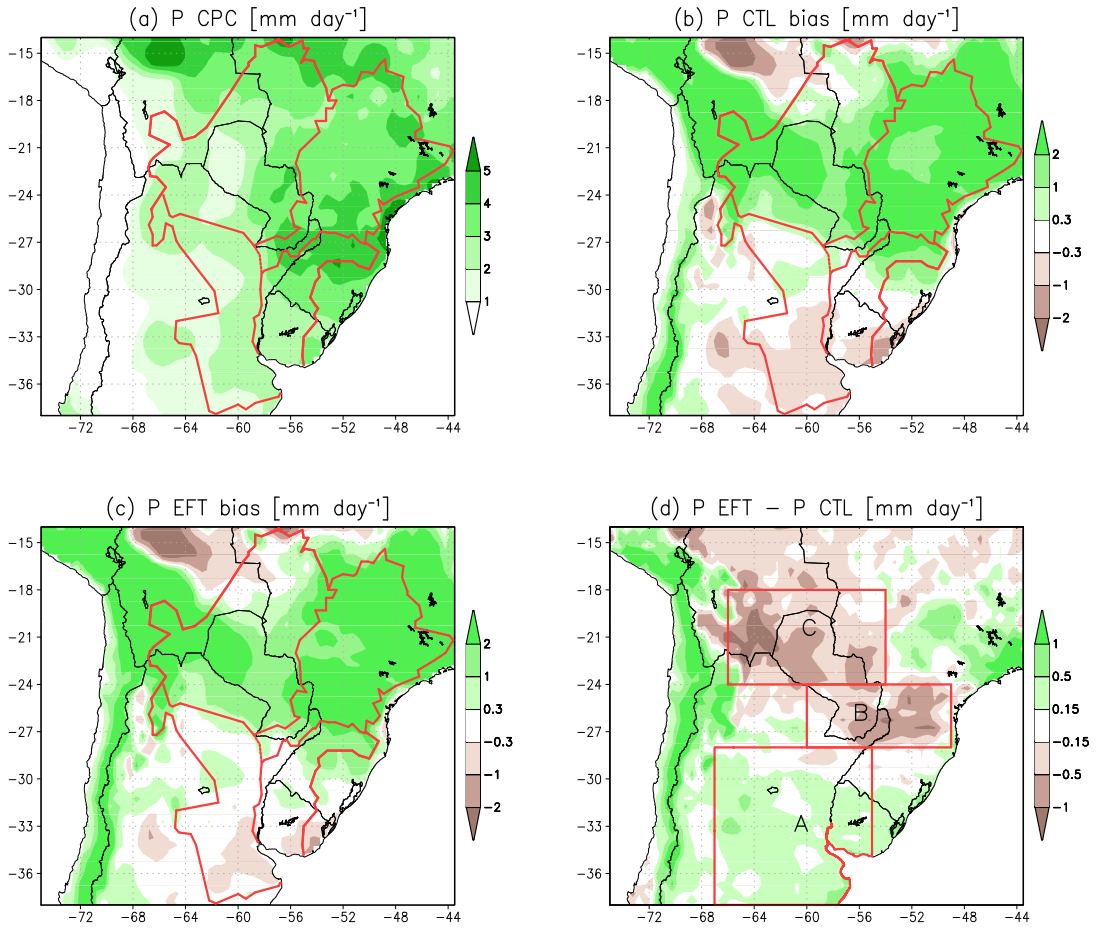

Figure 4.7: (a) Observed mean precipitation during the drought period, (b) CTL and (c) EFT ensemble biases, and (d) their differences. Panel (d) identifies three areas that are selected for further analysis: A (bottom) represents the drought region, B (middle) represents the northernmost part of the drought area, and C (top) is the region with large positive biases of precipitation.

as the model tends to have drier conditions than observed according to the climatology. Then, the biases can be derived from the changes of the lateral boundary conditions used in each case.

The rainfall bias of the EFT ensemble (Figure 4.7c) resembles that of the CTL ensemble both in terms of pattern and magnitude. Nevertheless, the difference map (Figure 4.7d) shows that the EFT ensemble reduces the biases in several regions. To the south of the domain, positive values (green shades) mean that the EFT ensemble produced slightly more rain in an area where the CTL had a dry bias. Over Bolivia, Paraguay and south of Brazil, Figure 4.7d presents negative values (brown shades), meaning that the EFT ensemble reduces the wet bias of the CTL ensemble. Thus the EFTs bring the model representation of the precipitation pattern closer to the observations in regions with either wet or dry biases.

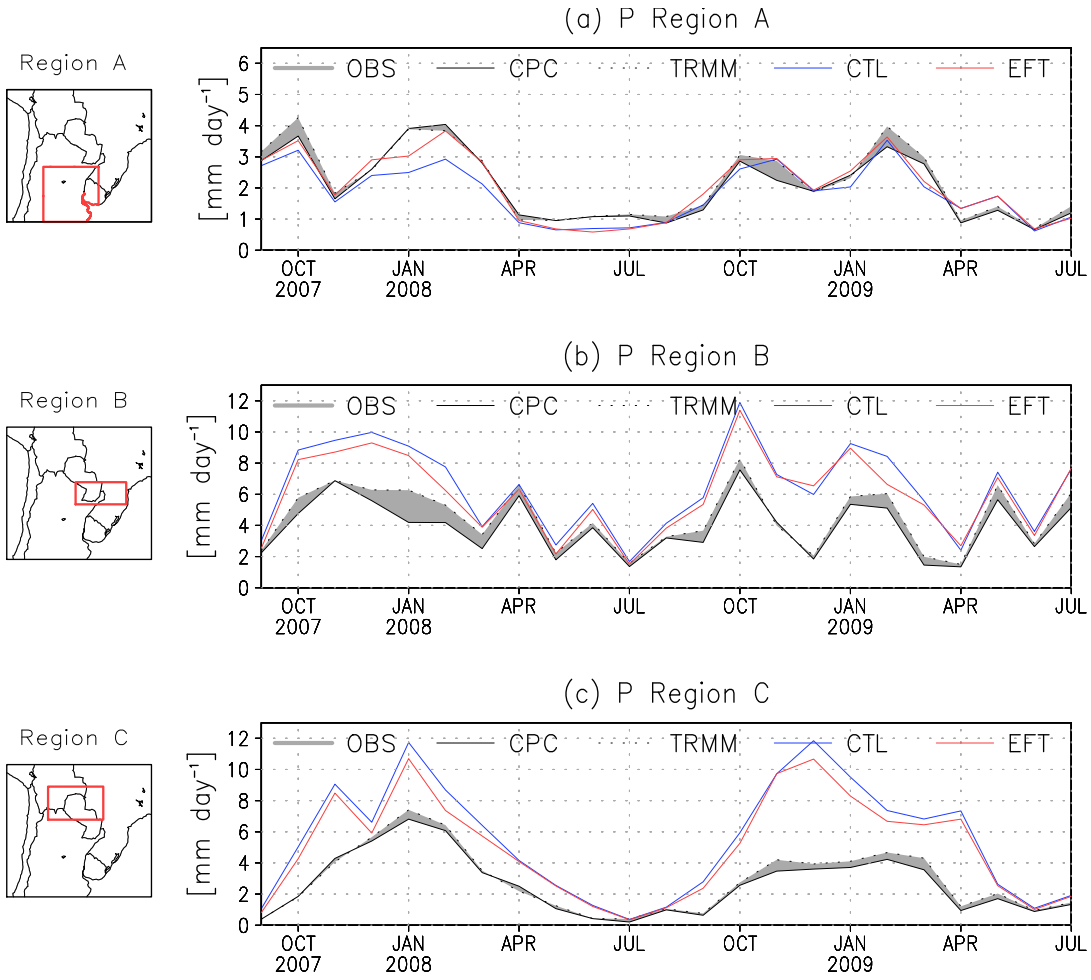

Figure 4.8: Area-averaged precipitation for TRMM and OBS (their differences are shaded), CTL and EFT ensembles over (a) region A, (b) region B, and (c) region C.

Region	Drought Period	Warm/Wet Season
A	3.4%	3.9%
B	8.9%	10.8%
C	19.9%	27.4%

Table 4.1: Bias reduction in precipitation (%) from the CTL ensemble to the EFT ensemble for the three regions defined in Fig. 4.7c.

Three regions were selected to examine the time evolution of area-averaged model, satellite, and observed precipitation estimates (Figure 4.8). The shading between the satellite and observed precipitation is an indicator of the uncertainty in the observations. Bias reductions are presented in Table 4.1.

Region A covers the drought core region where the CTL ensemble simulations exaggerate its severity (Figure 4.7b). The EFT ensemble simulation increases the magnitude of the precipitation (Figure 4.8a), reducing the dry bias by about 4 % during the rainy seasons (Table 4.1), and offering a somewhat better representation of the drought event.

Prop.	Region A			Region B			Region C		
	USGS	EFTs	DIFF	USGS	EFTs	DIFF	USGS	EFTs	DIFF
GVF	0.7	0.6	-12.3	0.8	0.7	-5.2	0.6	0.7	9.7
SR	94.6	128.0	35.4	103.2	115.9	12.3	90.7	122.9	35.5
LAI_{mn}	1.2	1.0	-21.8	2.0	1.5	-22.7	1.0	1.2	20.0
LAI_{mx}	4.0	3.5	-13.2	5.0	4.4	-11.1	4.0	4.0	0.0
$Z0_{mn}$	0.09	0.12	33.3	0.31	0.21	-32.3	0.19	0.16	-15.8
$Z0_{mx}$	0.14	0.16	14.3	0.31	0.24	-22.6	0.19	0.19	0.0
α_{mn}	0.18	0.19	5.6	0.16	0.18	12.5	0.19	0.19	0.0
α_{mx}	0.22	0.22	0.0	0.17	0.20	17.6	0.20	0.22	10.0
ϵ_{mn}	0.93	0.93	0.0	0.94	0.93	-1.1	0.93	0.93	0.0
ϵ_{mx}	0.97	0.95	-2.1	0.95	0.95	0.0	0.94	0.95	1.1

Table 4.2: Area-averaged values of vegetation properties for the three selected regions (A, B and C) derived from the USGS and EFTs data sets. Their percent differences (%) are computed as $[(EFTs - USGS)/USGS] \times 100$. See properties notation and units in Appendix A.

Region B corresponds to the northern sector of the observed drought, where the model had failed to replicate the dry conditions. The EFT ensemble precipitation (Figure 4.8b) remains at all times closer to the observations than the CTL ensemble indicating again an improvement on the simulation. Here, the wet bias was reduced by 9 % for the whole period, and by 11 % during wet seasons. Notably, despite differences in magnitude and the absence of a well-established annual cycle, the model simulations reproduce the month-to-month variability.

Lastly, Region C covers northern Paraguay/southern Bolivia where the CTL ensemble exhibits a large wet bias. The observed rainfall (Figure 4.8c) has a defined annual cycle with a maximum during summer and a minimum during winter. The evolution is correctly represented in the two ensemble simulations, but with excessive magnitude during summer, sometimes more than doubling the observed values (e.g., December 2008). However, the EFT ensemble simulation reduces the wet bias by 20 % for the whole period and 27 % for the rainy seasons (Table 4.1).

Table 4.2 shows 10 out of the 15 biophysical properties for the three regions.[2] The vegetation in EFT ensemble for Region A seems to be more representative of the drought period than the CTL ensemble, as it exhibits a lower

[2]The five terms excluded either did not give perceptible information for the region (e.g., related to snow processes or radiation stress) or were mostly constant (e.g., rooting depth).

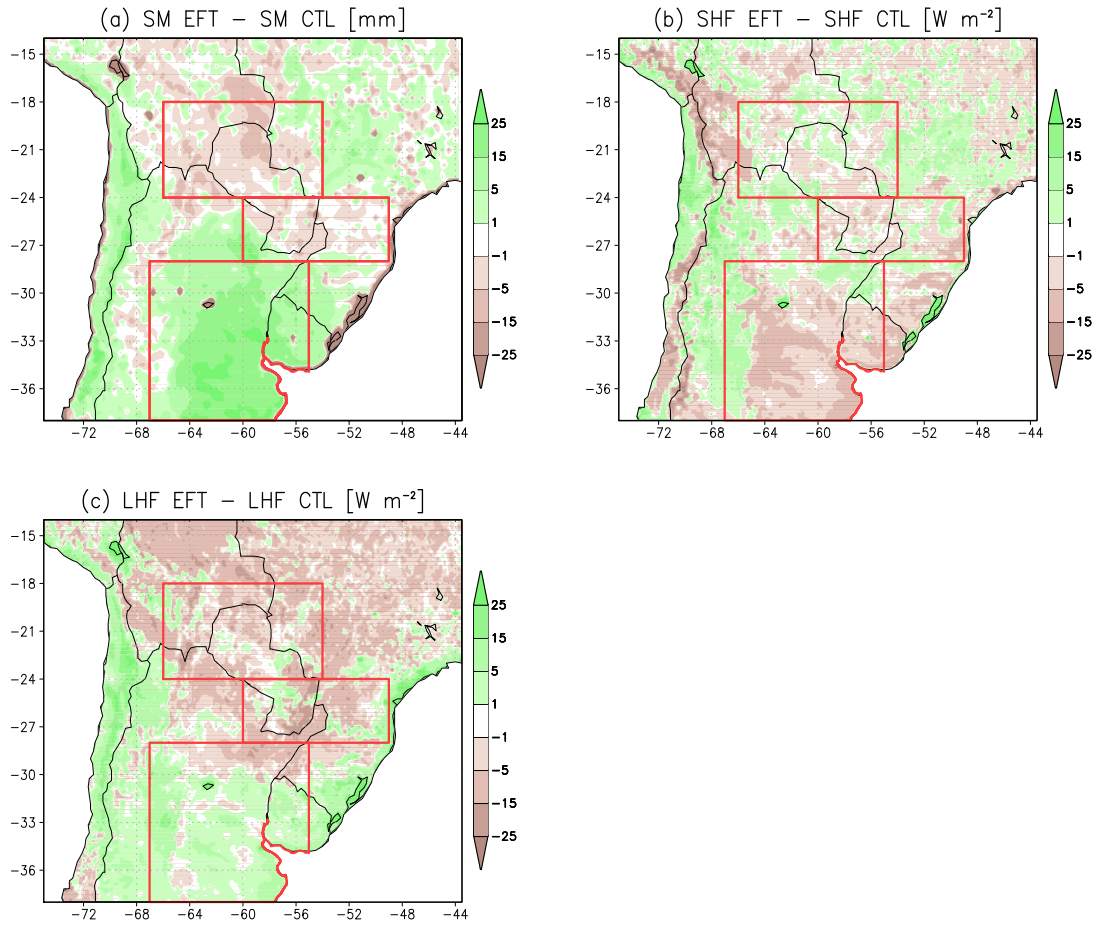

Figure 4.9: Mean values during the drought period of (a) soil moisture for the two top 2 layers (40 cm depth); (b) sensible heat flux; and (c) latent heat flux.

vegetation greenness fraction and leaf area index, as well as higher stomatal resistance (Table 4.2). On the other hand, the EFT ensemble has a precipitation increase over Region A that cancels out the dry bias noted in the CTL ensemble. The increased precipitation leads to soil moisture increases, favoring a larger latent heat flux and a sensible heat flux reduction (Figure 4.9).

While the two findings (bias reduction and more realistic vegetation representation) are encouraging when considered independently, together they seem counter-intuitive. A plausible justification can be found in Lee and Berbery (2012) who examined the effects of land cover changes in the La Plata Basin, where Region A is located. Their results indicate that land cover changes also induce changes in lower level moisture fluxes and their convergence. In the case of the current study, land cover changes from the CTL to the EFT ensembles induce an increase of about 25 % of the vertically integrated moisture flux convergence (not shown) that helps explain the increase of precipitation as a larger scale effect of land cover changes as opposed to a local effect alone.

The reduction of precipitation to the north of the domain (brown shades over Regions B and C in Figure 4.7d) is associated in general terms with a reduction of all components of the surface water balance: soil moisture, evapo-

Var.	Region A			Region B			Region C		
	CTL	EFT	DIFF	CTL	EFT	DIFF	CTL	EFT	DIFF
P	1.9	2.1	10.8	6.4	6.0	-6.4	5.5	5.0	-8.8
SM	86.4	97.7	13.1	136.8	136.9	0.1	113.6	11.8	-1.5
EVT	1.6	1.7	5.1	3.3	3.2	-4.2	2.9	2.7	-5.2
R	0.19	0.24	26.3	2.76	2.48	-10.1	2.14	1.82	-15.0

Table 4.3: Area averages (regions A-C) of selected variables from the CTL and EFT ensembles and their differences computed as $[(EFT - CTL)/CTL] \times 100$. The variables are: precipitation ($mm\ day^{-1}$), soil moisture (mm), evapotranspiration ($mm\ day^{-1}$), and runoff ($mm\ day^{-1}$).

transpiration, runoff and precipitation (see Table 4.3). According to Table 4.2, the EFTs properties in Region B are more representative of drier conditions than those obtained from USGS, with a reduction of the green vegetation fraction and the leaf area index, and increasing stomatal resistance. The large negative difference in surface roughness is likely attributable to the replacement of subtropical humid forests by crops in recent decades (Izquierdo et al., 2008). These conditions increase the surface resistance to evaporate giving place to a positive feedback with weaker turbulent exchanges, lower precipitation, soil wetness and runoff (Figure 4.9 and Table 4.3).

Note that the mean values of soil moisture in the CTL and EFT ensembles are similar (Table 4.3). Analysis of the spatial patterns (Figure 4.9a) indicates that this is attributable to the large positive differences of soil moisture around the southwestern sector of Region B. However, over most of the area where the precipitation bias reduction was achieved, the use of EFTs leads to a general reduction of soil moisture.

The reduction of evapotranspiration in Region C (Table 4.3; Figure 4.9c) can be traced to the increased stomatal resistance and the smaller roughness length (Table 4.2), which is consistent with a reduction of the turbulence in the boundary layer and an increase of the lower atmosphere stability. Also, the decrease in the total heat flux (Figures 4.9b and c) reduces the moist static energy at the boundary layer (Eltahir, 1998) and favors lower rainfall as shown in Fig. 4.7d. As a result of these changes, precipitation, soil moisture and runoff are also reduced (Table 4.3).

In summary, the results show that areas where soil moisture is reduced are associated with evapotranspiration reductions, sensible heat flux increases, as well as lower precipitation and runoff. Conversely, regions where the soil moisture has increased are associated with sensible heat flux reductions and latent heat flux increases that favor a moister boundary layer and increased rainfall

Correlated Variables	Region A	Region B	Region C
SM; LH	0.83	0.62	0.84
SM; SH	-0.67	-0.78	-0.91
LH; P	0.67	0.06	0.71
SH; P	-0.24	-0.60	-0.74

Table 4.4: Correlation coefficients between ensemble changes ($EFT - CTL$) of soil moisture, heat fluxes and precipitation.

and runoff. Correlations among soil moisture, heat fluxes and precipitation presented in Table 4.4 support these general conclusions. Soil moisture is positively (negatively) correlated with latent heat flux (sensible heat flux). In turn, the correlation between latent heat (sensible heat) and precipitation is also positive (negative). These results agree in general terms with the theory of Eltahir (1998) who proposes a pathway for relating the positive feedback between soil moisture conditions and rainfall. As discussed, deviations from this behavior are found when regional circulations develop also as a result of land cover changes.

Temperature

The model temperature was assessed against the gridded data set of observations. Figure 4.10 presents the spatial distribution during the drought as estimated from the CPC observations, the anomaly temperature for CTL and EFT ensemble and their differences. Away from the Andes, the model bias pattern shows somewhat warmer temperatures over the middle of the continent (Western LPB) and cooler temperatures on a band along Eastern LPB (Figure 4.10b). It is consistent with what was observed in the climatology (Figure 3.8c). Inside the LPB, the anomalies range between 0.5 °C and 2 °C in magnitude. The 2-m temperature bias of the EFT ensemble depicts a reduced area with cold bias towards the east coast, but a larger area with positive values (warm bias) over the central continental region east of the Andes (Figure 4.10c). Figure 4.10d presents the differences between the CTL and EFT biases, showing a general increase of temperature.

To further the analysis of the biases, two key regions, identified as Central and Eastern in Figure 4.11, were examined. Table 4.5 presents the values of the biophysical properties for USGS and EFTs, and their differences, while Table 4.6 shows the values of surface variables related to the energy balance from the corresponding ensembles (CTL and EFT).

The general warming over much of the domain can be attributed to the re-

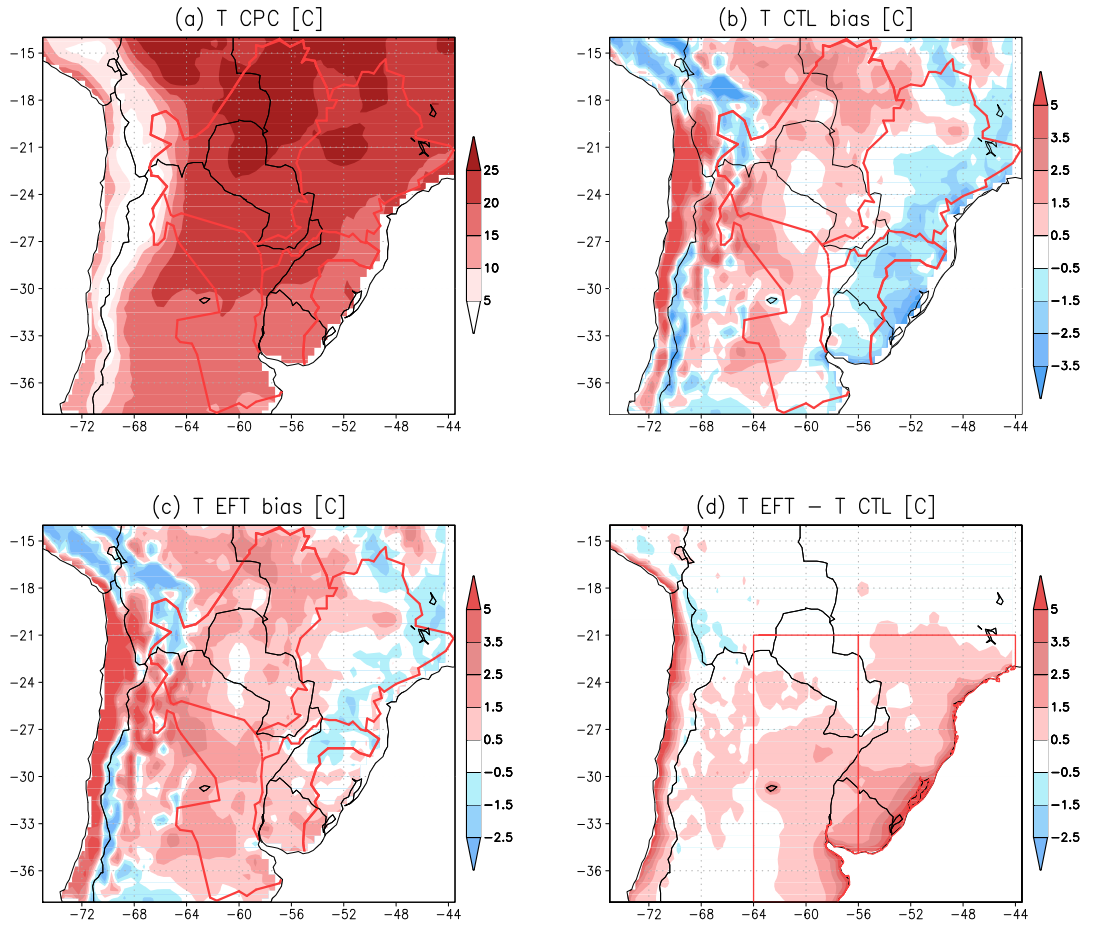

Figure 4.10: (a) Observed mean temperature at 2 m during the drought period, (b) CTL and (c) EFT ensemble bias, and (d) differences between the EFT and CTL ensembles. Panel (d) identifies two areas that are selected for further analysis: Central (left) and Eastern (right).

duction of vegetation, as indicated in the changes of green vegetation fraction and leaf area index for the EFT ensemble (see Table 4.5 and Figures 4.6a,b). This argument is consistent with other studies investigating the relations between vegetation and surface temperature (see, e.g., Kaufmann et al., 2003; Seneviratne et al., 2010; Avila et al., 2012). The changes in vegetation can be attributed to the drought conditions, although the replacement in recent years of natural forest by sowing and crops to the north of the region (Izquierdo et al., 2008), and which are not represented in the CTL land cover, may have contributed as well.

Despite the consistent result for vegetation changes and temperature changes, the analysis of the energy balance (Table 4.6) is uncertain. Most of the changes in the energy budget terms are small and do not appear to have physical consistency. Obviously, the 2-m temperature does not match uniquely the energy balance (surface temperature does), however, at this stage and without analysis beyond the scope of our study, it is unclear whether those inconsistencies are due to differences of behavior between the 2-m temperature and the sur-

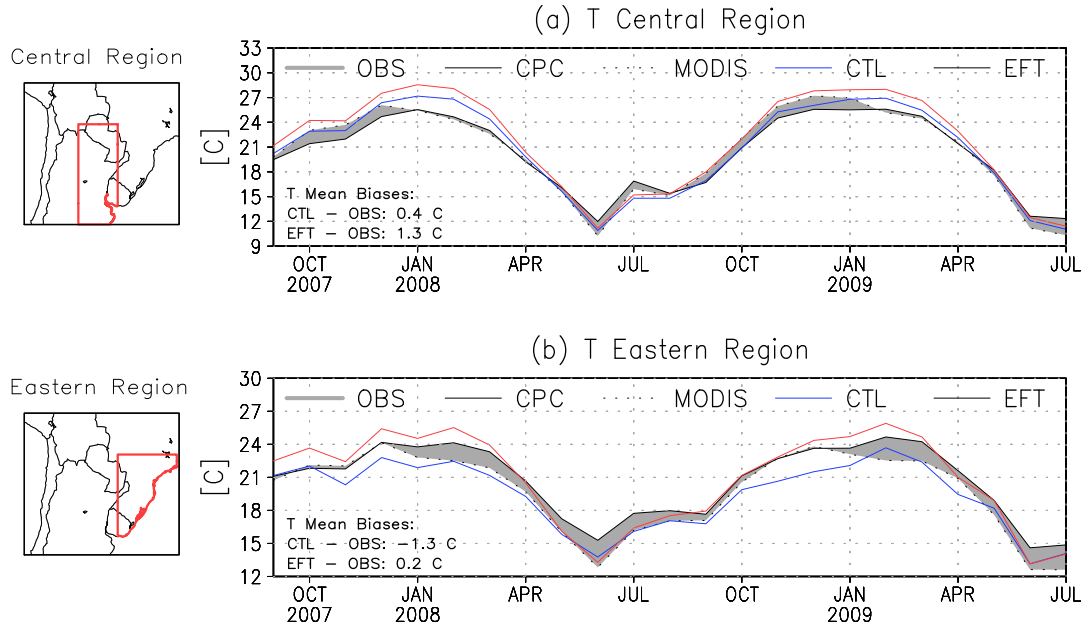

Figure 4.11: Area-averaged 2 m temperature for CPC and MODIS (their differences are shaded), CTL and EFT over (a) central region, and (b) eastern region.

Prop.	Central Region			Eastern Region		
	USGS	EFTs	DIFF	USGS	EFTs	DIFF
GVF	0.70	0.67	-4.3	0.37	0.35	-5.4
SR	62.0	117.0	88.7	93.0	106.8	14.9
LAI_{mn}	1.2	1.1	-6.8	0.9	0.7	-17.8
LAI_{mx}	4.1	3.8	-7.3	2.2	2.1	-1.8
$Z0_{mn}$	0.13	0.14	7.7	0.12	0.10	-16.7
$Z0_{mx}$	0.16	0.18	12.5	0.12	0.12	0.0
α_{mn}	0.18	0.19	5.6	0.12	0.13	8.3
α_{mx}	0.21	0.22	4.7	0.13	0.14	7.7
ϵ_{mn}	0.92	0.93	1.1	0.96	0.96	0.0
ϵ_{mx}	0.96	0.95	-1.0	0.97	0.96	-1.0

Table 4.5: As Table 4.2 but for the Central and Eastern regions.

face temperature, changes on circulations patterns that introduce large non-linearities, or simply the surface energy term variations are at a noise level.

According to Figure 4.11b, the cold biases in the CTL simulation are present during all months, but with somewhat larger values during the warm season. The EFT simulation exhibits a larger amplitude of the temperature annual cycle, and while maintaining a negative bias during the cold season, it eliminates the negative bias in summer (in fact, it overcorrects, showing a slightly positive

Var.	Central Region			Eastern Region		
	CTL	EFT	DIFF	CTL	EFT	DIFF
T	20.9	21.7	4.1	19.5	20.9	7.0
NR	120.6	117.8	-2.3	128.1	126.5	-1.3
SHF	55.0	54.0	-1.8	37.9	38.8	2.2
LHF	62.5	62.0	-0.9	85.6	86.6	1.1

Table 4.6: Area averages (Central and Eastern regions) of variables from CTL and EFT ensembles and their differences computed as $[(EFT - CTL)/CTL] \times 100$. The variables are: temperature ($^{\circ}C$), net radiation (Wm^{-2}), sensible and latent heat flux (Wm^{-2}).

bias). Overall, the cold bias in the CTL ensemble in the eastern sector averages -1.3 °C but it is notably reduced in the EFT ensemble to 0.2 °C with a reversal of its sign (Figure 4.11a). Contrary to what might be expected in the central region (Figure 4.11b) the overall EFT ensemble 2-m temperature bias is larger than the CTL ensemble bias (1.3 °C vs 0.4 °C). The EFT simulation reduces the positive bias during the winter months, but increases them during the warm season.

4.3 Discussion: Model Evolution of the Drought

So far the analysis focused on the differences between the CTL and EFT ensembles. Here the drought period will be examined against a mean climatology, where anomalies are computed as the differences between the results of the EFT ensemble and mean values of the 10-year model climatology discussed in the previous chapter. The analysis of a drought from a simulation allows to study a wider set of variables than that formed by the usually observed variables. For instance, heat fluxes are not usually measurable, nevertheless their anomalies can contribute in the comprehension of an event. Also, simulated variables guarantee consistency in balances, while observed from different sources do not. On the other hand, the use of a realistic set of vegetation properties helps to link the changes in some climate variables to the vegetation state.

Figure 4.12 presents the evolution of the anomalies of latent and sensible heat flux, temperature, soil moisture, rain, and runoff averaged for the main drought area (corresponding to 63°W - 55°W and 38°S - 27°S). The first important finding is that the evolution of the simulated precipitation anomalies (Figure 4.12e) is remarkably similar to the satellite and observed precipitation anomalies shown in Figures 4.3a and 4.3b, with an almost continuous deficit of rain from November 2007 to June 2009 and largest dryness in November 2007, April and December 2008 and March 2009. But, did surface effects contribute

to the persistence of these negative anomalies?

As it was found with the observed variables in Figure 4.3, there is a first deficit of rain at the end of 2007 (Figure 4.12d). The reduced precipitation combined with higher temperatures (Figure 4.12a) modified the heat fluxes with respect to normal values. While the sensible heat flux (Figure 4.12a) follows closely the climatology with alternating periods of small negative and positive values, the latent heat flux presents negative anomalies for the whole period (Figure 4.12b), indicating a continuous deficit of evapotranspiration which can be associated with the increased vegetation stress due to the lack of water.

In March of 2008, when a wetter soil is expected as consequence of the high precipitation, a new depletion of rain keeps the soil dry as in summer (Figure 4.12d). Then, the dry soil combined with high temperatures contributed to the vegetation stress, and therefore, to the reduction of evapotranspiration, i.e. negative anomalies of the latent heat flux. The general reduction of the total flux of heat and all terms of the water balance lead to a drier atmosphere. These conditions extended for more than a year intensifying the negative anomalies of precipitation. Towards the end of autumn of 2009 the precipitation become to normal mainly because SSTs also returned to normal (see Figure 4.1). But, local factors such as normal temperatures and heat fluxes contributed as well.

In summary, the dry soil conditions and lower NDVI reported in section 4.1.2 during the drought modified the spatial distribution of some properties like green vegetation fraction, albedo, surface roughness length, and stomatal resistance. When rain is strongly reduced with respect to the climatological values, temperatures are larger than normal, latent heat flux decreases while sensible heat flux slightly increases. The soil moisture is also reduced, with a delay due to memory processes. Low evapotranspiration leads to deficient atmospheric moisture, increasing the stability of the lower atmosphere and intensifying the downward trend of rainfall.

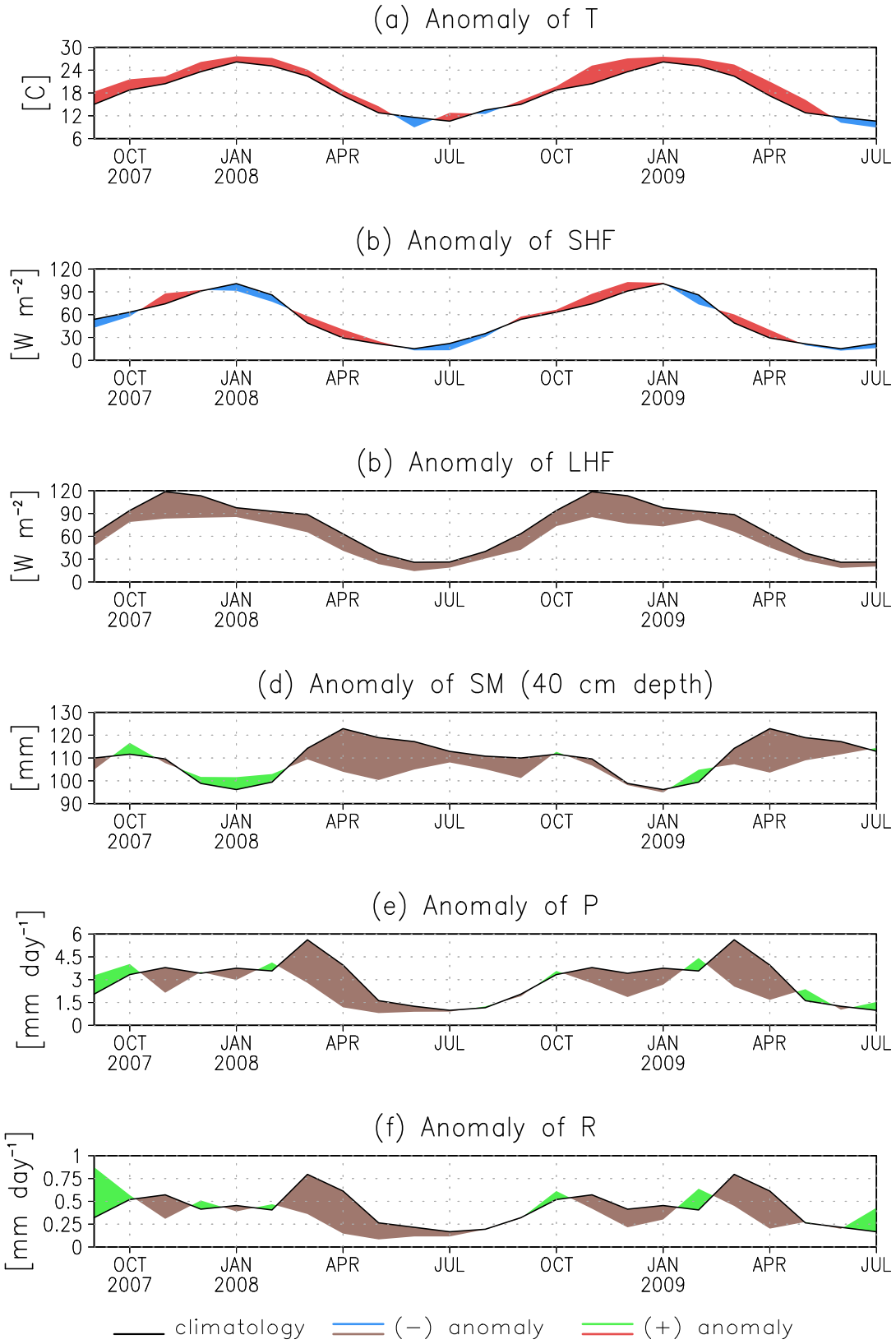

Figure 4.12: Area-averaged anomalies for the main drought area of (a) temperature at 2-m, (b) sensible, and (c) latent heat fluxes, (d) soil moisture, (e) precipitation, and (f) runoff. The anomalies were computed as the difference between the variables of the EFT ensemble and climatology variables from a 10-year simulation (2001-2010).

Chapter 5 | From Research to Application: Forecasting and Monitoring

5.1 Weather Forecasting and Monitoring Systems

La Plata Basin is one of the regions with the highest occurrence of convective storms in the world (Zipser et al., 2006). Due to the features of the region, i.e., the high variability of the regional climate and its influence in economic activities, there is always a need for additional information of hydrometeorological variables on real-time for the users (Müller and Berbery, 2014). Forecasting and monitoring systems, linked with appropriate decision and discussion support tools, could substantially improve operational decision making in agricultural and water management (Stone and Meinke, 2005).

Aldeco (2011) made a review of the evolution of operational forecasts in Argentina and reported that the first attempts with extremely simplified models were found in the early 70s. From that time until the present, the advance in the comprehension of the regional climate coupled with the technological evolution have allowed the implementation of forecast systems based on complex models with high resolution.

Currently, there are a few initiatives for developing this kind of systems. The Servicio Meteorológico Nacional (SMN) of Argentina publishes daily a 96-hr weather forecast of Argentina generated with the Eta Model, and a 18-hr forecast with the Brazilian Regional Atmospheric Modeling System (BRAMS) over the Province of Buenos Aires (García Skabar et al., 2011). Also, SMN monitors information of variables over LPB based on observations. The monitoring is offered as agroclimate and hydroclimate information through bulletins and graphics. The agroclimate section includes weather and climate watch (precipitation, temperature and heliophany), monitoring of crop, vegetation and soil states (NDVI, water balance, etc). The hydroclimate section includes LPB climate watch (precipitation and hydrometry), monitoring of soil state (water balance, available water, etc). Other forecasts are found at the Centro de Investigaciones del Mar y la Atmósfera (CIMA), which publishes a 48-hr forecast based on WRF (Saulo et al., 2008). With regard to other countries in the region, the Centro de Previsão de Tempo e Estudos Climáticos (CPTEC) of Brazil

offers two products of forecasts over South America. They are based on numerical simulation with Eta and BRAMS. The Eta product provides an extended 11-days forecast, and the BRAMS product a 3-day forecast. In terms of monitoring, CPTEC has abundant information but mostly limited to the Brazilian territory. Both national centers (SMN and CPTEC) are pioneers in the region in providing weather information based on numerical models, and the numerical products found at different parts of their web sites are mostly based on Eta and BRAMS models.

The objective of this chapter is to develop predictive capabilities by implementing a real-time forecasting and monitoring system. It is expected that the acquired knowledge about regional climate modeling can be translated to practical information for the users and stakeholders through the proposed system. Particularly the system is tailored for users in northeastern Argentina and other regions of high agricultural productivity and water needs. The development aims to simplify interpretation of the climate information in the region, offering tools with graphical information in a unified system based on numerical simulation with the WRF model, which is the model most used by the worldwide community of climate modelers.

5.2 System Design

5.2.1 Model Simulations

A routine system executed daily and based on climate model simulations was developed to offer climate information for South America, but focusing on the La Plata Basin. All products that make up the system are based on daily routine simulations with the WRF model, i.e., there is no information from other sources, such as, observations. The model performs forecasts for a period of 168-hr (7 days) with output every 3-hr. It ingests initial and 6-hr boundary conditions from the Global Forecast System (GFS) and is run over two nested domains. They are the same that were used for the climatology (see Figure 3.1) with a parent domain covering South America with a resolution of 45 km, and the nested domain centered over the LPB at 15 km. The model parameterization is the same that was used in the climatology.

The output includes variables of meteorological, agricultural, hydrological and social interest such as precipitation, temperature, winds, pressure, soil moisture, evapotranspiration, runoff, and surface heat fluxes. Some variables are shown as total values and, when relevant, others as anomalies. The latter are computed as the difference with climatological variables obtained from the 10-year simulation described in Chapter 3.

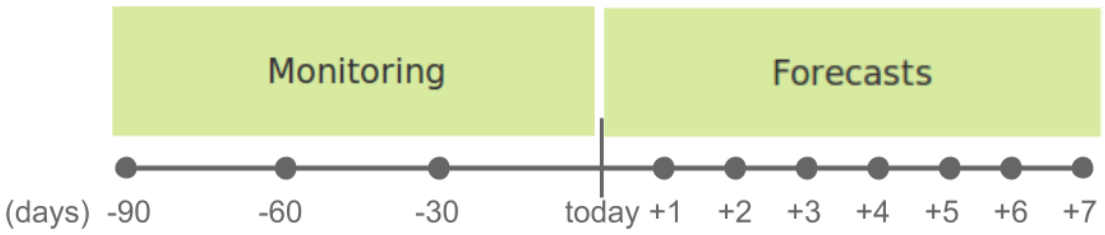

Figure 5.1: Scheme of system modules.

Monitoring Module			
Tool	Description	Variables	Domains
Maps	Time average maps in last 30-, 60- and 90-days showed as total values and anomalies. Eg. Fig. C.1	P, EVT, R, SM at 0.4 and 2.0 m depth, $MAX\ T$ and $MIN\ T$	SA, LPB
Time-Series	Areal average in last 30-, 60- and 90-days of hydrological variables. The time evolution of all variables are shown in one graphic (one below each other). Eg. Fig. C.2	P, accumulated P, SM at 0.4 and 2.0 m depth, EVT and R	Basins: LPB, Paraguay, Upper and Lower Paraná, Uruguay

Table 5.1: Monitoring module tools.

5.2.2 System Overview

The system released in www.atmos.umd.edu/˜berbery/research/forecasts.html consists of two main modules: monitoring and forecasting. Figure 5.1 gives a schematic insight of the system. The monitoring module shows maps and time-series for the last 30, 60, and 90 days of hydrometeorological variables such as precipitation, temperature, runoff, soil moisture, among others. The forecasts module shows the evolution of each variable in the next seven days with a time-step of three hours. All tools in each module are offered for both domains: South America (SA) and LPB. The variables can vary depending the type of product. Tables 5.1 and 5.2 summarize the set of graphics for each module, with a brief description, of variables and region of application.

This set of tools easily characterizes the hydroclimate of the most recent months and what can be expected for the next days. In this way, information is provided for informed decision making by users. Examples include to reduce adverse impacts of anomalous conditions over urban or agricultural areas, plan agricultural activities, decide whether irrigate or not, etc. The Appendix C shows examples of each product included in both modules.

Forecasts Module			
Tool	Description	Variables	Domains
3-hr Maps	Animations showing the evolution of the forecasts for the next 168 hrs with a time-step of 3-hr. Eg. Fig. C.3	P, T, $Winds$ at 10 m	SA, LPB
7-days Ave. Map	Time average map for the forecasts in next 168 hrs. It can be seen as the average of all 3-hr maps. Eg. Fig. C.4	P, EVT, R, SM at 0.4 and 2.0 m depth, $MAX\ T$, $MIN\ T$ and $Winds$ at 10 m	SA, LPB
Meteogram	Time evolution of all variables for a specific location in one graphic (one below each other). Eg. Fig. C.5	P, EVT, SM at 0.4 and 2.0 m depth, R, T, $Winds$ at 10 m	Specific Locations

Table 5.2: Forecasts module tools.

5.3 Forecasts Verification

Since the entire system is based on daily forecasts, it is essential to evaluate their quality with observations. The evaluation presented here is restricted to the inner domain and to daily values of precipitation and temperature at 2-m, as they are the most commonly measured variables.

There are many methods of verification applicable to different types of forecasts. The methods can vary from visual ("eyeball") verification, which assess visual and subjectively individual events, to object oriented methods, which verify the properties of spatial forecasts of entities, where an entity is anything that can be defined by a closed contour, for instance, contiguous rain areas (Stanski et al., 1989). For each entity that can be identified in the forecast and the observations, these methods use pattern matching techniques to determine the location error, as well as errors in area, mean and maximum intensity, and spatial pattern.

The objective on this work is to characterize the forecast skill with statistical measures of simple interpretation and general spatial and temporal representation. Complex methods are in general applicable to simple events rather than long sets of forecasts. Here, the period of evaluation begins on August 01, 2012 and ends on October 10, 2014, i.e., 804 days.

The observation data set (hereinafter called OBS) is from the National Climate Data Center (NCDC) of the United States, which gathers daily summaries of gauge station data from more than 9000 worldwide stations provided by different national weather services. Among the stations located inside the domain, we select those that pass a threshold of availability, i.e., those with the fewest undefined values for the period of evaluation are used, as to be considered statistically representative.

The forecasts data set (hereinafter called FCST) is a collection of 7 individual data sets, one per forecast day. For instance, the simulation issued on 01-AUG-2012 generates 7 days of forecasts —from 01-AUG-2012 (day 1) to 07-AUG-2012 (day 7)— that should be compared against the corresponding 7 observations days. In all cases, each station data is compared to the forecast in the nearest grid point.

5.3.1 Precipitation Verification

The precipitation is evaluated in terms of occurrence of daily events. When observed precipitation for a given day is more than a preset rainfall threshold, it is considered a rainy day. Then, methods for dichotomous (yes/no) forecasts can be applied. This methods have the disadvantage of double-counting penalty where a rainstorm displaced in space is scored worse than either a complete miss or a false alarm since it is penalized as both at once (Kok et al., 2008). But in turn, they are suitable when observed fields are not available allowing a simple and intuitive interpretation, which is the goal of this verification (Tartaglione, 2010).

Once the days are classified as rainy or dry (yes/no), contingency tables are calculated in order to verify daily precipitation events (P). A contingency table (see Table 5.3) shows the frequency of "yes" and "no" forecasts and occurrences for a given place (Wilks, 2011). It is a useful way to see what types of errors are being made. The four combinations of forecasts (yes or no) and observation (yes or no), called the joint distribution, are:

- hit (h): event forecast to occur, and did occur;
- miss (m): event forecast not to occur, but did occur;
- false alarm (fa): event forecast to occur, but did not occur;
- correct negative (cn): event forecast not to occur, and did not occur.

A large variety of categorical statistics can be computed from the elements in the contingency table to describe particular aspects of forecast performance.

		OBS		
		YES	NO	TOT
FCST	YES	hits	false alarms	forecasts yes
	NO	misses	correct negatives	forecasts no
	TOT	observed yes	observed no	total

Table 5.3: Contingency table.

In this research four statistical values are selected including the accuracy (A),

$$A = \frac{h + cn}{total}; \tag{5.1}$$

the Probability of Detection (POD), also known as Hit Rate (H),

$$POD = \frac{h}{h + m}; \tag{5.2}$$

the False Alarm Ratio (FAR),

$$FAR = \frac{fa}{fa + h}; \tag{5.3}$$

and the Bias score or frequency bias ($BIAS$),

$$BIAS = \frac{h + fa}{h + m}; \tag{5.4}$$

The accuracy A (Equation 5.1) indicates what fraction of the forecasts were correct. The result can vary between 0 and 1, being 1 the perfect score. The probability of detection POD in Equation 5.2 shows what fraction of the observed "yes" events were correctly forecast. POD ranges from 0 to 1, being 1 the perfect score. The false alarm ratio FAR defined in Equation 5.3 answer the question: What fraction of the predicted "yes" events actually did not occur (i.e., were false alarms)?. Perfect score is 0, but possible values goes from 0 to 1. Finally, the $BIAS$ presented in Equation 5.4 measures the ratio of the frequency of forecast events to the frequency of observed events. It indicates whether the forecast system has a tendency to underforecast ($BIAS < 1$) or overforecast ($BIAS > 1$) events, being 1 the perfect score. It does not measure how well the forecast corresponds to the observations, only measures relative frequencies.

5.3.2 Temperature Verification

Temperature is assessed in terms of minimum, mean and maximum daily temperature (T_{mn}, T and T_{mx} respectively). Unlike precipitation verification where

just yes/no events were evaluated, here the objective is to measure how the magnitudes of the forecasts differ from the magnitudes of the observations. This kind of verification methods include selected scatter plots or box plots, as well as various summary scores. In this study, scatterplots are selected and the Mean Absolute Error (MAE) and the Correlation Coefficient (r) given by:

$$MAE = \frac{1}{N}\sum_{i=1}^{N}|FCST_i - OBS_i|, \tag{5.5}$$

$$r = \frac{\sum_{i=1}^{N}(FCST_i - \overline{FCST})(OBS_i - \overline{OBS})}{\sqrt{\sum_{i=1}^{N}(FCST_i - \overline{FCST})^2}\sqrt{\sum_{i=1}^{N}(OBS_i - \overline{OBS})^2}} \tag{5.6}$$

where N is the total number of days, $FCST_i$ is forecasted T (minimum, mean or maximum) for the day i and OBS_i is observed T (minimum, mean or maximum). $\overline{FCST}$ and $\overline{OBS}$ denote the mean value of the series. From Eqn. 5.5, the mean absolute error (MAE) shows the average magnitude of the forecasts error, the ideal score is 0, but it can get any positive value. The correlation coefficient (r) in Eqn. 5.6 indicates the correspondence between forecast and observed values. It varies from -1 to 1, reaching a perfect score when $r = 1$.

5.4 Verification Results

Contingency tables for daily precipitation events and scatterplots for daily temperature, as well as their statistics, were computed for all stations in the domain. For practical reasons, they are shown here only for a sample station arbitrarily selected. It is "Sauce Viejo Aero" (id 873710) which is located at 31.7°S, 60.82°W, in the Province of Santa Fe, Argentina. Then, the behavior of precipitation and temperature forecasts for all stations in the region of interest are summarized with skill curves and maps. The rainfall threshold is set to 0.25 *mm*, coincident with the minimum measurable precipitation of most rain gauges (bucket type). The availability threshold is set to 724 days, that is, more than 90 % of the 804 days analyzed. Stations with more than 80 undefined daily values are discarded.

5.4.1 Precipitation

For the sample station, a contingency table per forecast day is presented in Table 5.4 (from 5.4a to 5.4g). The statistics over these tables indicate that the forecast offers an accuracy of 0.72 for maximum lead time (day 7) that reaches 0.79 for day 1. The POD varies from 0.58 to 0.72, with decreasing values

FCST (day 1)	OBS YES	OBS NO	OBS TOT
YES	120	110	230
NO	47	486	533
TOT	167	596	763

FCST (day 2)	OBS YES	OBS NO	OBS TOT
YES	121	113	234
NO	49	477	526
TOT	170	590	760

FCST (day 3)	OBS YES	OBS NO	OBS TOT
YES	123	103	226
NO	44	491	535
TOT	167	594	761

FCST (day 4)	OBS YES	OBS NO	OBS TOT
YES	117	121	238
NO	49	474	523
TOT	166	595	761

FCST (day 5)	OBS YES	OBS NO	OBS TOT
YES	119	145	264
NO	48	450	498
TOT	167	595	762

FCST (day 6)	OBS YES	OBS NO	OBS TOT
YES	110	136	246
NO	55	461	516
TOT	165	597	762

FCST (day 7)	OBS YES	OBS NO	OBS TOT
YES	94	142	236
NO	67	454	521
TOT	161	596	757

Table 5.4: Contingency tables for the Sample Station “Sauce Viejo” located in Santa Fe, Argentina. There is one table for each day of forecast, it is indicated as FCST (day #).

as lead time increases. In other words, observed rainy days are not predicted (misses) in about 28 % for day 1, reaching roughly 40 % for day 7. In general, the successes in forecasts ($h + cn$) almost triple (2.62 in the worse case) the amount of failures ($m + fa$).

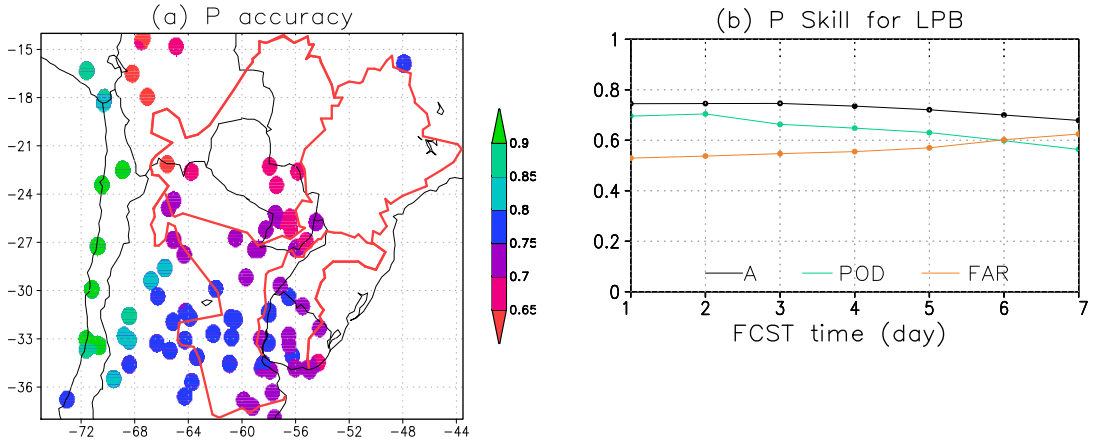

Figure 5.2: Forecasts skill for P. The map (a) averages in time the accuracy of FCST (from day 1 to day 7) with respect to observations for each station. The times-series (b) averages in space over LPB: the accuracy, the probability of detection and the false alarm ratio of all forecasts grid points under evaluation, i.e. points inside LPB.

Among the failures, the most common are false alarms, which exceed the number of hits when the forecast lead time is 4 days or more. It is consistent with the *BIAS* that varies between 1.37 and 1.47 suggesting a tendency of model to over-forecast events. Note that, according to what is expected, the successes tend to decrease and failures tend to rise when the forecast time increase.

As noted above, the positive results presented take into account just one sample station. To make a complete verification, all stations in the domain are verified with contingency tables, and then the results are summarized in Figure 5.2.

The map of FCST accuracy for P (Figure 5.2a) shows the average of the 7 days of forecasts for the 84 gauge stations. The figure shows the lowest results in the northern part of the domain (mainly in Bolivia and Paraguay) with accuracy values below 0.7, but the forecast performance improves toward the southern part of the domain with values up to 0.7. Focusing on the LPB region the accuracy values varies from 0.6 in the Upper LPB to 0.8 in the Lower LPB. Notably, the best results are found in Chile and west Argentina where the topography implies an extra issue for the model. Here, the accuracy scores vary in this region from 0.8 to 1 indicating that more than the 80 % of rainy or not rainy days were correctly forecast. The good performance in this region is directly related to the high score of correct negatives. The region is mostly dry and the model is able to represent the region climate as shown in Chapter 3. Also, the high resolution considered in the model configuration contributed as well. It satisfactorily represents the role of the strong local forcing of the topography on the region's precipitation regimes.

Figure 5.2b presents the evolution of skill scores with forecast time. The curves average the results of all valid stations for LPB adding up 46 out of 84. The accuracy *A* (black curve) shows almost no changes in time, with values above 0.70. That is, the model succeeds to forecast at least 70 % of the occurrence of rainy or dry days for LPB. The curve of *POD* starts with a value of 0.70 and decreases to about 0.55 for maximum lead time. In other words, the percent of observed rainy days that were correctly forecast varies from 55 % to about 70 % (from day 7 to day 1).

The *FAR* score (the orange curve) indicates that around the 55 % of the forecast rainy days were false alarms (did not occur). This is also reflected in Table 5.3 for the sample station. There are not specific studies in the bibliography talking about high *FAR* in operational forecasts with WRF in South America. However, three issues could be contributing to it:

1. The model tends to over-forecast rain. Different authors, such as Weisman et al. (2008) and Dravitzki and McGregor (2011) among others, also reported high *FAR*. In the first case, the evaluation of a 36-hr forecast of convective rainy events on central USA had a *FAR* above 0.4 with the WRF model using the Betts-Miller-Janjic scheme (the same used here). The second work reported *FAR* varying from 0.50 to 0.75 for 6-hr forecasts of heavy rainfall in New Zealand with the WRF model. Beyond this, in both cases the authors highlight the capacity of the model to reproduce the structure and evolution of convective rain.

2. The uncertainty of observations. The works mentioned recently noted that the values can change depending on the selected rainy threshold. In this case, 0.25 *mm* could be very low to be noted by the observer in conventional gauge stations. But even more important than the threshold is the period of hours that is considered a day. While a day is considered from 0 to 24-hr UTC in this work, many observations define days in local time.

3. The double-penalty derived from the comparison grid-point vs gauge station. This kind of verification methods tend to penalize with false alarm and miss when an observed feature is displaced from the forecast feature. Further analyses should be done to fully understand the causes of high *FAR* but it lies beyond the scope of this thesis.

5.4.2 Temperature

The observed temperature during a day (minimum, mean and maximum) for the sample station is compared against the 7 forecasts of temperature for the same day in Figure 5.3 with scatterplots. It is a common practice when working

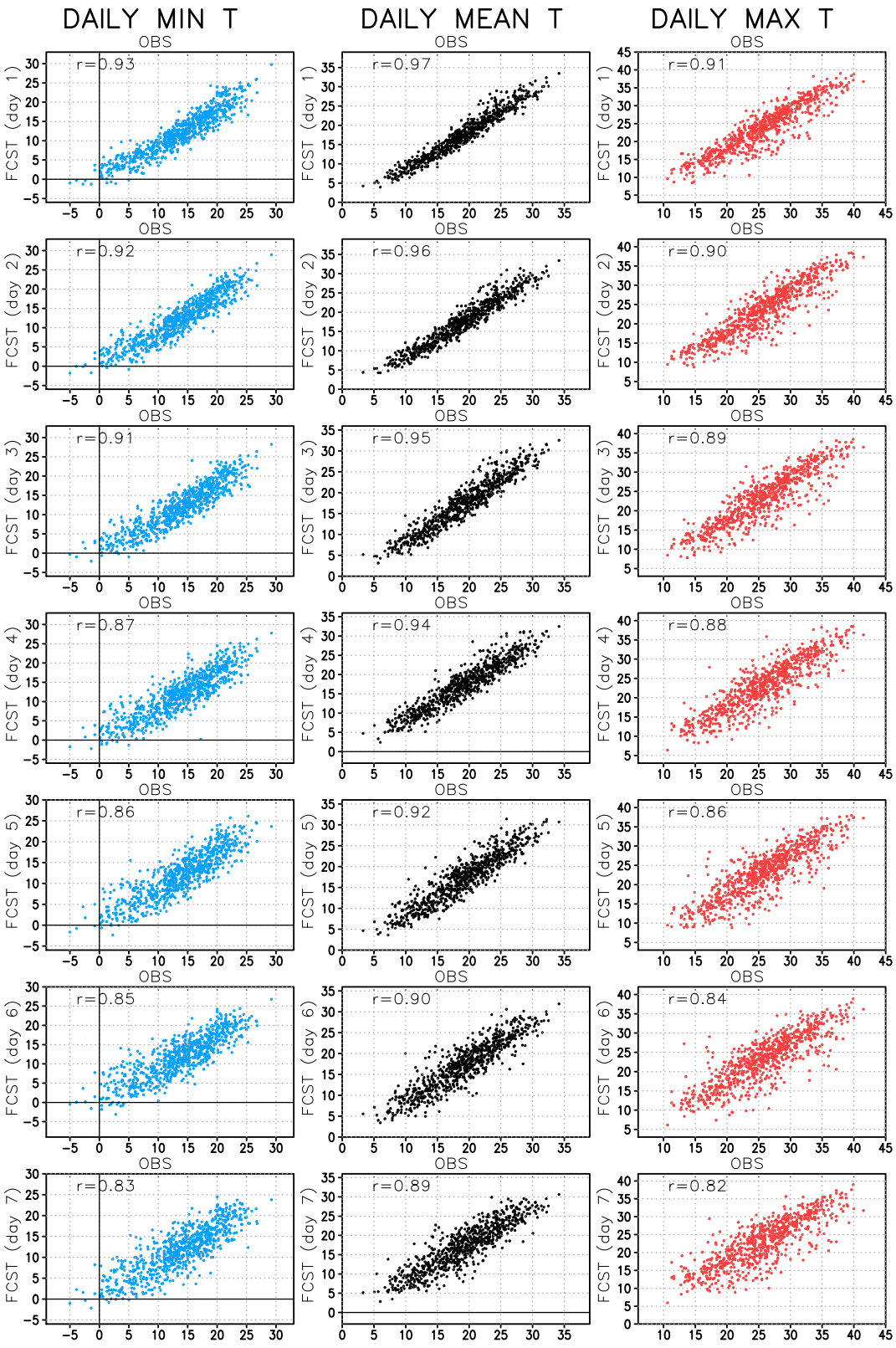

Figure 5.3: Scatter plots for daily minimum temperature (left column), mean temperature (central column) and maximum temperature (right column) comparing forecast values with observations in the sample station. Each row of scatter plots corresponds to each day of forecasts as indicated by the label of intercept axes. Also, the correlation is showed in the top left corner of each scatter plot.

with model forecasts to define the minimum and maximum values from the 3-hr forecasts, therefore they cannot define exactly the precise moment of the occurrence (a 1.5-hr uncertainty is present). This uncertainty leads to more scattered points and lower correlation for T_{mn} and T_{mx} when they are compared with T. Also, it is noted that as forecasts approach the issue date (looking at the pictures from bottom to top), the points tend to cluster together and the correlation coefficient improves. The coefficient are always greater than 0.8 for T_{mn} and T_{mx} and greater or equal than 0.89 for T, reaching a correlation of 0.97 for the minimum lead time.

The correlation maps (Figures 5.4a, c and e) for T_{mn}, T and T_{mx} respectively are an average in time of forecasts at different lead times over the nearest grid points of 137 stations. They show similar patterns with an increasing correlation from the north, with correlation coefficients around 0.7, to the south with correlation coefficients above 0.9. As expected, T slightly improves the correlations with respect to T_{mn} and T_{mx}. The spatial gradients agree with the verification of precipitation where the forecasts has better results towards the south. Inside LPB (tested in 64 stations), the forecast in the southern part has an almost homogeneous correlation of 0.9 or more for T and above 0.8 for T_{mn} and T_{mx}. Then, in the Paraguay and the Mid-Upper subbasins, most values vary from 0.7 to 1 for T, T_{mn} and T_{mx}. Summarizing, it is found that the forecasts for LPB temperature have an average correspondence with observations of more than 80 %, with few exceptions in the northern border of the basin.

From the point of view of time evolution of the forecasts skill, Figure 5.4b, d, and f show a very good correspondence between observed and forecast temperatures with correlations (black curves) above 0.8 with exception of T_{mx} for FCST(+6). The forecast biases vary in magnitude between 2 $^{\circ}C$ and 4 $^{\circ}C$ (blue curves). The best performance is for T curves, where the correlation is about 0.95 for day 1 and decreases to 0.83 for day 7 and the MAE is always below 3 $^{\circ}C$. T_{mn} has a similar curve of MAE, but it presents lower correlations that starts with 0.9 and decrease to 0.8 for maximum lead time. Finally, the T_{mx} correlation curve varies from 0.88 to 0.78, with MAE that begins with 2.7 $^{\circ}C$ and reaches a maximum error of 3.7 $^{\circ}C$.

In summary the forecasts of temperature (either, minimum, mean or maximum) present a very good correspondence with observed values in LPB, mainly in the southern subbasins, where the correlation is in general above 0.9. The magnitude of the difference is between 2 $^{\circ}C$ and 3 $^{\circ}C$ for minimum and mean temperatures, but rises to almost 4 $^{\circ}C$ for maximum temperature. Note, that minimum, mean and maximum temperature of forecast are computed among eight values for each day as the forecasts outputs are 3 hourly, then the values, mainly minimum and maximum have a 1.5-hr of uncertainty that can derive in higher biases.

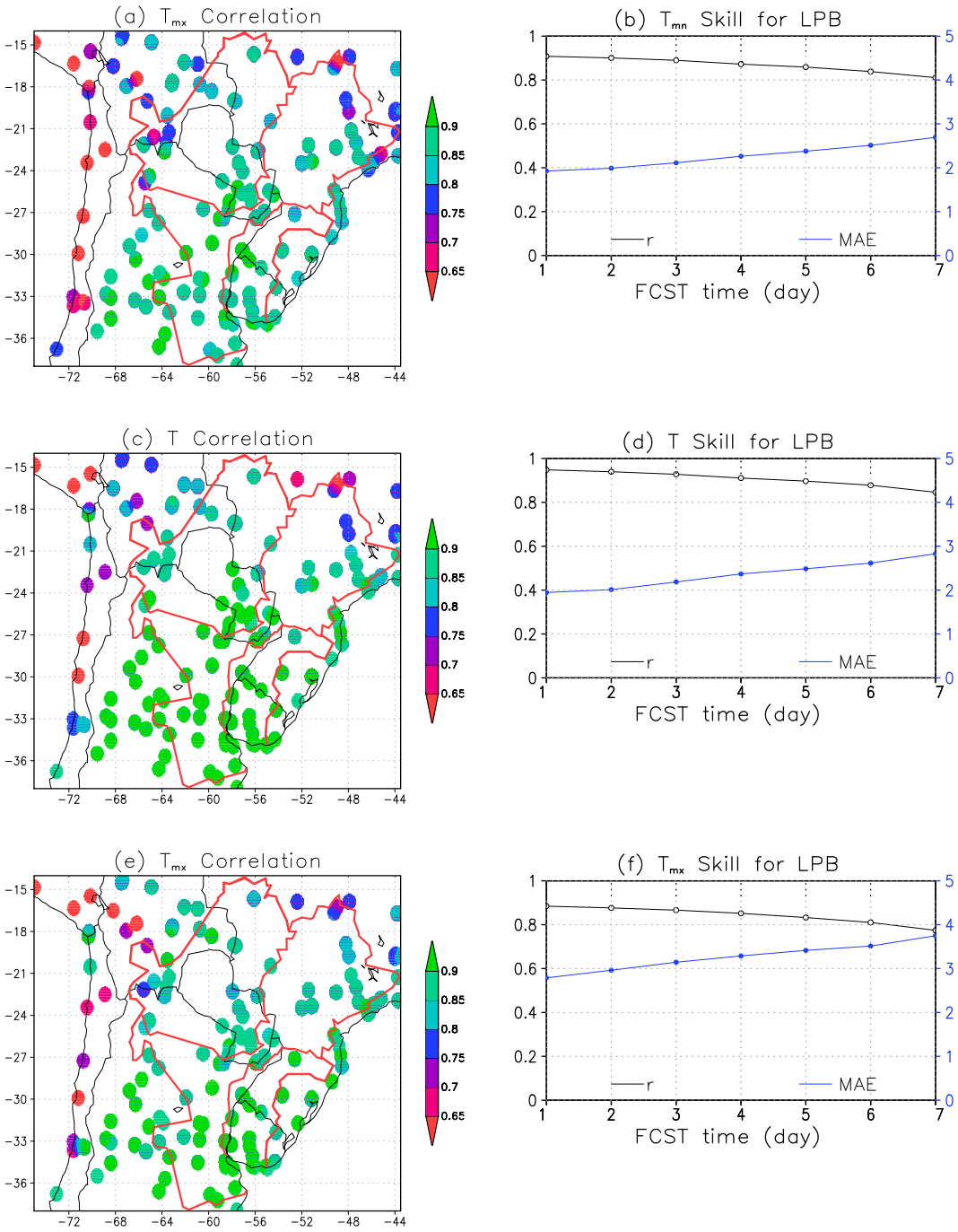

Figure 5.4: Forecasts skill for T. The maps (a), (c), and (e) averages in time the correlation of T_{mn}, T, and T_{mx} between FCST (from day 1 to day 7) and observations for each station. The times-series (b), (d), and (f) averages in space over LPB the T_{mn}, T, and T_{mx} correlation coefficients, and the mean absolute error, for all forecasts grid points under evaluation, i.e. points inside LPB.

5.5 Discussion: System Usefulness and Quality

An operational system based on model simulations was developed with the objective of offering information as support for agriculture, hydrology and risk management. The effort seeks to provide tools for monitoring and forecasting in an unified system. The set of tools allows easily to characterize the last months and what can be expected for the next days in order to plan activities, and reduce impacts of anomalous conditions.

Every day high resolution simulations are carried out over South America, and a nested domain covering La Plata Basin. The results of routine model simulations were evaluated against gauge station data for two variables: the occurrence of daily precipitation and daily temperature (minimum, mean and maximum). The forecasts of both variables show a good performance for the basin with better results in the southern part of the basin. The verification of the forecast skill shows an average accuracy of about 70 % for rainy days, and about 85 % of correlation with observed temperatures. The skill of the forecasts has a slow decrease with the increasing forecast time. This feature, observed for precipitation and temperatures, suggests that the period could be extended for more than 7-days of simulation (but remaining within the ranges of predictability of the dynamical system).

Currently, the system output is used as input of an early warning system for flows by the Instituto de Hidrología de Llanuras “Dr. Eduardo Usenoff” of UNICEN. Also, the system is used to support the daily weather report and extended forecasts of the Centro de Informaciones Meteorologicas of FICH, UNL. In both cases the users value positively the utility of the system and recognize it as a key tool for their applications.

Chapter 6 | Conclusions

6.1 Conclusions and Future Work

This dissertation focused on the analysis of the land cover changes effects on the regional climate and therefore the forecasts of hydrometeorological variables. Four major objectives were defined under the hypothesis that a realistic representation of the land cover properties helps improve the simulation of the land surface-atmosphere interactions and hence can reduce model biases that are inherent to surface processes. In this section, the conclusions are expressed as specific answers to each proposed objective (with abbreviated titles). Also, some comments about future work related to each topic are presented throughout the text.

6.1.1 Objective 1: Investigate Model Skill on LPB

It is of great interest to have a reliable high-resolution simulation to address studies of physical processes. The current WRF model skill was studied in Chapter 3 through the analysis of a long-term high resolution simulation. The overall results suggest that the proposed model parameterization is suitable to represent the regional climate. The model results are consistent with general aspects of the regional climate. For instance, the wet conditions –in terms of precipitation and soil moisture– over the Upper Paraná Atlantic Forest and the gradient towards the driest region over the Atacama Desert, were correctly represented, and likewise the large seasonal precipitation variability to the north modulated by the presence of a monsoon system. Also, the temperature pattern presents largest values to the north that gradually decrease towards the south as expected win higher latitudes.

The largest biases of the analyzed variables were observed over the Andes Cordillera. This was expected due to the model's comparatively low resolution (to reproduce sharp topographic features) and because the parameterizations do not properly reproduce the processes inherent to mountain-dominated areas. Further, observations have their own limitations due to the sparsity of the rain

gauges, impeding a correct assessment.

Focusing on LPB, the region of interest, the model and observed precipitation correlations are high (a minimum value of 0.77 is found) for different sub-basins and seasons. The WRF model simulates more frequent and less intense rainy days than found in the observations. On the other hand, the probability of occurrence of moderately to extremely wet months is notably similar between WRF and observations. Analysis of *SPI* was done over particular locations. One of these locations is close to the Marcos Juarez station in the Province of Córdoba. Here, the model identified the 2007/9 drought with similarities in the period of occurrence and intensities. It was a good clue to continue studying that particular event. However, the model tended to exaggerate the intensity of the drought.

In general, the model showed a tendency to generate negative biases, i.e. drier conditions in precipitation and soil moisture, which could lead to difficulties in the representation of severe or extreme droughts when *SPI* was analyzed, especially in Upper LPB. Because the model climatology is drier than in observations, it does not show as many dry anomalies as were observed.

The simulated temperatures have a very high correlation for Lower LPB in all seasons, while Upper LPB has high correlation in dry/cold season, but it decreases in warm months due to the hot biases in Paraguay sub-basins. The long-term simulation showed warmer temperatures over Paraguay sub-basin, and slight colder temperatures over the east side of LPB (Mid-Upper Paraná and Uruguay sub-basins). In Lower Paraná the model combined hot biases toward northwest with slight cold biases towards south.

In summary, the long-term simulation demonstrated a very good performance of the model in the region of interest, making it a useful climatology for studies of physical processes. The proposed parameterization was suitable to represent the regional climate. Nevertheless, some biases appear in the analysis of different variables, mainly in Upper LPB. The reduction of those biases were the motivation to test more realistic land surface conditions that could lead to better forecasts. In the future the simulations will be extended in time and testing the ecosystem functioning approach, in order to get a more representative climatology.

6.1.2 Objective 2: Improve Model Skill with EFTs.

Recent efforts have produced a number of high-quality remotely sensed land cover maps that can be used to better represent the land surface states eventually improving the performance of climate models. This research contributes to this line of research by presenting a new approach to describe vegetation

in regional models with information obtained from satellite-based estimates of ecosystem functional properties. New time-varying maps of the land surface biophysical properties were created using Ecosystem Functional Types, which capture the changes of vegetation status due to anomalous climate conditions as well as changes due to land use practices. This approach ensures the use of a consistent set of biophysical vegetation properties that reflect actual land surface conditions in long-term simulations with the WRF model. The method should be most helpful when actual conditions depart from mean values as it happens during extreme events. To confirm this hypothesis, Chapter 4 focused on land surface processes during the 2008 severe drought of southern South America, while also examining other regions where positive model biases were large.

Simulations using the standard surface conditions (USGS land cover map) represent the spatial pattern of precipitation, but tend to exaggerate the drought severity while producing large excesses of precipitation in other regions. The temperature is reasonably well simulated in magnitude and distribution except for cold biases towards the eastern coast, and large biases over the Andes Cordillera and its eastern slopes. Vegetation changes due to the drought or to land use changes modify the spatial distribution of the surface biophysical properties. The use of the new data set of EFT-based vegetation properties as a replacement of the conventional land cover types in the WRF/Noah model offers evidence that time-varying land cover properties do impact the performance of coupled land-atmosphere models. Particularly, the use of the novel EFT data set leads to an improvement of the drought simulation and reduces the wet biases in most (but not all) regions of large precipitation. The results demonstrate that the model is sensitive to land cover changes and vegetation variability through land-atmosphere interactions.

Precipitation estimates showed improvements in most regions, but mixed results were obtained for the temperature bias: The use of EFTs produced a significant reduction of the negative anomalies of temperature (cold bias) towards the eastern part of the domain over land. On the other hand, the near surface temperature simulation was degraded over the central region, where the warm bias was increased by about 1 $^{\circ}C$. The reasons for this inconsistency are yet not understood and may be inherent to parameterizations that tend to tune terms for better results. While beyond the scope of this work, further examination will require to combine the study of surface states with corresponding changes in parameterizations. In addition, advective processes have not been discussed in this work, but there are indications that they may play an additional role in defining temperature in this region.

The EFTs approach allows a suitable characterization of the actual surface conditions (the state of the vegetation), which is the bottom boundary condi-

tion for model simulations (e.g., WRF/Noah, as applied to this study). With near-real time availability of EFT data sets, the method may have implications for numerical weather prediction as well, so that this approach could be used for both weather and climate models. NCEP operations currently use fixed land cover types and an older 5-yr climatology of green vegetation fraction, which is derived from NDVI data. NCEP is exploring the use of a near-real time GVF product and the use of the future "Noah-MP" LSM that has CO2-based photosynthesis, an explicit canopy, and dynamic (growing) vegetation, among other upgrades (Niu et al., 2011). A desired next step will be to combine the methodology presented here with the future Noah-MP. One additional consideration is that for operational numerical weather prediction and seasonal climate forecasting, EFTs need to smoothly vary from season-to-season/year-to-year, similar to the near-real time GVF derived from weekly observed NDVI that NCEP plans to use. In that case, it will be necessary to explore how the near-real time GVF maps can be best combined with the 64 EFT categories.

6.1.3 Objective 3: Understand the Impact of Land Cover / Land Use Changes.

The evaluation of the new approach in Chapter 4 allows to draw conclusions about the effect of land cover changes in surface processes and then, in the overlying atmosphere. A specific interpretation for the precipitation and 2-m temperature changes is not always apparent due to the complexity of the system, including the type of land cover (or EFT) that prevails in each region, and the dominant precipitation/circulation regimes to which each region is subject. Further, while the Noah LSM follows a single column approach, its use over a grid and coupled with WRF implies that nonlinear three dimensional effects will take place. Land cover changes will favor the generation of surface gradients for different variables, which in turn will induce local circulations and differential surface heat fluxes. Advective processes will be influenced, as will be the moisture flux convergence.

In general, the results showed that when the land cover change reduces the soil moisture content, also the evapotranspiration is reduced, while sensible heat flux increases, leading to lower precipitation and runoff. Conversely, regions where the soil moisture content has increased are associated with sensible heat flux reductions and latent heat flux increases that favor a moister boundary layer and increased rainfall and runoff. In other words, soil moisture is positively (negatively) correlated with latent heat flux (sensible heat flux). In turn, the correlation between latent heat (sensible heat) and precipitation is also positive (negative). As discussed, deviations from this behavior are found when regional circulations develop also as a result of land cover changes.

The most clear example of land use change (human induced) detected on the experiments is in the Upper Paraná Atlantic Forest. The replacement of subtropical humid forests by crops in last decades led to a large reduction of surface roughness and increased albedo. These conditions smooth the total flux of heat and then generate weaker turbulent exchanges producing lower precipitation, soil wetness and runoff.

The drought of 2008 is an example of land cover change of natural origin. The drought began with negative anomalies of precipitation that affected the soil and land cover conditions. After some months of delay, the soil started to dry out and the region exhibited lower vegetation greenness fraction, leaf area index, and higher stomatal resistance. The generalized dry conditions hindered evapotranspiration processes and thereby the occurrence of high precipitation. These processes contributed to the duration of the drought that extended for almost 2 years.

As noted above surface processes derived from land cover or land use changes are not always of direct interpretation. The experiments of this study helped improve the understanding of these processes. On future work the general feasibility of this approach will be investigated. First, the severe drought of 2012 in central US will be studied also with the use of the EFT approach. The main goal will be to continue studying the suggested processes in a domain with large amount of observed data, allowing a more reliable assessment.

6.1.4 Objective 4: Develop Predictive Capabilities.

Weather information is usually required and appreciated by different stakeholders in decision-making. In Chapter 5 a comprehensive forecasting and monitoring system is presented and evaluated. The set of tools in the system allow an easy characterization and monitoring of the recent months climate, and predicts several days in advance, helping to plan activities, and reduce adverse impacts of anomalous conditions.

All system products are derived from daily 7-day forecasts. Then, the results of routine model simulations were evaluated against gauge station data in terms of occurrence of daily precipitation and daily temperature (minimum, mean and maximum). The forecasts of both variables show very good skill scores on LPB, mainly in the southern part of the basin. In particular, the occurrence of daily precipitation is predicted with an accuracy of about 70 % average and daily temperatures have an average correlation with observations of about 85 % with mean absolute errors varying between 2 $^{\circ}C$ and 4 $^{\circ}C$. The forecast skill remains in a range of suitable quality throughout the simulation period, suggesting that it could be extended to more than 7 days.

Official forecasts are sole responsibility of the Servicio Meteorologico Nacional. The system described here was developed in the research environment of a university, and as such is offered ”as is”, without guarantees and therefore not carrying any liability. Yet, it is noted that the system output is used as input of an early warning system for flows, to support the daily weather report and extended forecasts, and to planning activities in rural areas. In all cases the users value positively the utility of the system and recognize it as a key tool for their applications. The system was recently developed and has less than three years on line. It is expected that the current errors will be reduced in the future applying bias correction methods. Future work will deal with the inclusion of seasonal forecasts and indexes such as Standardized Precipitation Index, Standardized Runoff Index, among others, which will facilitate the interpretation for monitoring.

6.2 Publications and Awards Resulting from the Thesis

The advances derived from this thesis were published at conferences, congresses, seminars, journals and book chapters. Also, part of this research was awarded in an international conference.

6.2.1 Awards

- Müller, O. (2011). “WCRP Award for Best Scientific Presentation: In recognition of excellence in research and compelling presentation at the WCRP Conference”. The best 5 among the 500 works presented by young scientists were recognized with this award on the *WCRP Open Science Conference: Climate Research in Service to Society.* October 24th-28th. Denver, USA.

6.2.2 Publications

- Alcaraz-Segura, D., Berbery, E., Müller, O. and Paruelo, J. (2013). “Characterizing and Monitoring Climate Regulation Services”. In: Alcaraz-Segura, D., Di Bella, C. and Straschnoy, J.. *Earth Observation of Ecosystem Services.* CRC Press-Taylor and Francis. 418 p. ISBN: 9781466505889.
- Müller, O. V., Berbery, E. H., Alcaraz-Segura, D. and Ek, M. (2014). “Regional Model Simulations of The 2008 Drought in Southern South America Using a Consistent Set of Land Surface Properties”. *Journal of Climate.*, 27: 6754-6778.

6.2.3 Keynote Talks

- Berbery, E. H., Mo, K. and Müller, O. (2013): "Droughts in Southern South America: Large-Scale Dynamics and Regional Processes". *Joint Conference of the 11th AsiaFlux International Workshop, the 3rd HESSS, and 14th Annual Meeting of KSAFM "Communicating Science to Society: Coping with Climate Extremes for Resilient Ecological-Societal Systems"*. August 21th-24th. Seoul, Korea. Participation: co-author.

- Berbery, E. H., Mo, K., Müller, O. and Sgroi, L. (2014): Large-Scale Dynamics and Regional Processes Affecting Droughts in Central Argentina. *2nd International Congress on Plains Hydrology*. September 23th-26th. Santa Fe, Argentina. Participation: co-author.

6.2.4 Invited Talks

- Berbery, E., Alcaraz-Segura, D., Lee, S.-J. and Müller, O. (2011). "The Effects of the Surface Conditions on Extreme Events: Regional Model Simulations using Ecosystem Functional Types". *WCRP Workshop on Drought Predictability and Prediction in a Changing Climate.* March 2nd-4th. Barcelona, Spain. Participation: co-author.

- Berbery, E. and Müller, O. (2011). "Land Surface Effects on Heavy Precipitation over Subtropical South America". *IUGG 2011 General Assembly. Earth on the Edge: Science for a Sustainable Planet.* Jun 28th-July 7th. Melbourne, Australia. Participation: co-author.

- Berbery, H., Mo, K. and Müller, O. (2011). "On the Remote and Regional Forcings of Extreme Events in Southern South America". *AGU Fall Meeting 2011: Session Climate Extremes, Weather and Climate Extremes in the Americas.* December 5th-9th. San Francisco, USA. Participation: co-author.

6.2.5 Contributed Talks and Seminars

- Müller, O., and Berbery, E., (2011). Hydrometeorological Simulations and Their Sensitivity to Land Use Changes in La Plata Basin. *Weekly seminar of Land Surface Hydrology Group of University of Washington*. July 20th. Seattle, USA. Participation: expositor.

- Müller, O., and Berbery, E., (2014). Routine Forecasting and Monitoring System for Agricultural and Hydrological Applications on La Plata Basin. *2nd International Congress on Plains Hydrology*. September 23th-26th. Santa Fe, Argentina. Participation: expositor.

6.2.6 Poster Presentation

- Müller, O. and Berbery, E. (2011). "The Role of Vegetation during the Argentine Drought of 2008". *WCRP Workshop on Drought Predictability and Prediction in a Changing Climate*. March 2nd-4th. Barcelona, Spain. Participation: expositor.

- Müller, O., Berbery, E. and Alcaraz-Segura, D. (2011). "Using Ecosystem Functional Types as Lower Boundary Conditions in Simulations of Droughts in Southern South America". *WCRP Open Science Conference: Climate Research in Service to Society*. October 24th-28th. Denver, USA. Participation: expositor.

- Müller, O. and Berbery, E. (2012). "Representing Vegetation with Ecosystem Functional Types in WRF Simulations". *13th Annual WRF Users' Workshop*. June 25th-29th. Boulder, USA. Participation: expositor.

Appendix A | Lookup Tables for Land Cover Properties in Noah LSM

The lookup tables for land cover types in the Noah LSM define the value of 15 biophysical properties for each type or category. Both classifications available in the Noah LSM (USGS and IGBP) share the following properties:

- shdfac (GVF): Green vegetation fraction [fraction 0.0 to 1.0],
- nroot (i): Rooting depth [soil layer index],
- rs (rs): Stomatal resistance [s m-1],
- rgl (rgl): Parameter used in radiation stress function [dimensionless],
- hs (hs): Parameter used in vapor pressure deficit function [dimensionless],
- snup ($snup$): Threshold water-equivalent snow depth [m] that implies 100% snow cover,
- maxalb (α_{sn}): Upper bound on maximum albedo over deep snow [%],
- laimin (LAI_{mn}): Minimum leaf area index through the year (tty) [dimensionless],
- laimax (LAI_{mx}): Maximum leaf area index tty [dimensionless],
- emissmin (ϵ_{mn}): Minimum background emissivity tty [fraction 0.0 to 1.0],
- emissmax (ϵ_{mx}): Maximum background emissivity tty [fraction 0.0 to 1.0],
- albedomin (α_{mn}): Minimum background albedo tty [fraction 0.0 to 1.0],
- albedomax (α_{mx}): Maximum background albedo tty [fraction 0.0 to 1.0],
- z0min ($Z0_{mn}$): Minimum background roughness length tty [m],
- z0max ($Z0_{mx}$): Maximum background roughness length tty [m],

where each property is called keeping the name used by the model, with the notation used on this work indicated in parentheses and the units indicated in brackets. The lookup table for USGS and IGBP land cover categories are showed in Table A.1 and A.2 respectively.

Land cover type	GVF	i	rs	rgl	hs	$snup$	α_{sn}	LAI_{mn}	LAI_{mx}	ϵ_{mn}	ϵ_{mx}	α_{mn}	α_{mx}	$Z0_{mn}$	$Z0_{mx}$
1-Urban/built-up land	0.10	1	200	999	999.00	0.040	46	1.00	1.00	0.880	0.880	0.15	0.15	0.50	0.50
2-Dryland cropland/pasture	0.80	3	40	100	36.25	0.040	66	1.56	5.68	0.920	0.985	0.17	0.23	0.05	0.15
3-Irrigated cropland/pasture	0.80	3	40	100	36.25	0.040	66	1.56	5.68	0.930	0.985	0.20	0.25	0.02	0.10
4-Mixed dryland/irrigated cropland/pasture	0.80	3	40	100	36.25	0.040	66	1.00	4.50	0.920	0.985	0.18	0.23	0.05	0.15
5-Cropland/grassland mosaic	0.80	3	40	100	36.25	0.040	68	2.29	4.29	0.920	0.980	0.18	0.23	0.05	0.14
6-Cropland/w oodland mosaic	0.80	3	70	65	44.14	0.040	60	2.00	4.00	0.930	0.985	0.16	0.20	0.20	0.20
7-Grassland	0.80	3	40	100	36.35	0.040	70	0.52	2.90	0.920	0.960	0.19	0.23	0.10	0.12
8-Shrubland	0.70	3	300	100	42.00	0.030	60	0.50	3.66	0.930	0.930	0.25	0.30	0.01	0.05
9-Mixed shrubland/grassland	0.70	3	170	100	39.18	0.035	65	0.60	2.60	0.930	0.950	0.22	0.30	0.01	0.06
10-Savanna	0.50	3	70	65	54.53	0.040	50	0.50	3.66	0.920	0.920	0.20	0.20	0.15	0.15
11-Deciduous broadleaf forest	0.80	4	100	30	54.53	0.080	58	1.85	3.31	0.930	0.930	0.16	0.17	0.50	0.50
12-Deciduous needleleaf forest	0.70	4	150	30	47.35	0.080	54	1.00	5.16	0.930	0.940	0.14	0.15	0.50	0.50
13-Evergreen broadleaf forest	0.95	4	150	30	41.69	0.080	35	3.08	6.48	0.950	0.950	0.12	0.12	0.50	0.50
14-Evergreen needleleaf forest	0.70	4	125	30	47.35	0.080	52	5.00	6.40	0.950	0.950	0.12	0.12	0.50	0.50
15-Mixed forest	0.80	4	125	30	51.93	0.080	53	2.80	5.50	0.930	0.970	0.17	0.25	0.20	0.50
16-Water bodies	0.00	0	100	30	51.75	0.010	70	0.01	0.01	0.980	0.980	0.08	0.08	0.00	0.00
17-Herbaceous wetland	0.60	2	40	100	60.00	0.010	68	1.50	5.65	0.950	0.950	0.14	0.14	0.20	0.20
18-Wooded wetland	0.60	2	100	30	51.93	0.020	50	2.00	5.80	0.950	0.950	0.14	0.14	0.40	0.40
19-Barren/sparsely vegetated	0.01	1	999	999	999.00	0.020	75	0.10	0.75	0.900	0.900	0.38	0.38	0.01	0.01
20-Herbaceous tundra	0.60	3	150	100	42.00	0.025	68	0.41	3.35	0.920	0.920	0.15	0.20	0.10	0.10
21-Wooded tundra	0.60	3	150	100	42.00	0.025	55	0.41	3.35	0.930	0.930	0.15	0.20	0.30	0.30
22-Mixed tundra	0.60	3	150	100	42.00	0.025	60	0.41	3.35	0.920	0.920	0.15	0.20	0.15	0.15
23-Bare ground tundra	0.30	2	200	100	42.00	0.020	75	0.41	3.35	0.900	0.900	0.25	0.25	0.05	0.10
24-Snow/ice	0.00	1	999	999	999.00	0.020	82	0.01	0.01	0.950	0.950	0.55	0.70	0.00	0.00
25-Playa	0.50	1	40	100	36.25	0.020	75	0.01	0.010	0.890	0.890	0.30	0.30	0.01	0.01
26-Lava	0.00	0	999	999	999.00	0.020	75	0.01	0.01	0.880	0.880	0.16	0.16	0.15	0.15
27-White sand	0.00	0	999	999	999.00	0.020	75	0.01	0.01	0.830	0.830	0.60	0.60	0.01	0.01

Table A.1: Biophysical properties for land cover types based on USGS classification.

Land cover type	GVF	i	rs	rgl	hs	$snup$	α_{sn}	LAI_{mn}	LAI_{mx}	ϵ_{mn}	ϵ_{mx}	α_{mn}	α_{mx}	$Z0_{mn}$	$Z0_{mx}$
1-Evergreen needleleaf forest	0.70	4	125	30	47.35	0.080	52	5.00	6.40	0.950	0.950	0.12	0.12	0.50	0.50
2-Evergreen broadleaf forest	0.95	4	150	30	41.69	0.080	35	3.08	6.48	0.950	0.950	0.12	0.12	0.50	0.50
3-Deciduous needleleaf forest	0.70	4	150	30	47.35	0.080	54	1.00	5.16	0.930	0.940	0.14	0.15	0.50	0.50
4-Deciduous broadleaf forest	0.80	4	100	30	54.53	0.080	58	1.85	3.31	0.930	0.930	0.16	0.17	0.50	0.50
5-Mixed forest	0.80	4	125	30	51.93	0.080	53	2.80	5.50	0.930	0.970	0.17	0.25	0.20	0.50
6-Closed shrublands	0.70	3	300	100	42.00	0.030	60	0.50	3.66	0.930	0.930	0.25	0.30	0.01	0.05
7-Open shrublands	0.70	3	170	100	39.18	0.035	65	0.60	2.60	0.930	0.950	0.22	0.30	0.01	0.06
8-Woody savannas	0.70	3	300	100	42.00	0.030	60	0.50	3.66	0.930	0.930	0.25	0.30	0.01	0.05
9-Savannas	0.50	3	70	65	54.53	0.040	50	0.50	3.66	0.920	0.920	0.20	0.20	0.15	0.15
10-Grasslands	0.80	3	40	100	36.35	0.040	70	0.52	2.90	0.920	0.960	0.19	0.23	0.10	0.12
11-Permanent wetlands	0.60	2	70	65	55.97	0.015	59	1.75	5.72	0.950	0.950	0.14	0.14	0.30	0.30
12-Croplands	0.80	3	40	100	36.25	0.040	66	1.56	5.68	0.920	0.985	0.17	0.23	0.05	0.15
13-Urban/built-up	0.10	1	200	999	999.00	0.040	46	1.00	1.00	0.880	0.880	0.15	0.15	0.50	0.50
14-Cropland/natural vegetation mosaic	0.80	3	40	100	36.25	0.040	68	2.29	4.29	0.920	0.980	0.18	0.23	0.05	0.14
15-Snow/ice	0.00	1	999	999	999.00	0.020	82	0.01	0.01	0.950	0.950	0.55	0.70	0.00	0.00
16-Barren/sparsely vegetated	0.01	1	999	999	999.00	0.020	75	0.10	0.75	0.900	0.900	0.38	0.38	0.01	0.01
17-Water bodies	0.00	0	100	30	51.75	0.010	70	0.01	0.01	0.980	0.980	0.08	0.08	0.00	0.00
18-Wooded tundra	0.60	3	150	100	42.00	0.025	55	0.41	3.35	0.930	0.930	0.15	0.20	0.30	0.30
19-Mixed tundra	0.60	3	150	100	42.00	0.025	60	0.41	3.35	0.920	0.920	0.15	0.20	0.15	0.15
20-Barren tundra	0.30	2	200	100	42.00	0.020	75	0.41	3.35	0.900	0.900	0.25	0.25	0.05	0.10

Table A.2: Biophysical properties for land cover types based on IGBP classification.

Appendix B | Computation of the EFTs biophysical properties

Once the EFT categories are defined, the computation of their corresponding biophysical properties is done following these steps:

1. Each 0.05° MODIS pixel in the MCD12C1 product comes with the percentage coverage of IGBP land-cover classes for each year.

2. The MODIS land-cover classes were then used to specify 15 land surface parameters (as defined by a Table in the Noah LSM) for each pixel and each year. These parameters are fixed for each land-cover class. For each 0.05° MODIS pixel, we calculated a 15 weighted average value (one for each land surface parameter) based on the percentage coverage of each IGBP class.

3. Each MODIS pixel was also assigned a particular EFT category (from 1-64) for each year. The 64 annual EFT categories were computed from the monthly NDVI values of the MOD13C12 product (Alcaraz-Segura et al., 2013a).

4. The annual EFT maps were then overlaid on top of each of the 15 land surface parameter maps of the corresponding year (from step 2). Then, for each EFT category, a spatially averaged parameter value was computed. This means that we have now for each year a table with a set of 15 biophysical parameters per EFT category.

5. Finally, the 2001-2009 time mean of each land surface parameter was computed for each EFT category. With this step we get a unique relation between EFT categories and their biophysical parameters that allows to prepare a unique table similar to the one used in Noah LSM (EFT category values for 15 parameters).

Appendix C | Examples of the Monitoring and Forecasts System

The routine forecasts and monitoring for agricultural and hydrological applications is compound of two modules: monitoring and forecasts. All tools in each module are offered for both domains: South America and LPB. The variables can vary depending the type of product. A control panel to select these and others options is available for each module (see right side in Figures C.1 to C.5). Figures from C.1 to C.5 show an example of each item.

The example figures are captures of the system on October 15th, 2014, and will be used to briefly explain how the tools offered in the system can be interpreted. According to the model, the last 30-days had high precipitation over the Andes in San Juan, Mendoza, Neuquén, but also in San Luis and La Pampa (Figure C.1). Particularly inside LPB, the Lower LPB presented normal to wet conditions, while the Upper LPB had almost not precipitation. Focusing in Mid-Upper Paraná with the Figure C.2, it can be seen that there was several precipitation events in the first half of the period, and then there was no precipitation event. The lack of precipitation and the high evapotranspiration in last 15 days dried the soil and nullified the runoff.

On the other hand, forecasts tools shows that is expected that the anomaly conditions monitored in last month can be even more severe inside LPB. The 7-days average map (Figure C.4) presents still more rain in Lower LPB, and no rain over Upper LPB. Then, is expected an increase of wet anomalies over Lower LPB, mainly over Uruguay sub-basin and a strengthening of dry conditions over Upper LPB. In turn, the 7-days map shows high precipitation events eastern Argentina that extends to Uruguay. The most severe events are expected for the second, third and fourth day of forecasts (i.e. November 16th to 18th, 2014) as showed in Figure C.3 for the second day. It is also seen in the meteogram over Concordia (Argentina) (Figure C.5), where precipitation concentrates on mentioned dates. Also, the meteogram shows the increase of soil moisture for each rain event, and a general increase of runoff. Once the storms end, the daily maximum and minimum temperature drop by more than 5 $^{\circ}C$. Note how the wind direction rotates from north to south as the storm progresses. A complete analysis of the storm evolution could be done using the forecasts animation for precipitation, temperature and winds (3-hr maps).

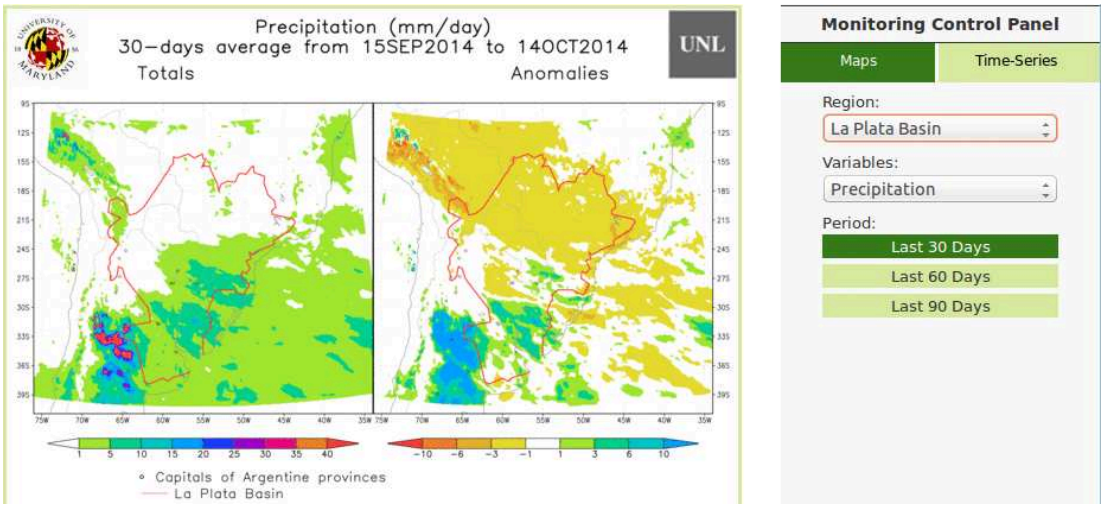

Figure C.1: 30-days precipitation monitoring for LPB domain.

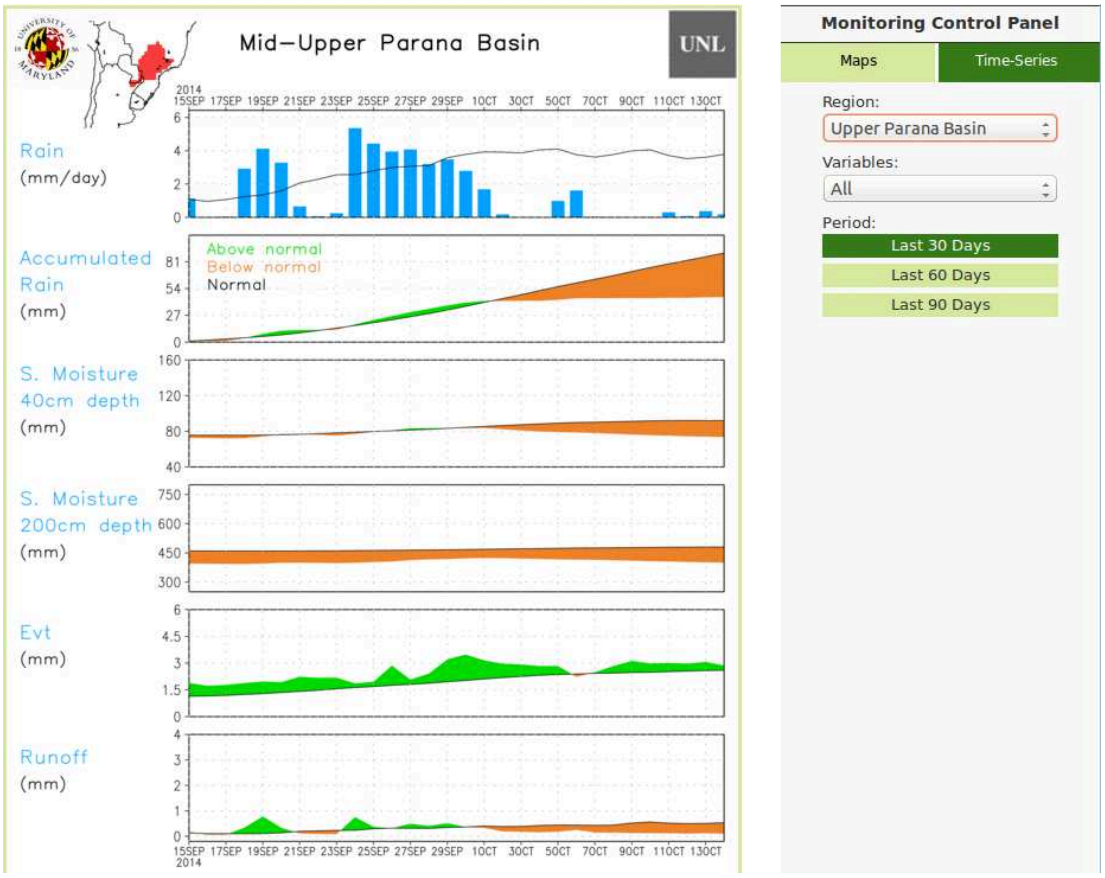

Figure C.2: 30-days hydrological variables monitoring for Mid-Upper Paraná sub-basin.

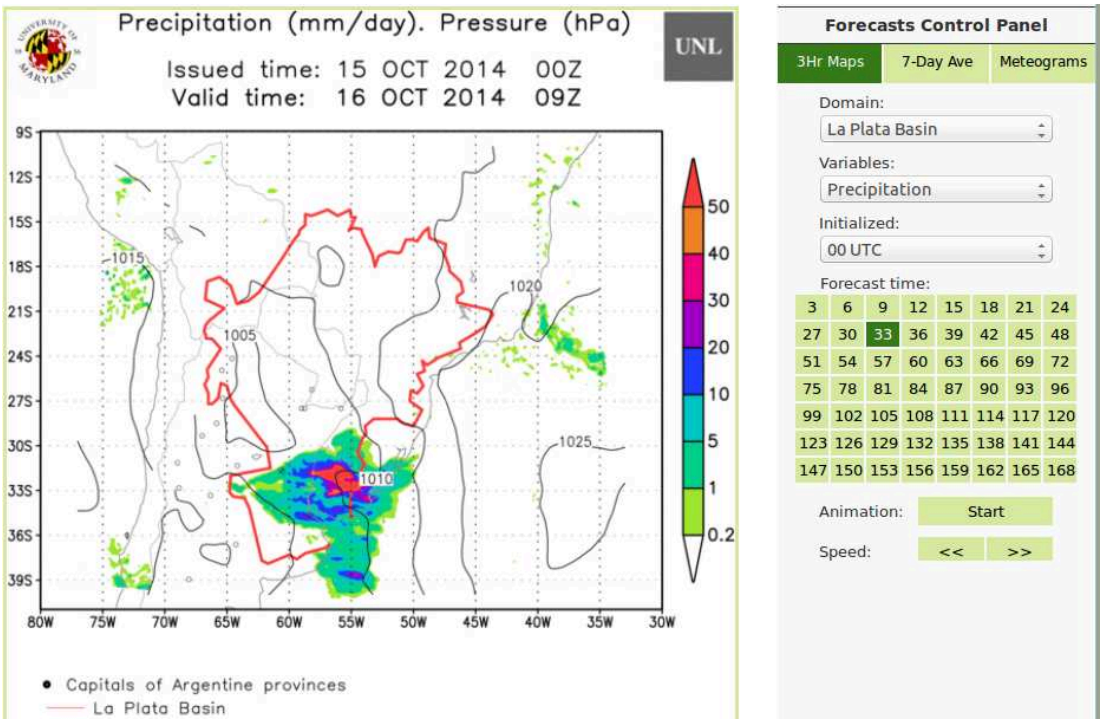

Figure C.3: One time-step map (33-hr) of the precipitation animation for the 168-hr forecasts in LPB.

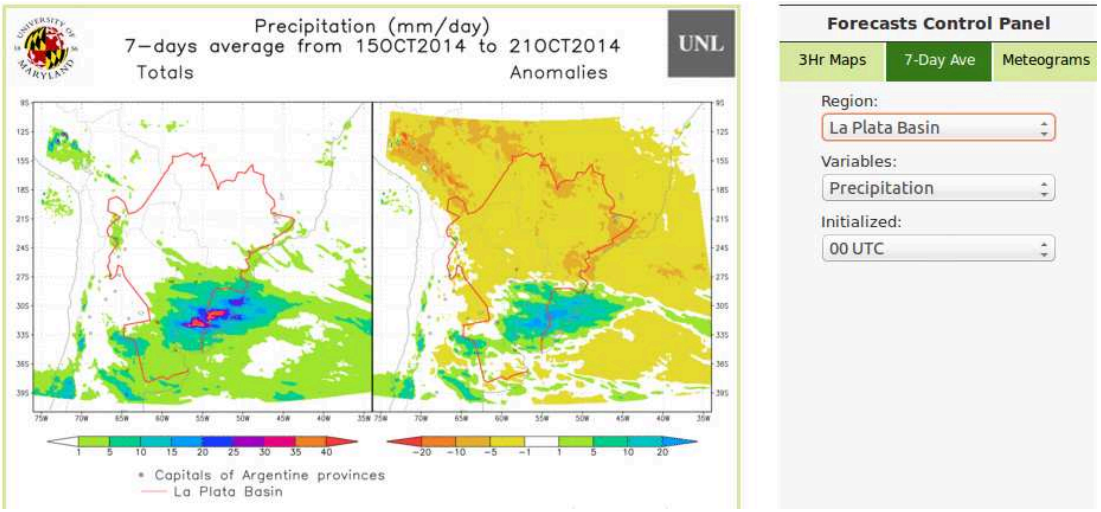

Figure C.4: 7-days precipitation forecasts for LPB domain.

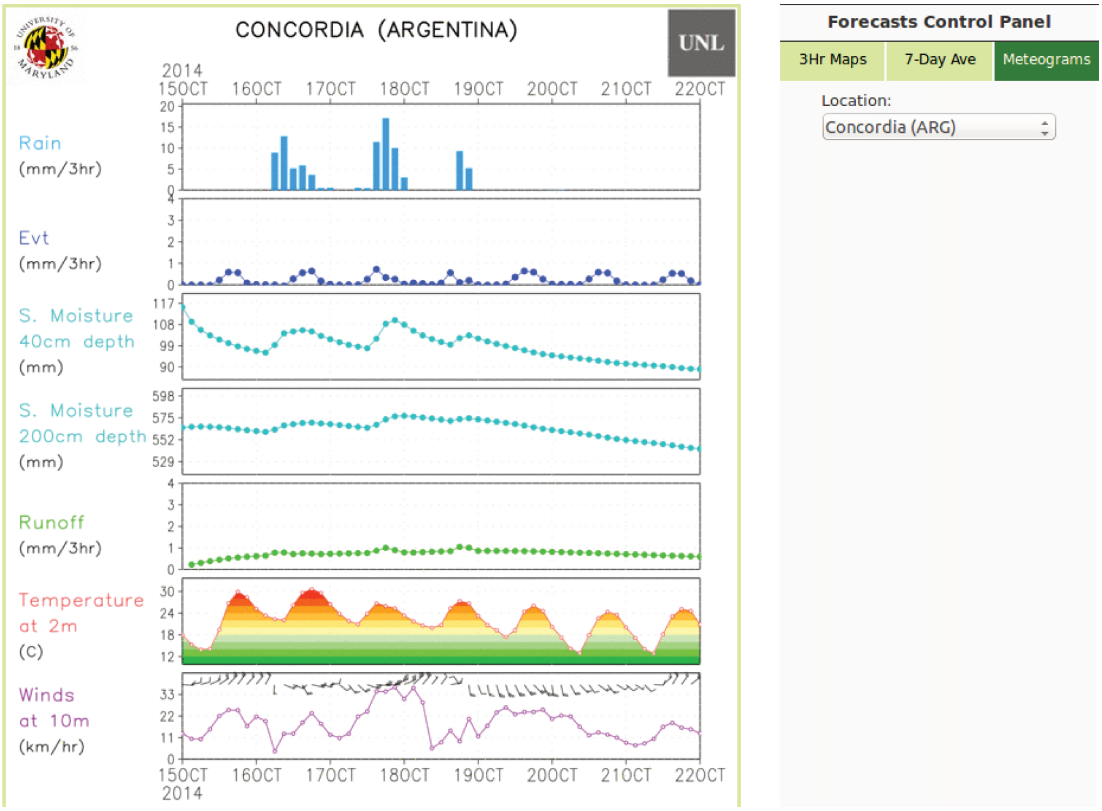

Figure C.5: Meteogram for the forecasts in Concordia (Argentina).

Appendix D | Resumen extendido en español

Pronósticos hidrometeorológicos y su sensibilidad a los cambios de uso del suelo

D.1 Introducción

El clima de Sudamérica se caracteriza por una gran variabilidad a diferentes escalas temporales y espaciales. En la actualidad, las anomalías de temperatura superficial de los océanos son reconocidas como el factor de mayor influencia en la ocurrencia de eventos extremos en el sur de Sudamérica. No obstante, las condiciones de la superficie del suelo actúan como moduladores de períodos anómalos persistentes, ya sea secos o húmedos, a través de las interacciones suelo-atmósfera. Por lo tanto, resulta esencial avanzar sobre nuevos enfoques que contribuyan en la comprensión de estas interacciones.

En Sudamérica, ademas de la región Amazónica, la cobertura superficial ha experimentado grandes cambios en las últimas décadas en el sur de Sudamérica, ya sea inducidos por el hombre o de origen natural. Estos cambios de cobertura tienen un impacto directo en los procesos de superficie, y son reconocidos como fuente potencial de variabilidad y predictibilidad climática. Mientras la interacción océano-atmósfera ha sido estudiada en profundidad y es correctamente representada por los modelos regionales, la representación de la relación suelo-atmósfera aún presenta dificultades para los modelos, especialmente en la región de interés.

Muchos de los modelos atmosféricos actuales usan esquemas simplificados de superficie del suelo. Por ejemplo, representan la vegetación con mapas de cobertura del suelo fijos en el tiempo junto con tablas que definen propiedades biofísicas para cada tipo de cobertura. Este tipo de representación no considera los cambios interanuales de las propiedades debido a exceso o déficit de precipitación, cambio de uso del suelo, cambio de cobertura, etc. Esta limitación puede por ejemplo, retardar el impacto del estado del suelo sobre variables at-

mosféricas, y por ende, reducir la habilidad de los modelos para representar cambios rápidos que afecten la predictibilidad de inundaciones, o sequías.

Diferentes trabajos han demostrado que una correcta representación de la cobertura del suelo contribuye a mejorar la predictibilidad de las interacciones suelo-atmósfera (Betts et al., 1996; Smith et al., 2001; Kurkowski et al., 2003; Levis et al., 2004; Tian et al., 2004a,b; Ge et al., 2007; Jiang et al., 2010; Weiss et al., 2012). A pesar de estas evidencias, los modelos actuales, particularmente los utilizados para pronósticos operativos, aún utilizan tipos de cobertura del suelo fijos en el tiempo. Es decir, son incapaces de representar las fuentes adicionales de variabilidad interanual debido a los cambios de cobertura.

La hipótesis de este trabajo es que una representación realista de la cobertura del suelo y sus propiedades contribuye en la mejora de la simulación de interacciones suelo-atmósfera y por lo tanto, puede reducir desvíos del modelo inherentes a procesos de superficie. Este trabajo se propone, desarrollar y explorar el uso de un conjunto consistente de propiedades biofísicas variantes en el tiempo y derivadas de datos de satélite en reemplazo de los tipos de cobertura del suelo que se usan convencionalmente en el modelo Weather Research and Forecasting (WRF) acoplado al modelo de superficie Noah (Noah LSM).

El nuevo enfoque basado en el concepto de ecosistemas funcionales se denomina Tipos Funcionales de Ecosistemas (EFTs, del inglés Ecosyste Functional Types). Este enfoque tiene en cuenta las propiedades funcionales de los ecosistemas terrestres, mas allá del tipo de cobertura. Las propiedades son identificadas a partir de mediciones de satélite del índice verde normalizado (NDVI, del inglés Normalized Difference Vegetation Index) derivado del satélite MODIS (del inglés, Moderate Resolution Imaging Spectroradiometer). La hipótesis se pone a prueba durante una sequía prolongada que tuvo lugar en el sudeste de Sudamérica durante el año 2008.

D.1.1 Objetivos

En relación a los temas planteados, los principales objetivos de este trabajo son:

- Investigar las fortalezas y debilidades actuales del modelo regional para representar el clima regional de la cuenca del Plata.
- Profundizar el conocimiento de los procesos que conducen a mejoras en la predictibilidad del clima regional, específicamente utilizando un conjunto de propiedades biofísicas mas realista y consistente en el modelo regional.
- Mejorar la comprensión del impacto de cambios de cobertura y uso del suelo sobre procesos físicos relacionados al hidroclima de la cuenca del Plata.

- Desarrollar capacidades predictivas implementando un sistema de pronósticos y monitoreo en tiempo real que genere información práctica para diferentes usuarios, particularmente de sectores agrícolas e hidrológicos.

D.2 Modelos regionales y acoplados: Representación de la superficie del suelo

D.2.1 Introducción a modelos regionales acoplados

Los modelos de circulación general (GCM, del inglés Global Climate Models) actuales simulan el comportamiento del sistema climático acoplando tres subsistemas principales: atmósfera, suelo y océanos, que se relacionan mediante flujos de calor, humedad y momento. Los GSMs permiten simular circulaciones generales, pero fallan en la predicción de procesos a escala regional. Esta limitación se resuelve mediante modelación anidada, utilizando modelos regionales (RCM, del inglés Regional Climate Models). Los RCMs se nutren de los GCM para definir las condiciones iniciales y de borde y logran un análisis detallado de las condiciones locales a partir de una mejor resolución y parametrización.

Las ecuaciones de gobierno que representan el comportamiento atmosférico en modelos climáticos (RCMs y GCMs) se denominan ecuaciones primitivas. Son un sistema de siete ecuaciones diferenciales no-lineales con siete incógnitas y con condiciones de borde definidas. La formulación de este sistema se encuentra en numerosos libros de dinámica de la atmósfera (Peixoto and Oort, 1992; Hartmann, 1994; Rayner, 2001; Holton et al., 2004; Jacobson, 2005) y está formado por la ecuación de movimiento, la ecuación de continuidad, la ecuación de estado para aire húmedo, la ecuación de termodinámica (primera ley) y la ecuación de conservación del vapor de agua. En este sistema las incógnitas están dadas por la velocidad en sus tres dimensiones (zonal, meridional y vertical), la densidad del aire, la presión, la temperatura y la humedad específica del vapor de agua.

Para este trabajo se utilizó el modelo regional WRF. Este modelo es de desarrollo cooperativo entre múltiples instituciones, encabezadas por el National Center for Atmospheric Research (NCAR). El desarrollo colaborativo lo ha convertido en el mas utilizado a nivel mundial. WRF es un modelo de mesoescala utilizado tanto de manera operacional como para diagnóstico, asimilación de datos, investigación sobre parametrizaciones, simulaciones sintéticas, etc.

El uso de un modelo no sólo implica la elección de un dominio y resoluciones espaciales y temporales. También se requiere de la definición de numerosas parametrizaciones relacionadas a la dinámico y principalmente a la física del

mismo. WRF ofrece para cada parametrización múltiples opciones, desde simples y eficientes hasta complejas y costosas computacionalmente, como también desde esquemas novedosos a tradicionales. Entre las parametrizaciones mas relevantes para los procesos de superficie se encuentran: los esquemas que definen la microfísica, los esquemas de convección cúmulus, los esquemas de capa de superficie, el modelo de superficie del suelo, los esquemas de capa límite planetaria y los esquemas de radiación atmosférica.

Aunque las parametrizaciones mencionadas se definen individualmente, existen muchas interacciones entre ellas. Particularmente, las propiedades biofísicas asociadas a la cobertura del suelo están directa o indirectamente involucradas en muchas de las parametrizaciones. Estas propiedades son definidas por el modelo de superficie y afectan directamente la capa de superficie y la radiación atmosférica. Los flujos de calor y humedad también dependen de las propiedades biofísicas, por lo tanto, la capa límite planetaria y la convección también están indirectamente relacionadas a las mismas.

D.2.2 Representación de la vegetación en el modelo de superficie

El modelo Noah es elegido para representar la superficie del suelo. Este modelo de superficie de complejidad intermedia ofrece una relación costo/beneficio que los posiciona como la mejor opción para pronósticos operacionales. Noah utiliza forzantes atmosféricos y de radiación, junto con información interna de variables de estado del suelo y propiedades de superficie, para proveer flujos de calor y humedad sobre puntos superficiales. Estos flujos proveen a su vez una condición de borde inferior para el transporte vertical calculado en la capa límite planetaria. Por otro lado, define cuatro capaz de 10, 30, 60 y 100 cm de espesor (2 m de profundidad total), e incluye la zona de raíces, las categorías de vegetación o cobertura, fracción de vegetación mensual, textura del suelo, entre otros. A su vez Noah LSM predice nieve en el suelo, y efectos de cobertura de nieve, tiene un tratamiento mejorado de zonas urbanas y considera las propiedades de emisividad de superficie. También simula la humedad y la temperatura del suelo, la temperatura superficial, el espesor y la densidad de la capa de nieve, el contenido de agua en el canopeo, y términos de flujo de agua y energía en sus respectivos balances superficiales.

Las ecuaciones del modelo Noah LSM se pueden dividir en tres partes: termodinámica, hidrología y nieve. La termodinámica determina el balance superficial de energía representando la superficie combinada suelo-vegetación. La hidrología define el contenido volumétrico de humedad del suelo mediante el balance de agua en cada capa del modelo. En este balance resultan importantes propiedades biofísicas tales como la profundidad de las raíces, la re-

sistencia estomatal y el índice de área foliar. El modelo de nieve tiene una capa de cobertura de nieve y simula su acumulación, sublimación, derretimiento e intercambio de calor en sus interfaces. Aquí se destaca la importancia de propiedades como el albedo o la emisividad. Como se deduce, las propiedades biofísicas definidas por el tipo de cobertura son críticas para el modelo de superficie. Luego, una definición realista de estos parámetros biofísicos puede ayudar a mejorar la calidad del modelo de superficie y por ende los resultados generales de la simulación.

El modelo Noah LSM prescribe un tipo de cobertura del suelo y sus propiedades asociadas para cada punto de grilla. Así, cada punto de grilla tiene definido una categoría de vegetación o cobertura constante en el tiempo. Luego, un conjunto de 15 propiedades son asignadas mediante una tabla con valores predefinidos por categoría. Por defecto el modelo usa un conjunto de 27 coberturas generadas por el United States Geological Survey (USGS) Center. El mapa con estas categorías se derivó de imágenes del satélite AVHRR (del inglés, Advanced Very High Resolution Radiometer), capturadas diariamente durante un período de 12 meses de Abril de 1992 a Marzo de 1993 con una resolución de 1 km. Alternativamente, el modelo ofrece otra clasificación de 20 categorías definidas por el International Geosphere Biosphere Program (IGBP). Esta clasificación se basa en datos del satélite MODIS capturadas de Octubre del 2000 a Octubre del 2001.

Las 15 propiedades biofísicas son: fracción de vegetación verde, profundidad de las raíces, resistencia estomatal, parámetro utilizado en la función de estrés de radiación, parámetro utilizado en la función de déficit de presión de vapor, umbral de equivalencia agua-profundidad de nieve, límite superior de albedo máximo sobre nieve, mínimo y máximo índice de área foliar durante el año, mínimo y máximo emisividad durante el año, mínimo y máximo albedo durante el año, mínimo y máxima altura de rugosidad durante el año. Una vez que se elige la clasificación (USGS o IGBP), las categorías y los valores de las propiedades se mantienen constantes durante la simulación.

El enfoque de definición de coberturas convencional tiene varias limitaciones a partir de su invariancia temporal y a valores mínimos y máximos prefijados. Por ejemplo, se asume que cada cobertura tiene las mismas propiedades constantes durante una sequía o un período húmedo, y en cualquier locación clasificada con la misma categoría. Los intercambios de energía, agua, y momento entre suelo y atmósfera dependen de las propiedades. Consecuentemente, cambios en el tipo de cobertura también afectarán esos intercambios con posibles impactos en las condiciones del clima. La inclusión de información de cobertura mas realista en modelos de superficie es relativamente nueva, pero particularmente relevante para el sur de Sudamérica, donde el reemplazo de vegetación nativa por cultivos principalmente ha ocurrido extensivamente en

los últimos años.

D.2.3 Tipos funcionales de ecosistemas

Para superar las limitaciones planteadas anteriormente, esta investigación explora la sensibilidad del modelo al uso de ecosistemas variantes en el tiempo como reemplazo a las coberturas fijas. Los atributos funcionales de los ecosistemas, aquellos que caracterizan el intercambio de energía y materia entre la biota y la atmósfera, muestran una respuesta mas rápida a cambios ambientales que aquellos estructurales. Además, son relativamente fácil de monitorear utilizando índices espectrales derivados de mediciones satelitales. Basado en este concepto, Alcaraz et al. (2006); Alcaraz-Segura et al. (2013a) desarrollaron un método para definir Tipos Funcionales de Ecosistemas en base anual. Formalmente, los EFTs se definen como grupos de ecosistemas que comparten características funcionales en relación a la cantidad y tiempo de intercambio de materia y energía entre la biota y el ambiente físico que lo rodea (Paruelo et al., 2001; Alcaraz et al., 2006). Dado que son definidos a partir de descriptores del ciclo anual de NDVI, la variabilidad interanual de las condiciones de superficie puede ser identificada.

Los EFTs son computados a partir de tres métricas del ciclo anual de NDVI: (a) NDVI-I: el valor medio anual de NDVI como estimador de producción primaria neta; (b) CV: el coeficiente de variación estacional de NDVI como descriptor de la estacionalidad (amplitud del ciclo anual); y (c) DMAX: la fecha del máximo absoluto de NDVI en el año dado como indicador fenológico de la estación de crecimiento. Por razones prácticas el rango de valores para cada descriptor es dividido en cuatro intérvalos fijos, dando un número potencial de $4^3 = 64$ categorías. Para dividir NDVI-I en cuatro categorías, se obtienen tres cuartiles para cada año y luego, para cada cuartil, se calcula la mediana en el período de años base. Lo mismo aplica para CV. Por último, las cuatro categorías para DMAX se corresponden a las cuatro estaciones del año para ecosistemas templados.

Las categorías de EFTs son identificadas con códigos de tres caracteres, uno para cada descriptor. La definición y codificación de los EFTs permiten una interpretación ecológica de la leyenda en término de las métricas de NDVI: el primer caracter identifica la productividad primaria neta de menor a mayor con letra mayúscula de A a D (productividad creciente). El segundo caracter representa la estacionalidad de mayor a menor (amplitud del ciclo anual), la cual se identifica por letra minúscula de a a d (estacionalidad decreciente). El último caracter corresponde a la estación del máximo NDVI, donde primavera se identifica con 1 y secuencialmente se asigna un número a las estaciones siguientes. Así, por ejemplo, las plantaciones de soja en el Chaco seco tienen

relativamente baja productividad, gran estacionalidad y máximo en verano, lo que se corresponde con el EFT Ba2.

El modelo Noah define una tabla con 15 propiedades biofísicas para cada tipo de cobertura. De manera análoga, el método propuesto define las 15 propiedades para cada EFT y cada año haciendo:

1. Cada píxel MODIS del producto MCD12C1 viene con el porcentaje de cada tipo de cobertura dentro del píxel, según las categorías de IGBP para cada año.

2. Luego,las coberturas de MODIS son usadas para especificar los 15 parámetros para cada píxel y cada año. Estos parámetros son fijos para cada tipo de cobertura. Para cada píxel, se calculan 15 promedios pesados (uno por cada parámetro) basados en el porcentaje de cobertura de cada clase IGBP.

3. A cada píxel MODIS se le asigna una categoría particular de EFT (de 1 a 64) para cada año. Estas EFTs anuales son calculadas con valores mensuales de NDVI del producto MOD13C12.

4. Los mapas anuales de EFT son superpuestos sobre el mapa de cada uno de los 15 parámetros decada año (definidos en el paso 2). Luego, para cada categoría EFT, se calcula un promedio espacial de cada parámetro. A partir de aquí, se tiene una tabla de propiedades para cada año.

5. Finalmente, se promedia en el tiempo cada parámetro para cada categoría EFT. Aquí se tiene una única tabla que define las propiedades de cada EFT y un mapa de EFT por año.

Con el objetivo de hacer una primera evaluación del enfoque propuesto, se contrastaron valores de albedo mínimo y máximo de diferentes fuentes y para diferentes locaciones. Dichas locaciones son definidas como cultivos (en dos casos), pasturas y sabana según IGBP. Las estimaciones de albedo comparadas son:

a)	MODIS	albedo de onda corta del producto MCD43C3, utilizado como referencia;
b)	IGBP LC-derivado	albedo definido por tabla de Noah LSM;
c)	MODIS LC-derivado	valor de tabla derivado de mapas de cobertura variantes en el tiempo de MODIS producto MCD12C1; y
d)	EFTs-derivado	derivado en este estudio.

Los albedos provenientes de diferentes enfoques fueron contrastados mediante gráficos de dispersión y series de tiempo. Los resultados muestran que en

todos los casos el albedo derivado de este estudio tiende a corresponderse mejor con las observaciones que el resto de las estimaciones. A su vez, los resultados demuestran que mientras los métodos convencionales mantienen constantes los valores de albedo, el nuevo enfoque muestra variaciones interanuales tal como lo hacen los valores observados. También se observa que en general el albedo tiene correlación negativa con NDVI.

Parte de la mejora puede ser atribuida al hecho de que los métodos convencionales prescriben propiedades para cada tipo de cobertura sin considerar si es un año húmedo o seco y si existió un cambio de cobertura. El enfoque de EFT se basa en estimaciones satelitales de intercambios de masa y energía entre suelo y atmósfera, mas allá del tipo de cobertura. Luego, las propiedades biofísicas resultan sensibles debido a años secos o húmedos, incluso cuando se asuma que el tipo de cobertura es el mismo.

D.2.4 Discusión: Métodos de representación de cobertura

Como se notó previamente, una de las limitaciones de las clasificaciones convencionales (USGS o IGBP) es que son constantes en el tiempo. El uso de coberturas de MODIS en base anual es una mejora importante en ese sentido. A pesar de eso, la definición de coberturas puede incluir errores importantes por escasez o falta de información in-situ, como puede suceder en la región de interés. MODIS también estima para cada año alguna de las 15 propiedades biofísicas que podrían ser incluidos en modelos de superficie. Sin embargo, el resto de las propiedades también deberían cambiar consistentemente con las propiedades modificadas.

En este trabajo, todas las propiedades biofísicas son derivadas de los valores de EFT con el objetivo de mantener la consistencia entre ellas y evitar la mezcla de enfoques. En este sentido, el método modifica todas las propiedades a partir de un único indicador físico (el valor de EFT). En cualquier caso, el objetivo de este estudio no es una comparación con las estimaciones de MODIS, sino mas bien mostrar posibles mejoras sobre la versión actual del modelo WRF/Noah.

Notar que con los enfoques convencionales también es posible incrementar el número de tipos de coberturas para representar mejor cambios como el del tipo de cultivo. Sin embargo, asignar propiedades físicas a cada subcategoría puede ser difícil de lograr. En este caso, las propiedades EFT son derivadas de un número reducido de tipos de cobertura, que se realiza como promedio pesado para cada píxel. Per se, esto no provee información adicional, sin embargo, las EFTs incluyen en su definición una representación del estado de la vegetación mediante el indicador de producción primaria, la amplitud anual, y la fenología derivadas del ciclo anual de NDVI. Ecologicamente, esta información es significativa y de otro modo no se tiene en cuenta. La definición

de EFTs captura las diferencias en términos de ecosistemas funcionales dentro del mismo tipo de cobertura. Por ejemplo, logra distinguir entre matorrales abiertos y densos, o cultivos irrigados o de secano. Esto se logra mediante las diferencias que surgen en la dinámica de la producción primaria. Con estas definiciones, cambios anuales en EFTs tendrán asociadas un conjunto anual de propiedades biofísicas consistente (por ej., un año seco con vegetación estresada tendrá un incremento de resistencia estomatal, mayor albedo y menor rugosidad de superficie).

Resumiendo, los aspectos principales de la clasificación EFTs son: (a) es un enfoque alternativo a la clasificación por tipo de cobertura que hace énfasis en la homogeneidad de propiedades físicas en términos de intercambios de energía y biomasa entre suelo y atmósfera. Desde el punto de vista de la modelación climática, esto es único; (b) el enfoque se basa en el concepto de ecosistema funcional, intercambio de energía y carbono; (c) se puede aplicar a casos previos a MODIS (utilizando NDVI de AVHRR); y (d) provee consistencia entre 15 propiedades biofísicas diferentes.

D.3 Climatología de la cuenca del Plata a partir de una simulación de alta resolución

En esta sección se hace un análisis de una simulación de 11 años sobre la cuenca del Plata. La meta final es obtener una climatología confiable de alta resolución que permita computar anomalías en otros experimentos. Para ello es necesario evaluar las fortalezas y debilidades actuales del modelo en la región. El análisis se basa en la descripción de desvíos respecto a observaciones para variables seleccionadas y también un análisis de eventos extremos.

El rendimiento del modelo se evalúa en términos de precipitación, humedad del suelo y temperatura. Todas ellas son consideradas variables climáticas esenciales por la Organización Mundial de Meteorología (WMO, del inglés World Meteorological Organization), y requieren la correcta representación de muchos procesos para simularlas.

D.3.1 Configuración del modelo y datos

La simulación fue realizada con el modelo WRF versión 3.3 acoplado al modelo Noah LSM. El período de simulación comienza el 1 de Enero del 2000 y se extiende hasta el 31 de Diciembre de 2010. Sin embargo, el año 2000 es considerado período de estabilización del modelo y sus resultados son descartados en el análisis.

El dominio cubre Sudamérica con una resolución de 45 km con un dominio

anidado cubriendo la cuenca del Plata con una resolución de 15 km. El dominio mayor tiene la mayoría de sus bordes sobre los océanos, asegurando la contribución de las temperaturas del océano a través de las condiciones de borde laterales. En el dominio anidado, las condiciones de borde laterales son proveídas por el dominio padre. El dominio anidado incluye la cuenca del Plata, conformada por cuatro sub-cuencas: Paraguay, Medio y Alto Paraná, Bajo Paraná y Uruguay. También cuenta con importantes características topográficas como la cordillera de Los Andes al oeste, algunas montañas de menor altura en Brasil (hacia el noreste del dominio) y planicies que completan el dominio.

La configuración física del modelo sigue la selección de esquemas y opciones de (Lee and Berbery, 2012) y (Lee, 2010) quienes evaluaron la combinación de parametrizaciones que minimizan el error en la región de estudio. El modelo es forzado por condiciones iniciales y de borde (6-hs) del NCEP Climate Forecast System Reanalysis.

El modelo es evaluado con datos observados de origen satelital o de estaciones. Para evaluar precipitación se utilizó datos del CPC (del inglés, Climate Prediction Center) llamados Unified Gauge-Based Analysis of Global Daily Precipitation. Este conjunto consiste de observaciones interpoladas a una grilla de $0.5^\circ \times 0.5^\circ$. También datos derivados de satélite fueron usados, en particular los del Tropical Rainfall Measurement Mission (TRMM) 3B43 cuya resolución es de $0.25^\circ \times 0.25^\circ$. Las estimaciones de humedad del suelo se compararon contra el conjunto llamado Essential Climate Variable V2 de origen satelital. Tiene una resolución de $0.25^\circ \times 0.25^\circ$. La temperatura se evalúa con el conjunto llamado CPC Global monthly gridded land-only surface air temperature at 2 m, conocido como GHCN-CAMS. También el producto de origen satelital MOD11C3 es usado para evaluar temperatura.

D.3.2 Fortalezas y debilidades del modelo en la cuenca del Plata

Los resultados generales sugieren que la parametrización utilizada es adecuada para representar el clima regional. Los mayores errores de las variables evaluadas se producen sobre la cordillera de los Andes, donde los modelos tienden a fallar por la complejidad topográfica, la escasez de observaciones y parametrizaciones que no se ajustan a climas de regiones montañosas.

Dentro de la región de interés (cuenca del Plata), el modelo alcanza una gran similitud con la distribución espacial de precipitación e identifica correctamente la gran variación anual de precipitación en la parte norte. Sin embargo, el modelo tiende a simular condiciones mas secas que lo observado. En la parte norte de la cuenca (subcuencas de Paraguay y Medio y Alto Paraná) los desvíos secos se dan principalmente en los meses de menor precipitación (coincidente

con los meses mas fríos). En la parte sur de la cuenca el modelo subestima la precipitación durante todo el año.

Los patrones de humedad de suelo derivados de satélites y del modelo son consistentes con la distribución espacial de precipitación. Los valores mas altos se dan sobre el Bosque Atlántico del Alto Paraná y las condiciones mas secas en el Desierto de Atacama, siendo Bolivia y Perú los lugares con mayor desvío (positivo). La cuenca muestra una concordancia general entre las estimaciones observadas y simuladas, con desvíos levemente secos en la parte norte. Las correlaciones entre ambos conjuntos son mejores para estaciones húmedas/cálidas que para estaciones secas/frías. Un análisis mas profundo no resulta conveniente ya que es una variable altamente dependiente de la fuente lo que invalida una comparación directa de la magnitud de los valores.

Como sucede con precipitación y humedad de suelo, el modelo hace una buena aproximación a la distribución espacial de temperatura, pero falla sobre la Cordillera. Dentro de la cuenca, el modelo muestra temperaturas más cálidas sobre la subcuenca del Paraguay, y levemente frías sobre las subcuencas del este (Medio y Alto Paraná y Uruguay). En el Bajo Paraná se combinan desvíos positivos al noroeste con desvíos negativos al sureste.

El análisis de *SPI* muestra similitudes entre la distribución de probabilidades de ocurrencia de extremos en la cuenca derivados de precipitación observada (CPC) y de la simulación. En particular, se observan algunas dificultades en la simulación de sequías severas o extremas en la parte sur de la cuenca. Aquí el modelo no muestra tantas sequías de gran magnitud como indica el *SPI* derivado de las observaciones. Sin embargo, la probabilidad de ocurrencia de meses moderada a extremadamente húmedos es notablemente similar entre CPC y WRF.

Los resultados de *SPI* mencionados muestran una valoración sobre la capacidad del modelo en representar la frecuencia y magnitud de ocurrencia eventos extremos. Sin embargo, esos resultados no indican la correspondencia entre valores de *SPI* derivados de observaciones y los derivados de la simulación para lugares particulares. Para ello, se evaluaron las series de *SPI* en dos puntos de grilla, uno en cada parte de la cuenca. Los resultados de WRF en el punto correspondiente a la parte norte no tiene una buena correspondencia con CPC. El modelo simula menor variabilidad interanual y eventos menos intensos. Sin embargo, los resultados mejoran en el punto de la parte sur, donde el modelo logra una muy buena correspondencia entre la evolución de SPI de ambos conjuntos en las diferentes escalas de tiempo. Por ejemplo, la sequía del 2008, que es objeto de estudio en la sección siguiente, está muy bien identificada. En términos de intensidad de la sequía existen similitudes aunque el modelo muestra un evento mas seco que lo observado.

La simulación discutida en esta sección ha demostrado un muy buen rendimiento del modelo sobre la región. La parametrización utilizada resulta adecuada para representar el clima regional. El objetivo de las secciones siguientes es reducir los desvíos actuales del modelo a partir de una representación mas realista del estado de cobertura del suelo.

D.4 La sequía de 2008 en la cuenca del Plata

D.4.1 La sequía según las observaciones

La hipótesis de esta investigación es que una representación realista de las propiedades de la vegetación ayuda a mejorar la simulación de las interacciones suelo-atmósfera y por lo tanto puede reducir los desvíos del modelo inherentes a procesos de superficie. Consecuentemente, se espera que estos efectos sean mas notorios durante situaciones anómalas, cuando la vegetación mas se aleja de las condiciones predefinidas, como sucede durante una sequía. Por esta razón la hipótesis se evalúa durante la sequía de 2008 ocurrida en el sur de Sudamérica. Otras regiones cercanas tuvieron precipitación normal o por exceso, lo que da lugar a examinar las interacciones en condiciones muy diferentes.

La sequía tuvo características excepcionales en términos de extensión espacial, persistencia e intensidad, comparable o incluso mas importante que otras grandes sequías de las últimas décadas. Espacialmente tuvo su epicentro en Uruguay, extendiéndose sobre el Bajo y Medio Paraná, y la parte sur de la subcuenca del Paraguay. Según valores de *SPI* promedio para 2008, la sequía se caracterizó como moderada a severa dependiendo la región.

La intensa sequía surge como consecuencia de la acción combinada de un evento La Niña y anomalías cálidas en el Atlántico Norte Tropical. Estas anomalías produjeron un primer déficit leve de precipitación durante el invierno de 2007. Ya en Noviembre de 2007 el déficit de precipitación se combinó con temperaturas de verano levemente superiores a lo normal acentuando las condiciones adversas. Consecuentemente, se redujo gradualmente el contenido de agua en el suelo. La región afectada está dominada por cultivos y pasturas, coberturas sensibles a condiciones anómalas. Luego, las condiciones secas generalizadas condujeron a un estrés de la cobertura que se reflejó con anomalías negativas de NDVI. Estos procesos de sequía se extendieron hasta Junio de 2009, cuándo el evento La Niña ya se debilitó y las lluvias retornaron a valores normales.

Como se mencionó, las condiciones secas generalizadas condujeron a coberturas con mayor estrés reflejado en las anomalías negativas de NDVI. De acuerdo a los modelos actuales esta información no se tiene en cuenta. Sin embargo,

esto si se observa mediante los mapas de EFTs. En particular el mapa de EFTs de 2008 muestra diferencias significativas con respecto a las EFTs de 2001 a 2009 utilizadas como referencia. La comparación muestra que en lugares afectados por la sequía se pasa de vegetación con productividad y estacionalidad promedio a baja o muy baja. También se observan algunos cambios menos significativos en otras regiones. Todos los cambios en el funcionamiento de los ecosistemas concuerdan con la dinámica observada de NDVI.

D.4.2 La sequía según las simulaciones

Se hicieron simulaciones sobre el dominio de la cuenca del Plata para el período de sequía, es decir, de Setiembre 2007 a Julio 2009. Para ello se usó la misma configuración utilizada en la climatología, usando como forzantes las condiciones de borde e iniciales de NCEP/NCAR Global Reanalysis Project.

Las simulaciones se dividieron en dos ensambles. Un ensamble de control (CTL) donde se simula con el mapa de coberturas de USGS que el modelo utiliza por defecto. El otro ensamble denominado EFT utiliza el mapa de EFTs derivado de este estudio. En ambos casos cada ensamble consta de 5 miembros que desfasan en 24 hs la fecha de comienzo de la simulación. Estos ensambles fueron comparados con valores observados para demostrar la hipótesis propuesta. Notar, que las simulaciones de uno y otro ensamble comparten las misma configuración y forzantes a excepción del mapa de cobertura y las propiedades biofísicas.

El cambio de propiedades muestra en la región seca un decrecimiento en la fracción de vegetación verde y en el índice de área foliar y mayor resistencia estomatal al pasar de USGS a EFTs. A su vez, en la parte norte de la sequía, alrededor del Paraná Medio, las EFTs reducen la fracción de vegetación verde, el índice de área foliar y la rugosidad, y aumentan el albedo. Este tipo de cambios muestran las modificaciones que se hicieron en los datos de entrada al cambiar la representación de la cobertura. Luego, la evaluación consiste en estudiar los efectos de estos cambios en las variables de salida. En particular sobre precipitación y temperatura, y todas aquellas variables que pueden influir en la determinación de las mismas. Los resultados no fueron sencillos de interpretar ya que no siempre las consecuencias son directas debido a la complejidad del sistema suelo-atmósfera.

En términos de precipitación, los resultados muestran una reducción generalizada de los desvíos del modelo (tanto positivos como negativos) con la utilización de EFTs. En particular en la zona de la sequía las EFTs permitieron ajustar el desvío negativo de las simulaciones de control. Es decir, CTL presentaba una sequía mas severa de lo observado y EFT permitió corregir esta sobreestimación en un 4 %. Hacia el norte de la cuenca del Plata, donde CTL

mostró desvíos positivos de gran magnitud, EFT logra reducirlos entre un 10% y un 20 %. La reducción de los desvíos resulta mas evidente en la estación húmeda donde el desvío llega a reducirse en un 27%.

El análisis de los procesos de superficie sugiere que aquellas áreas donde ser la humedad del suelo es reducida están asociadas con reducciones de evapotranspiración, incremento del flujo de calor sensible, como así también menor precipitación y escorrentía. Por el contrario, regiones donde la humedad del suelo se incrementa están asociadas con reducciones de calor sensible, mientras se incrementa el flujo de calor latente favoreciendo una capa límite planetaria mas húmeda que conlleva a mayores precipitaciones y escurrimiento. El cálculo de correlaciones entre estas variables confirman lo establecido. La humedad del suelo tiene correlación positiva (negativa) con el flujo de calor latente (sensible). A su vez, la correlación entre el calor latente (sensible) y la precipitación es positivo (negativo). Como se mencionó, estas relaciones no son siempre directas y en algunos casos particulares los resultados se desvían de lo formulado, principalmente cuando se desarrollan circulaciones regionales resultantes de los cambios de cobertura.

Los resultados en temperatura muestran un calentamiento generalizado con EFT en comparación con CTL, posiblemente debido a la reducción de la vegetación por la sequía, aunque el reemplazo de bosques por cultivos también pudo haber contribuido. Este aumento de temperaturas permitió reducir el desvío negativo de las simulaciones de control (observadas también en la climatología) al este del dominio sobre la costa Atlántica. La reducción fue de -1.3 $^{\circ}C$ a 0.2 $^{\circ}C$. A su vez, se incrementó el desvío positivo en las subcuencas del oeste (Paraguay y Bajo Paraná) de 0.4 $^{\circ}C$ a 1.3 $^{\circ}C$. Si bien en esta región se reduce el desvío durante los meses de invierno, en el resto de los meses el desvío se incrementa.

El análisis del balance energético no arroja resultados claros. La mayoría de los cambios en los términos del balance son pequeños y no parecen tener consistencia física. Obviamente, la temperatura a 2 m no es derivada directamente del balance de energía como si lo es la temperatura de superficie, por lo tanto, los resultados incluidos en esta investigación no son suficientes para comprender las causas del calentamiento generalizado.

Como se explicó, el uso de EFTs logra una mejora de los resultados generales, logrando reducir en la mayoría de los casos los desvíos de precipitación y temperaturas en simulaciones que utilizan una configuración convencional del modelo. De esta manera es posible interpretar un evento extremo a partir de una simulación que ofrece mucha mayor información que lo observado. Es habitual disponer de observaciones de algunas variables como precipitación, temperatura, presión, etc. Sin embargo, hay muchas otras variables que resultan difícil de medir como por ejemplo humedad del suelo, flujos de calor, flujos

de radiación, etc. Es por ello que contar con simulaciones precisas permite un análisis mucho mas amplio de los procesos de interacción.

En el caso de la sequía del 2008 la simulación de EFT muestra que las condiciones secas del suelo y la vegetación, expresadas a través de la humedad del suelo y el NDVI, modificaron la distribución espacial de algunas propiedades como fracción de vegetación verde, albedo, rugosidad de superficie y resistencia estomatal. Cuando se produce una anomalía negativa tan grande de lluvias, las temperaturas aumentan mas de lo normal incrementando el calor sensible y reduciendo el flujo de calor latente. Así, la sequedad del suelo continúa aumentando. Estas condiciones generales conducen a una deficiencia de la humedad atmosférica que incrementa la estabilidad de la atmósfera baja e intensifica la tendencia negativa de precipitación.

D.5 Sistema de pronóstico y monitoreo

La cuenca del Plata, junto a las grandes planicies en el centro de Estados Unidos son las regiones con mayor ocurrencia de precipitaciones intensas en el mundo (Zipser et al., 2006). A su vez, es una región con gran variabilidad climática que afecta las principales actividades económicas. A pesar de ello, hay escasa disponibilidad en información en tiempo real de variables hidrometeorológicas que sirvan de soporte en la toma de decisiones de distintos sectores o usuarios. Un sistema de pronóstico y monitoreo puede mejorar sustancialmente la administración por ejemplo, de los recursos hídricos y de las actividades agrícolas.

Actualmente existen algunas herramientas de pronósticos y monitoreo en la región, principalmente los que son provistos por el Servicio Meteorológico Nacional de Argentina y el Centro de Previsão de Tempo e Estudos Climáticos de Brasil. Sin embargo, la información brindada no siempre se adapta a la necesidad de los usuarios. El objetivo es desarrollar capacidades predictivas mediante la implementación de uns sistema de pronóstico y monitoreo en tiempo real. Se espera traduci r el conocimiento adquirido sobre la modelación del clima regional en información práctica para diferentes usuarios, principalmente de regiones agrícolas e hidrologicamente relevantes como el noreste de Argentina. El desarrollo intenta simplificar la interpretación de la información climática, ofreciendo herramientas gráficas en un sistema unificado y basado en simulaciones con el modelo WRF.

Todos los productos del sistema se basan en simulaciones rutinarias con el modelo WRF. El modelo realiza pronósticos para un período de 168 hs (7 días) con salidas cada 3 hs. Se simula diariamente sobre los mismos dominios que la climatología, es decir, un dominio de 45 km de resolución que cubre Sudamérica con un dominio anidado cubriendo la cuenca del Plata con resolución de 15 km.

Los datos de Global Forecast System son usados como forzantes.

El sistema consta de dos módulos, uno de monitoreo y otro de pronósticos. Ambos módulos basan todos sus productos en resultados obtenidos de las simulaciones diarias. El módulo de monitoreo muestra el comportamiento de variables hidrometeorológicas como precipitación, temperatura, escorrentía, humedad del suelo, entre otras en los últimos 30, 60 y 90 días. La información se brinda mediante mapas de promedios temporales y anomalías y también series de tiempo con promedio areal por subcuenca. El módulo de pronóstico muestra la evolución de cada variable en los próximos 7 días. Las herramientas son mapas con paso de tiempo trihorario, mapas de promedio temporal de los 7 días y anomalías y meteogramas, que brindan el pronóstico para lugares puntuales mediante series temporales. Todas las herramientas se publican en el sitio www.atmos.umd.edu/˜berbery/research/forecasts.html.

D.5.1 Verificación de los pronósticos

Dado que todo el sistema se basa en las simulaciones diarias, resulta esencial evaluar la calidad de los pronósticos con observaciones. La evaluación se restringe a valores diarios de precipitación y temperatura sobre el dominio anidado. Los datos observados provienen de estaciones meteorológicas y la comparación es punto a punto. Es decir, los valores de cada estación se comparan con el punto de grilla mas cercano. Los datos observados se toman del conjunto conformado en el National Center Data Center, que reune información de los servicios meteorológicos de cada país. El período de evaluación va desde el 1 de Agosto de 2012 al 10 de Octubre de 2014, un total de 804 días. El conjunto de datos de pronóstico es una colección de 7 conjuntos individuales, uno por cada día de pronóstico.

La precipitación se evalúa en término de ocurrencia de precipitación utilizando un umbral de 0.25 *mm*. A partir de esta "binarización" de los datos observados y pronosticados se arman tablas de contingencia. Estas tablas cruzan la información de pronóstico de días lluviosos (si/no) con las observaciones de días lluviosos (si/no). De la combinación surgen cuatro valores enteros: aciertos, negativos correctos, falsas alarmas y errores. Luego, utilizando esta información se computan valores estadísticos como la precisión (que fracción de los pronósticos fueron correctos), la probabilidad de detección (que fracción de días lluviosos fueron correctamente pronosticados), la tasa de falsa alarma (fracción de días pronosticados como lluviosos que fueron secos) y la frecuencia del desvío (frecuencia de eventos pronosticados sobre la frecuencia de eventos observados). Los valores estadísticos se computan para cada estación y luego se sintetizan con mapas y series de tiempo que resumen la habilidad del modelo.

El mapa de precisión que promedia la evaluación de los 7 pronósticos mues-

tra valores de precisión superiores a 0.7 (en un rango posible de 0 a 1) hacia el sur del dominio, con un leve decaimiento en la parte norte del dominio (principalmente en Bolivia y Paraguay) con valores en el rango 0.6 a 0.7. Notoriamente, los mejores resultados se dan en Chile y el oeste de Argentina donde la topografía implica una dificultad extra. Aquí, la precisión varía entre 0.8 y 1 indicando que mas del 80 % de días lluviosos o secos fueron correctamente pronosticados. Esta gran tasa de precisión se debe principalmente a la gran cantidad de negativos correctos, es decir, pronósticos de días secos que finalmente se observan. La región es mayormente árida y el modelo logra representar esta característica satisfactoriamente.

Analizando la evolución de la calidad del pronóstico a medida que el día pronosticado se aleja del día de inicio de la simulación se observa que la precisión logra mantenerse casi constante con valores siempre por encima de 0.7 para la cuenca del Plata. Es decir, el modelo acierta al menos en un 70 % la ocurrencia de días lluviosos o secos en la cuenca del Plata con 168 hs de anticipación. La curva de probabilidad de detección comienza con un valor de 0.7 que decrece hasta 0.55. En otras palabras, el porcentaje de días lluviosos que fueron pronosticados como tal varía entre 55 % con 6 días de anticipación a 70 % con mínima anticipación. Finalmente, la tasa de falsa alarma indica que alrededor del 55 % de los días pronosticados como lluviosos fueron secos. Esa gran cantidad de falsas alarmas puede deberse a tres motivos. Primero, el modelo tiende a sobrestimar ocurrencia de lluvia y subestimar su intensidad. Segundo, la incerteza en las observaciones. Un umbral de 0.25 *mm* puede resultar muy bajo para ser leído por el observador en estaciones convencionales. Pero inclusive mas importante es la hora en la cual se considera el cambio de día. Mientras este trabajo utiliza el horario UTC, muchas observaciones se hacen en hora local. Por último, la doble penalidad derivada de una comparación observación vs punto de grilla. Los métodos de verificación de este tipo tienden a penalizar con falsa alarma y evento omitido un evento observado desplazado de donde fue pronosticado.

Para evaluar temperatura se consideraron los valores mínimos, medios y máximos diarios. Notar que las salidas de la simulación son trihorarias por lo que los valores mínimos y máximos tienen un período de incertidumbre de 90 min. Se evaluó como difieren las magnitudes observadas de las pronosticadas mediante el error absoluto medio y el coeficiente de correlación. El coeficiente de correlación indica la correspondencia entre dos series, mientras que el error absoluto medio da una idea de la magnitud del error en el pronóstico. Al igual que para precipitación estos valores se calculan entre observaciones y sus puntos de grilla mas cercanos. Luego, se sintetizan mediante mapas que promedian los 7 pronósticos y curvas que promedian arealmente y muestran la evolución del pronóstico a medida que el tiempo transcurre desde el día de simulación.

Los mapas de correlación para temperaturas mínimas, medias y máximas muestran patrones similares con valores de correlación crecientes a medida que nos desplazamos al sur del dominio. En la parte norte del dominio se observaron correlaciones de alrededor de 0.7 que aumentan al sur con valores por encima de 0.9. El gradiente espacial concuerda con la verificación de precipitación donde los resultados también mejoran hacia el sur. Dada la incertidumbre presente en los valores mínimos y máximos, la temperatura media muestra una una distribución de coeficientes similar pero con valores levemente superiores.

Desde el punto de vista del tiempo de pronóstico, la correlación siempre se mantiene por encima de 0.8 para las tres variables, a excepción de temperatura máxima que decae levemente de ese valor para el máximo período de pronóstico. El error absoluto medio varía entre 2 $^{\circ}C$ y 4 $^{\circ}C$. En el caso particular de temperatura media alcanza una correlación de 0.95 para el primer día de pronóstico, con un error siempre por debajo de los 3 $^{\circ}C$. En resumen, el pronóstico de temperatura, ya sea mínima, media o máxima, presenta una muy buena correspondencia con los valores observados en la cuenca del Plata, principalmente en la parte sur, donde las correlaciones en general son superiores al 90 %. La magnitud de la diferencia varía entre 2 $^{\circ}C$ y 3 $^{\circ}C$ para temperatura mínima y media y alcanza los 4 $^{\circ}C$ para temperatura máxima.

D.6 Conclusiones

Esta tesis se centre en el análisis del efecto de los cambios de cobertura sobre el clima regional y por ende en el pronóstico de variables hidrometeorológicas. En este sentido, se definieron cuatro objetivos principales bajo la hipótesis de que una representación realista de las propiedades asociadas a la cobertura de superficie ayuda a mejorar la simulación de las interacciones suelo-atmósfera y por lo tanto reducen los desvíos del modelo inherentes a procesos de superficie. En esta sección, se hará una síntesis de las conclusiones principales como respuesta concreta a cada uno de los objetivos planteados.

D.6.1 Objetivo 1: Investigar la capacidad del modelo sobre la cuenca del Plata

Los buenos resultados obtenidos en la simulación climatológica indican que la parametrización utilizada resulta adecuada para la región. El modelo es consistente con los aspectos generales del clima regional. Por ejemplo, las condiciones húmedas sobre el Bosque Atlántico del Alto Paraná y el gradiente hacia la región más árida, es decir, el Desierto de Atacama son correctamente representados por el modelo. También logra identificar la gran variabilidad estacional de pre-

cipitación dada por la presencia de un sistema monzónico hacia el noreste del dominio. Además, los patrones de temperatura simulados presentan valores máximos al norte que decrecen gradualmente hacia el sur, tal como se espera cuando nos alejamos del Ecuador. Los desvíos mas importantes del modelo se dan sobre regiones montañosas como la cordillera de los Andes, pero esta falla es esperable cuando la resolución y parametrización no se ajustan a la complejidad topográfica presente en estas áreas.

Particularmente en la cuenca del Plata, el modelo ofrece muy buena correlación con valores por encima de 0.77 (computando por subcuencas y estaciones), con la particularidad que WRF simula precipitaciones mas frecuentes y menos intensas que las observadas. Sin embargo, el modelo tiende a generar desvíos negativos, es decir, condiciones mas secas que lo observado. Este puede ser el motivo por el cual se generan dificultades en la representación de sequías severas o extremas, como lo indicó el análisis de *SPI*. En términos de temperatura, la simulación mostró valores mas cálidos sobre la subcuenca del Paraguay, y levemente mas fríos hacia el este de la cuenca. En la subcuenca del Bajo Paraná, el modelo combina desvíos positivos y negativos. A pesar de estos desvíos, el modelo logra altas correlaciones en la parte sur de la cuenca, mientras que en la parte norte la correlación disminuye principalmente en meses fríos.

En resumen, la simulación climatológica demostró una gran capacidad del modelo para representar el clima regional. Contar con una simulación de alta resolución resulta fundamental para otro tipos de estudios que requieran el cómputo de anomalías. Sin embargo, se debe notar que el análisis sobre diferentes variables visualiza algunas deficiencias predictivas, principalmente en la parte norte de la cuenca. La reducción de estos errores es la motivación principal para evaluar el modelo con condiciones de superficie mas realistas que conduzcan a mejores resultados. En el futuro se espera extender el período de simulación para lograr un clima simulado mas representativo del clima regional, que mejore el cómputo de anomalías.

D.6.2 Objetivo 2: Mejorar la capacidad del modelo con ecosistemas funcionales

En los últimos años se han generado una cantidad importante de mapas de cobertura de alta calidad que pueden ser usados para mejorar la calidad de los modelos. Esta investigación contribuye en ese sentido presentando un nuevo enfoque para describir la vegetación en modelos regionales con información de ecosistemas funcionales derivada de satélites. Se crearon mapas variables en el tiempo de propiedades biofísicas utilizando el concepto de Tipos de Ecosistemas Funcionales, capaces de capturar condiciones anómalas de la vegetación. Este

enfoque asegura el uso de un conjunto de propiedades biofísicas consistente que reflejan el estado de la vegetación. Los beneficios del método son mas relevantes cuando las condiciones del suelo se alejan de los valores medios como sucede durante la ocurrencia de eventos extremos.

Para confirmar la utilidad del nuevo método, se evaluó la sequía del 2008 en el sur de Sudamérica. Las simulaciones de control que utilizan las condiciones superficiales convencionales (derivadas de USGS) representan el patrón espacial de precipitación, pero tienden a exagerar la severidad de la sequía, mientras que en otras regiones muestran desvíos positivos de precipitación que duplican los valores observados en algunos casos. La temperatura es razonablemente simulada en magnitud y distribución a excepción del desvío frío hacia la costa este, y los grandes errores sobre la Cordillera de los Andes.

El uso del nuevo conjunto de propiedades como reemplazo de las convencionales en el modelo WRF ofrecen evidencia que propiedades variables en el tiempo impactan en el rendimiento de modelos acoplados suelo-atmósfera. Particularmente, el uso de ecosistemas funcionales condujo a mejorar la simulación de la sequía y reducir el desvío húmedo en la mayoría de las regiones. Los resultados muestran que el modelo es sensible a los cambios de cobertura y a la variabilidad de la vegetación a través de las interacciones suelo-atmósfera.

Las estimaciones de precipitación mejoran en la mayoría de las regiones, mientras que la calidad de la simulación de temperatura varía según la región. Particularmente, los resultados mejoran notablemente la simulación hacia el este del dominio a la vez que degradan la simulación en la región central del dominio, donde el desvío se aumenta en 1 $^{\circ}C$. Estos resultados negativos no son totalmente comprendidos aún, pero pueden ser mejorados con pequeños cambios de parametrización que logren ajustar la simulación de temperatura. Estos cambios de parametrización combinados con cambios en las condiciones de superficie, al igual que procesos de advección requieren mayor estudio, pero dicho análisis está fuera del alcance de este trabajo.

D.6.3 Objetivo 3: Comprender el impacto de los cambios de uso del suelo

La interpretación de cambios en precipitación y temperatura debido a cambios de cobertura no resulta siempre evidente debido principalmente a la complejidad del sistema, que incluye cambios de cobertura y regímenes de circulación particulares para cada región bajo estudio. A su vez, mientras el modelo de superficie calcula balances puntuales (por columna), su uso sobre una grilla y acoplado a un modelo atmosférico implica que no-linealidades tridimencionales tomaran efecto. Cambios de cobertura pueden favorecer la generación de gradientes en diferentes variables, que a su vez inducen a circulaciones locales

y diferencias en los flujos de superficie. Los procesos advectivos también son afectados, como por ejemplo la convergencia del flujo de humedad.

En general, los resultados muestran que cuando un cambio de cobertura reduce la humedad del suelo, también se reduce la evapotranspiración, mientras el calor sensible aumenta. Esto conduce a mayor estabilidad atmosférica, y por lo tanto menor precipitación y escorrentía. Contrariamente, regiones con aumento en la humedad del suelo están asociados a reducciones en el calor sensible e incremento de calor latente lo que favorece una capa límite planetaria húmeda e inestable y por ende mayor precipitación y escorrentía.

El ejemplo mas claro de cambio en uso del suelo inducido por el hombre se observó en el Bosque Atlántico del Alto Paraná. El reemplazo de bosques subtropicales por cultivos en las últimas décadas condujo a una reducción de la rugosidad de superficie y un incremento en el albedo. Estas condiciones suavizaron el flujo total de calor generando menos intercambios turbulentos lo que produce una reducción en todas las componentes del balance de agua en superficie. Por su parte, la sequía del 2008 es un ejemplo de cambio en la cobertura por origen natural. La sequía comenzó con anomalías negativas de precipitación que afectó las condiciones del suelo y de la cobertura. Así, el suelo y la vegetación comenzaron a secarse mostrando menor fracción de vegetación verde, índice de área foliar y mayor resistencia estomatal. Las condiciones secas generalizadas dificultaron el proceso de evapotranspiración y luego la ocurrencia de precipitaciones significativas. Estos procesos fueron en parte responsables de la persistencia de la sequía que se extendió casi por dos años.

Como se indicó anteriormente, procesos de superficie derivados de cambios en la cobertura no siempre tienen una interpretación directa. Los experimentos realizados contribuyen en este sentido, ayudando a mejorar la comprensión de estos procesos. En futuros trabajos se estudiará la sequía de 2012 en la región central de Estados Unidos con la utilización de ecosistemas funcionales. El objetivo es evaluar el nuevo enfoque en regiones con gran cantidad y calidad de datos observados que permitan un análisis mas preciso de los procesos de superficie.

D.6.4 Objetivo 4: Desarrollar capacidades predictivas

La información meteorológica es usualmente requerida y apreciada por diferentes sectores y usuarios. Con el objetivo de responder a este requerimiento se desarrolló y evaluó un sistema de pronósticos y monitoreo. El conjunto de herramientas del sistema permiten caracterizar y monitorear los meses recientes de forma simple, y predecir el estado del tiempo con varios días de anticipación, contribuyendo así en la planificación de actividades y la reducción de riesgos causadas por condiciones anómalas.

Todas las herramientas se basan en simulaciones diarias a 7 días. Luego, los resultados de las simulaciones fueron evaluados con datos de estaciones de medición en términos de ocurrencia de precipitación y temperatura (mínima, media y máxima) ambos en valores diarios. El pronóstico de ambas variables muestra muy buenos resultados en la cuenca del Plata, principalmente en la parte sur de la cuenca. En particular, la ocurrencia de precipitación diaria se predice con una precisión promedio del 70 % y temperaturas con una correlación promedio con las observaciones del 85 % con errores medios absolutos va entre 2 $^{\circ}C$ y 4 $^{\circ}C$. La calidad del pronóstico se mantiene en un rango de calidad adecuado para el período de simulación, sugiriendo que puede ser extendido a mas de 7 días.

El sistema desarrollado no ofrece pronósticos oficiales de ninguna institución y por lo tanto no acarrea ningún compromiso. Sin embargo, las salidas del sistema son utilizadas como entrada de un sistema de alerta de caudales y como soporte para la emisión de pronósticos extendidos, como así también por usuarios particulares para planificar actividades en zonas rurales.

Notar que el sistema presentado no utiliza EFTs. El enfoque de EFTs permite una caracterización adecuada de las condiciones de superficie, es decir, de las condiciones de borde inferior en modelos regionales. La posibilidad de disponer de conjuntos de EFTs casi en tiempo real podría permitir su aplicación en pronósticos operativos. Un próximo paso podría ser la combinación de EFTs con el modelo de superficie Noah-MP. Este modelo posee características avanzadas con respecto a Noah LSM. Para ello, sería necesario suavizar los cambios entre EFTs en períodos de transición, es decir, al pasar de un año al siguiente.

Bibliography

Aceituno, P. (1988). On the functioning of the Southern Oscillation in the South American sector. Part I: Surface climate. *Monthly Weather Review*, 116:505–524.

Alcaraz, D., Paruelo, J., and Cabello, J. (2006). Identification of current ecosystem functional types in the Iberian Peninsula. *Global Ecology and Biogeography*, 15(2):200–212.

Alcaraz-Segura, D., Berbery, E., Lee, S., and Paruelo, J. (2011). Use of ecosystem functional types to represent the interannual variability of vegetation biophysical properties in regional models. *CLIVAR Exchanges*, 17:23–27.

Alcaraz-Segura, D., Berbery, E., Müller, O., and Paruelo, J. (2013a). Characterizing and monitoring climate regulation services. In *Earth Observation of Ecosystem Services*, chapter 16, pages 351–378. CRC Press.

Alcaraz-Segura, D., Paruelo, J. M., Epstein, H. E., and Cabello, J. (2013b). Environmental and human controls of ecosystem functional diversity in temperate South America. *Remote Sensing*, 5(1):127–154.

Aldeco, L. (2011). Aplicación de la técnica de análogos a la generación de pronósticos probabilísticos de precipitación sobre algunas estaciones de la Argentina.

Anderson, J. R. (1976). *A land use and land cover classification system for use with remote sensor data*, volume 964. US Government Printing Office.

Avila, F., Pitman, A., Donat, M., Alexander, L., and Abramowitz, G. (2012). Climate model simulated changes in temperature extremes due to land cover change. *Journal of Geophysical Research: Atmospheres (1984–2012)*, 117(D4).

Baidya Roy, S. and Avissar, R. (2002). Impact of land use/land cover change on regional hydrometeorology in Amazonia. *Journal of Geophysical Research: Atmospheres (1984–2012)*, 107(D20):LBA–4.

Baldi, G., Nosetto, M. D., Aragón, R., Aversa, F., Paruelo, J. M., and Jobbágy, E. G. (2008). Long-term satellite NDVI data sets: evaluating their ability to

detect ecosystem functional changes in South America. *Sensors*, 8(9):5397–5425.

Baldi, G. and Paruelo, J. M. (2008). Land-use and land cover dynamics in South American temperate grasslands. *Ecology and Society*, 13(2):6.

Barros, V., Clarke, R., and Dias, P. S. (2006). *Climate change in the La Plata basin*.

Beltrán-Przekurat, A., Pielke Sr, R. A., Eastman, J. L., and Coughenour, M. B. (2012). Modelling the effects of land-use/land-cover changes on the near-surface atmosphere in southern South America. *International Journal of Climatology*, 32(8):1206–1225.

Berbery, E. H. and Barros, V. R. (2002). The hydrologic cycle of the La Plata basin in South America. *Journal of Hydrometeorology*, 3(6):630–645.

Betts, A. K., Ball, J. H., Beljaars, A., Miller, M. J., and Viterbo, P. A. (1996). The Land surface-atmosphere interaction: a review based on observational and global modeling perspectives. *Journal of Geophysical Research: Atmospheres (1984–2012)*, 101(D3):7209–7225.

Bidegain, M. (2009). Severe drought in central Argentina and Uruguay. *Bulletin of American Meteorological Society*, 90(8):S138.

Carvalho, L. M., Jones, C., and Liebmann, B. (2004). The South Atlantic convergence zone: Intensity, form, persistence, and relationships with intraseasonal to interannual activity and extreme rainfall. *Journal of Climate*, 17(1):88–108.

Chen, F. and Dudhia, J. (2001). Coupling an advanced land surface-hydrology model with the Penn State-NCAR MM5 modeling system. Part I: Model implementation and sensitivity. *Monthly Weather Review*, 129(4):569–585.

Chen, F., Mitchell, K., Schaake, J., Xue, Y., Pan, H.-L., Koren, V., Duan, Q. Y., Ek, M., and Betts, A. (1996). Modeling of land surface evaporation by four schemes and comparison with FIFE observations. *Journal of Geophysical Research: Atmospheres (1984–2012)*, 101(D3):7251–7268.

Chen, M., Shi, W., Xie, P., Silva, V., Kousky, V. E., Wayne Higgins, R., and Janowiak, J. E. (2008). Assessing objective techniques for gauge-based analyses of global daily precipitation. *Journal of Geophysical Research: Atmospheres (1984–2012)*, 113(D4).

Collini, E. A., Berbery, E. H., Barros, V. R., and Pyle, M. E. (2008). How does soil moisture influence the early stages of the South American monsoon? *Journal of Climate*, 21(2):195–213.

Doyle, M. E., Saurral, R. I., and Barros, V. R. (2012). Trends in the distributions of aggregated monthly precipitation over the La Plata Basin. *International Journal of Climatology*, 32(14):2149–2162.

Dravitzki, S. and McGregor, J. (2011). Predictability of heavy precipitation in the Waikato river basin of New Zealand. *Monthly Weather Review*, 139(7):2184–2197.

Dros, J. M. a. (2004). Managing the soy boom: two scenarios of soy production expansion for South America. Technical report, AIDEnvironment.

Dudhia, J. (1989). Numerical study of convection observed during the winter monsoon experiment using a mesoscale two-dimensional model. *Journal of the Atmospheric Sciences*, 46(20):3077–3107.

Eidenshink, J. C. and Faundeen, J. L. (1994). The 1 km AVHRR global land data set: first stages in implementation. *International Journal of Remote Sensing*, 15(17):3443–3462.

Eltahir, E. A. (1998). A soil moisture–rainfall feedback mechanism: 1. Theory and observations. *Water Resources Research*, 34(4):765–776.

Fan, Y. and Van den Dool, H. (2008). A global monthly land surface air temperature analysis for 1948–present. *Journal of Geophysical Research: Atmospheres (1984–2012)*, 113(D1).

Foley, J. A., Levis, S., Costa, M. H., Cramer, W., and Pollard, D. (2000). Incorporating dynamic vegetation cover within global climate models. *Ecological Applications*, 10(6):1620–1632.

Friedl, M. A., McIver, D. K., Hodges, J. C., Zhang, X., Muchoney, D., Strahler, A. H., Woodcock, C. E., Gopal, S., Schneider, A., Cooper, A., et al. (2002). Global land cover mapping from modis: algorithms and early results. *Remote Sensing of Environment*, 83(1):287–302.

Friedl, M. A., Sulla-Menashe, D., Tan, B., Schneider, A., Ramankutty, N., Sibley, A., and Huang, X. (2010). MODIS Collection 5 global land cover: Algorithm refinements and characterization of new datasets. *Remote Sensing of Environment*, 114(1):168–182.

García Skabar, Y., Vidal, L., Salio, P., and Nicolini, M. (2011). Experimental high-resolution forecast in a region of Argentina. *Working group in Numerical Experimentation (WGNE) Research Activities in Atmospheric and Oceanic Modelling (Blue book)*, 5:09–10.

Ge, J., Qi, J., Lofgren, B. M., Moore, N., Torbick, N., and Olson, J. M. (2007). Impacts of land use/cover classification accuracy on regional climate simulations. *Journal of Geophysical Research: Atmospheres (1984–2012)*, 112(D5).

Geary, T. F. (2001). Afforestation in Uruguay: Study of a changing landscape. *Journal of Forestry*, 99(7):35–39.

Guo-Shuai, Z., Jun-Bang, W., Wen-Yi, F., and Tian-Yu, Y. (2011). Vegetation net primary productivity in Northeast China in 2000-2008: simulation and seasonal change. *Yingyong Shengtai Xuebao*, 22(3).

Hartmann, D. L. (1994). *Global physical climatology*, volume 56. Academic press.

Hoffman, R. N. and Kalnay, E. (1983). Lagged average forecasting, an alternative to Monte Carlo forecasting. *Tellus A*, 35(2):100–118.

Holton, J. et al. (2004). *Dynamic meteorology*. Elsevier Amsterdam, fourth edition.

Huffman, G. J., Bolvin, D. T., Nelkin, E. J., Wolff, D. B., Adler, R. F., Gu, G., Hong, Y., Bowman, K. P., and Stocker, E. F. (2007). The TRMM multisatellite precipitation analysis (TMPA): Quasi-global, multiyear, combined-sensor precipitation estimates at fine scales. *Journal of Hydrometeorology*, 8(1):38–55.

Izquierdo, A. E., De Angelo, C. D., and Aide, T. M. (2008). Thirty years of human demography and land-use change in the Atlantic Forest of Misiones, Argentina: an evaluation of the Forest Transition Model. *Ecology and Society*, 13(2):3.

Jacobson, M. Z. (2005). *Fundamentals of atmospheric modeling*. Cambridge University Press.

Janjic, Z. (1996). The surface layer parameterization in the NCEP Eta Model. *WORLD METEOROLOGICAL ORGANIZATION-PUBLICATIONS-WMO TD*, pages 4–16.

Janjic, Z. I. (1994). The step-mountain eta coordinate model: Further developments of the convection, viscous sublayer, and turbulence closure schemes. *Monthly Weather Review*, 122(5):927–945.

Janjic, Z. I. (2000). Comments on "Development and evaluation of a convection scheme for use in climate models". *Journal of the Atmospheric Sciences*, 57(21):3686–3686.

Jiang, L., Kogan, F. N., Guo, W., Tarpley, J. D., Mitchell, K. E., Ek, M. B., Tian, Y., Zheng, W., Zou, C.-Z., and Ramsay, B. H. (2010). Real-time weekly global green vegetation fraction derived from advanced very high resolution radiometer-based NOAA operational global vegetation index (GVI) system. *Journal of Geophysical Research: Atmospheres (1984–2012)*, 115(D11).

Kalnay, E., Kanamitsu, M., Kistler, R., Collins, W., Deaven, D., Gandin, L., Iredell, M., Saha, S., White, G., Woollen, J., et al. (1996). The NCEP/NCAR 40-year reanalysis project. *Bulletin of the American meteorological Society*, 77(3):437–471.

Kaufmann, R., Zhou, L., Myneni, R., Tucker, C., Slayback, D., Shabanov, N., and Pinzon, J. (2003). The effect of vegetation on surface temperature: A statistical analysis of NDVI and climate data. *Geophysical Research Letters*, 30(22).

Kodama, Y.-M. (1993). Large-scale common features of subtropical convergence zones (the Baiu frontal zone, the SPCZ, and the SACZ). Part II: Conditions of the circulations for generating the STCZs. *J. Meteor. Soc. Japan*, 71:581–610.

Kok, K., Schreur, B. W., and Vogelezang, D. (2008). Valuing information from mesoscale forecasts. *Meteorological Applications*, 15(1):103–111.

Koster, R. D., Dirmeyer, P. A., Guo, Z., Bonan, G., Chan, E., Cox, P., Gordon, C. T., Kanae, S., Kowalczyk, E., Lawrence, D., Liu, P., Lu, C.-H., Malyshev, S., McAvaney, B., Mitchell, K., Mocko, D., Oki, T., Oleson, K., Pitman, A., Sud, Y. C., Taylor, C. M., Verseghy, D., Vasic, R., Xue, Y., and Yamada, T. (2004). Regions of strong coupling between soil moisture and precipitation. *Science*, 305(5687):1138–1140.

Koster, R. D. and Suarez, M. J. (2003). Impact of land surface initialization on seasonal precipitation and temperature prediction. *Journal of Hydrometeorology*, 4(2).

Koster, R. D., Suarez, M. J., Ducharne, A., Stieglitz, M., and Kumar, P. (2000). A catchment-based approach to modeling land surface processes in a general circulation model: 1. Model structure. *Journal of Geophysical Research: Atmospheres (1984–2012)*, 105(D20):24809–24822.

Krepper, C. M. and Zucarelli, G. A. (2010). Assesing interannual water balance of La Plata river basin. *Atmóosfera*, 22:387–398.

Kurkowski, N. P., Stensrud, D. J., and Baldwin, M. E. (2003). Assessment of implementing satellite-derived land cover data in the Eta model. *Weather and forecasting*, 18(3):404–416.

Lawrence, P. J. and Chase, T. N. (2007). Representing a new MODIS consistent land surface in the community land model (CLM 3.0). *Journal of Geophysical Research: Biogeosciences (2005–2012)*, 112(G1).

Lee, S.-J. (2010). *Impact of land surface vegetation change over the La Plata Basin on the regional climatic environment: A study using conventional land-cover/land-use and newly developed ecosystem functional types*. PhD thesis, University of Maryland, College Park, MD, USA.

Lee, S.-J. and Berbery, E. H. (2012). Land cover change effects on the climate of the La Plata Basin. *Journal of Hydrometeorology*, 13(1):84–102.

Lee, S.-J., Berbery, E. H., and Alcaraz-Segura, D. (2013a). Effect of implementing ecosystem functional type data in a mesoscale climate model. *Advances in Atmospheric Sciences*, 30(5):1373–1386.

Lee, S.-J., Berbery, E. H., and Alcaraz-Segura, D. (2013b). The impact of ecosystem functional type changes on the la plata basin climate. *Advances in Atmospheric Sciences*, 30(5):1387–1405.

Levis, S., Bonan, G. B., and Bonfils, C. (2004). Soil feedback drives the mid-Holocene North African monsoon northward in fully coupled CCSM2 simulations with a dynamic vegetation model. *Climate Dynamics*, 23(7-8):791–802.

Li, D., Bou-Zeid, E., Barlage, M., Chen, F., and Smith, J. A. (2013). Development and evaluation of a mosaic approach in the WRF-Noah framework. *Journal of Geophysical Research: Atmospheres*, 118(21):11–918.

Liu, Y., Parinussa, R., Dorigo, W., De Jeu, R., Wagner, W., Van Dijk, A., McCabe, M., and Evans, J. (2011). Developing an improved soil moisture dataset by blending passive and active microwave satellite-based retrievals. *Hydrology and Earth System Sciences*, 15(2):425–436.

Mahmood, R., Quintanar, A. I., Conner, G., Leeper, R., Dobler, S., Pielke Sr, R. A., Beltran-Przekurat, A., Hubbard, K. G., Niyogi, D., Bonan, G., et al. (2010). Impacts of land use/land cover change on climate and future research priorities. *Bulletin of the American Meteorological Society*, 91(1):37–46.

McKee, T. B., Doesken, N. J., and Kleist, J. (1993). The relationship of drought frequency and duration to time scales. In *Proceedings of the 8th Conference on Applied Climatology*, volume 17, pages 179–183. American Meteorological Society Boston, MA.

McNaughton, S. J., Oesterheld, M., Frank, D. A., and Williams, K. (1989). Ecosystem-level patterns of primary productivity and herbivory in terrestrial habitats.

Mechoso, C. R. and Perez Iribarren, G. (1992). Streamflow in southeastern South America and the Southern Oscillation. *Journal of Climate*, 5:1535–1539.

Michalakes, J., Dudhia, J., Gill, D., Henderson, T., Klemp, J., Skamarock, W., and Wang, W. (2004). The weather research and forecast model: software architecture and performance. In *Proceedings of the 11th ECMWF Workshop on the Use of High Performance Computing In Meteorology*, volume 25, page 29. World Scientific.

Miller, J., Barlage, M., Zeng, X., Wei, H., Mitchell, K., and Tarpley, D. (2006). Sensitivity of the NCEP/Noah land surface model to the MODIS green vegetation fraction data set. *Geophysical research letters*, 33(13).

Mitchell, K. et al. (2005). The community Noah Land–Surface Model (LSM) Users Guide. *Public Release Version*, 2(1).

Mlawer, E. J., Taubman, S. J., Brown, P. D., Iacono, M. J., and Clough, S. A. (1997). Radiative transfer for inhomogeneous atmospheres: RRTM, a validated correlated-k model for the longwave (Paper 97JD00237). *JOURNAL OF GEOPHYSICAL RESEARCH-ALL SERIES-*, 102:16–663.

Mo, K. C. and Berbery, E. H. (2011). Drought and persistent wet spells over South America based on observations and the U.S. CLIVAR drought experiments. *Journal of Climate*, 24:1801–1820.

Müller, O. V., Berbery, E. H., Alcaraz-Segura, D., and Ek, M. B. (2014). Regional model simulations of the 2008 drought in southern South America using a consistent set of land surface properties. *Journal of Climate*, 27:6754–6778.

Müller, O. V. and García, N. O. (2006-2010). Análisis de la predicción de precipitaciones mediante correlaciones canónicas en el NE de Argentina. *Revista Geofísica*, 62:61–78.

Müller, O. V. and Berbery, E. H. (2014). Routine forecasting and monitoring system for agricultural and hydrological applications on La Plata Basin. In *Anales del 2do. Congreso Internacional de Hidrología de Llanuras*, Santa Fe, Argentina+. FICH-UNL.

Niu, G.-Y., Yang, Z.-L., Mitchell, K. E., Chen, F., Ek, M. B., Barlage, M., Kumar, A., Manning, K., Niyogi, D., Rosero, E., et al. (2011). The community noah land surface model with multiparameterization options (Noah-MP): 1. model description and evaluation with local-scale measurements. *Journal of Geophysical Research: Atmospheres (1984–2012)*, 116(D12).

Nogués-Paegle, J. and Berbery, H. R. (2000). Low-level jets over the Americas. *CLIVAR Exchanges*, 5(2):6–8.

Nuñez, M. N., Solman, S. A., and Cabré, M. F. (2009). Regional climate change experiments over southern South America. II: Climate change scenarios in the late twenty-first century. *Climate Dynamics*, 32(7-8):1081–1095.

Ooyama, K. V. (1990). A thermodynamic foundation for modeling the moist atmosphere. *Journal of the Atmospheric Sciences*, 47(21):2580–2593.

Paruelo, J. M., Guershman, J. P., and Verón, S. R. (2005). Expansión agrícola y cambios en el uso del suelo. *Ciencia Hoy*, 15(87):14–23.

Paruelo, J. M., Jobbagy, E. G., and Sala, O. E. (2001). Current distribution of ecosystem functional types in temperate South America. *Ecosystems*, 4(7):683–698.

Peixoto, J. and Oort, A. H. (1992). Physics of climate, 520 pp. *Am. Inst. of Phys., New York*.

Penalba, O. C., Rivera, J. A., and Bettolli, M. L. (2010). Trends and periodicities in the annual amount of dry days over Argentina, looking towards the climatic change. In *Second International Conference on Drought Management: Economics of Drought and Drought Preparedness in CIHEAM Journal Options Méditerranéennes*, pages 4–6.

Pielke, R., Adegoke, J., Beltran-Przekurat, A., Hiemstra, C., Lin, J., Nair, U., Niyogi, D., and Nobis, T. (2007). An overview of regional land-use and land-cover impacts on rainfall. *Tellus B*, 59(3):587–601.

Rayner, J. (2001). *Dynamic climatology: basis in mathematics and physics*. Blackwell Publishing.

Rogers, E., Black, T., Ferrier, B., Lin, Y., Parrish, D., and DiMego, G. (2001). Changes to the NCEP Meso Eta Analysis and Forecast System: Increase in resolution, new cloud microphysics, modified precipitation assimilation, modified 3DVAR analysis. *NOAA/NWS Technical Procedures Bulletin*, 488.

Ropelewski, C. F. and Halpert, M. S. (1987). Global and regional scale precipitation patterns associated with the El Niño/Southern Oscillation. *Monthly Weather Review*, 115:1606–1626.

Rusticucci, M., Marengo, J., Penalba, O., and Renom, M. (2010). An intercomparison of model-simulated in extreme rainfall and temperature events during the last half of the twentieth century. Part 1: mean values and variability. *Climatic Change*, 98(3-4):493–508.

Saha, S., Moorthi, S., Pan, H.-L., Wu, X., Wang, J., Nadiga, S., Tripp, P., Kistler, R., Woollen, J., Behringer, D., et al. (2010). The NCEP Climate Forecast System Reanalysis. *Bulletin of the American Meteorological Society*, 91(8):1015–1057.

Saulo, C., Cardazzo, S., Ruiz, J., Campetella, C., and Rolla, A. (2008). El sistema de pronóstico experimental del Centro de Investigaciones del Mar y la Atmósfera. *Meteorologica*, 33:83–97.

Seager, R., Naik, N., Baethgen, W., Robertson, A., Kushnir, A., Nakamura, J., and Jurburg, S. (2010). Tropical oceanic causes of interannual to multidecadal precipitation variability in Southeast South America over the Past Century. *Journal of Climate*, 23:5517–5539.

Sellers, P., Berry, J., Collatz, G. J., Field, C. B., and Hall, F. G. (1992). Canopy reflectance, photosynthesis, and transpiration. iii. A reanalysis using improved leaf models and a new canopy integration scheme. *Remote Sensing of Environment*, 42(3):187–216.

Seneviratne, S. I., Corti, T., Davin, E. L., Hirschi, M., Jaeger, E. B., Lehner, I., Orlowsky, B., and Teuling, A. J. (2010). Investigating soil moisture–climate interactions in a changing climate: A review. *Earth-Science Reviews*, 99(3):125–161.

Silvestri, G. and Vera, C. (2008). Evaluation of the WCRP-CMIP3 model simulations in the la plata basin. *Meteorological Applications*, 15(4):497–502.

Skamarock, W. C., Klemp, J. B., Dudhia, J., Gill, D. O., Barker, D. M., Duda, M. G., Huang, X.-Y., Wang, W., and Powers, J. G. (2008). A description of the Advanced Research WRF version 3. Technical report, NCAR.

Skansi, M., Núñez, S., Podestá, G., Veiga, H., and Garay, N. (2009). La sequía del año 2008 en la región húmeda argentina descripta a través del índice de precipitación estandarizado. In *Actas del XIII Congreso Latinoamericano e Ibérico de Meteorología y X Congreso Argentino de Meteorología.*, Buenos Aires, Argentina.

Smith, B., Prentice, I. C., and Sykes, M. T. (2001). Representation of vegetation dynamics in the modelling of terrestrial ecosystems: comparing two contrasting approaches within European climate space. *Global Ecology and Biogeography*, 10(6):621–637.

Solman, S. A., Nuñez, M. N., and Cabré, M. F. (2008). Regional climate change experiments over southern South America. I: present climate. *Climate Dynamics*, 30(5):533–552.

Solman, S. A., Sanchez, E., Samuelsson, P., da Rocha, R., Li, L., Marengo, J., Pessacg, N., Remedio, A., Chou, S., , et al. (2013). Evaluation of an ensemble of regional climate model simulations over south america driven by the ERA-Interim reanalysis: model performance and uncertainties. *Climate Dynamics*, 41(5-6):1139–1157.

Stanski, H. R., Wilson, L. J., and Burrows, W. R. (1989). *Survey of common verification methods in meteorology*. World Meteorological Organization Geneva.

Stone, R. C. and Meinke, H. (2005). Operational seasonal forecasting of crop performance. *Philosophical Transactions of the Royal Society B: Biological Sciences*, 360(1463):2109–2124.

Sörensson, A. A. and Berbery, H. (2014). A single period analysis of soil moisture memory and interactions with surface climate for different vegetation types in the La Plata Basin. *Journal of Hydrometeorology*, In revision.

Tartaglione, N. (2010). Relationship between precipitation forecast errors and skill scores of dichotomous forecasts. *Weather and Forecasting*, 25(1):355–365.

Tian, Y., Dickinson, R., Zhou, L., Myneni, R., Friedl, M., Schaaf, C., Carroll, M., and Gao, F. (2004a). Land boundary conditions from MODIS data and consequences for the albedo of a climate model. *Geophysical Research Letters*, 31(5).

Tian, Y., Dickinson, R., Zhou, L., and Shaikh, M. (2004b). Impact of new land boundary conditions from Moderate Resolution Imaging Spectroradiometer (MODIS) data on the climatology of land surface variables. *Journal of Geophysical Research: Atmospheres (1984–2012)*, 109(D20).

Valentini, R., Baldocchi, D., Tenhunen, J., and Kabat, P. (1999). Ecological controls on land-surface atmospheric interactions. *Integrating Hydrology, Ecosystems Dynamics, and Biogeochemistry in Complex Landscapes*.

Virji, H. (1981). A preliminary study of summertime tropospheric circulation patterns over South America estimated from clouds winds. *Monthly Weather Review*, 109:599–610.

Volante, J., Alcaraz-Segura, D., Mosciaro, M., Viglizzo, E., and Paruelo, J. (2012). Ecosystem functional changes associated with land clearing in NW Argentina. *Agriculture, Ecosystems & Environment*, 154:12–22.

Wan, Z. and Li, Z.-L. (2011). MODIS land surface temperature and emissivity. In *Land Remote Sensing and Global Environmental Change*, pages 563–577. Springer.

Wang, W., Bruyère, C., Duda, M., Dudhia, J., Gill, D., Kavulich, M., Keene, K., Lin, H.-C., Michalakes, J., Rizvi, S., Zhang, X., Berner, J., and Smith, K. (2014). *ARW Version 3 Modeling System User's Guide*. National Center for Atmospheric Research.

Weisman, M. L., Davis, C., Wang, W., Manning, K. W., and Klemp, J. B. (2008). Experiences with 0-36-h explicit convective forecasts with the WRF-ARW model. *Weather and Forecasting*, 23(3):407–437.

Weiss, M., van den Hurk, B., Haarsma, R., and Hazeleger, W. (2012). Impact of vegetation variability on potential predictability and skill of EC-Earth simulations. *Climate Dynamics*, 39(11):2733–2746.

Wilks, D. S. (2011). Chapter 8: Forecast verification. In *Statistical methods in the atmospheric sciences*, volume 100, pages 301–393. Academic press.

World Meteorological Organization (2009). Experts agree on a universal drought index to cope with climate risks. Technical report, Geneva. Press Releas No. 82.

World Meteorological Organization (2010). Implementation plan for the global observing system for climate in support of the unfccc. WMO-TD/No. 1523.

Zipser, E. J., Liu, C., Cecil, D. J., Nesbitt, S. W., and Yorty, D. P. (2006). Where are the most intense thunderstorms on Earth? *Bulletin of the American Meteorological Society*, 87(8):1057–1071.

Doctorado en Ingeniería
mención recursos hídricos

Título de la obra:

Hydrometeorological Forecasts and Their Sensitivity to Land Cover Changes

Autor: Omar Vicente Müller

Lugar: Santa Fe, Argentina

Palabras Claves:

Hydrometeorological Forecasts, Regional Modeling,
Land Use/Land Cover Changes, Ecosystem Functioning,
Ecosystem Functional Types, Biophysical Properties,
Land Surface Processes, Land-Atmosphere Interactions,
Decision Support System, Monitoring and Forecasting System,
Forecasts Verification.